UNIVERSITY OF CALIFORNIA

Los Angeles

Electrostatic Mode Coupling Of Beat Excited Electron Plasma Waves

A dissertation submitted in partial satisfaction of the
requirements for the degree Doctor of Philosophy
in Physics

by

Christopher Brian Darrow

1986

The dissertation of Christopher Brian Darrow is approved.

Francis F. Chen

Francis F. Chen

Walter Gekelman

Walter Gekelman

Chandra Joshi

Chan Joshi, Committee Co-chair

John M. Dawson

John M. Dawson, Committe Co-chair

University of California, Los Angeles

1986

Dedicated to my parents ... All of them.

TABLE OF CONTENTS

TABLE OF CONTENTS (cont.)

LIST OF SYMBOLS

a_m	Temporal envelope
c	Velocity of light in vacuum
c_e	Electron thermal velocity
E_1	Electric field
E	Electric field in units of E_{cold}
E_{cold}	Cold plasma wave breaking field
F	Unitless force
I	Laser intensity
J_m	m^{th} Bessel function
k_p	Plasma wavenumber
k_i	Ripple wavenumber
k_1, k_2	Laser wavenumbers
n(x)	Density as a function of x
n_o	Background plasma density
p, f(p)	Thermal parameter and function
v_ϕ	Phase velocity of a wave
α_j	v_{osc}/c of j^{th} laser beam
γ	Growth rate
λ_d	Debye length
Ψ_m	Oscillatory phase of m^{th} mode
COM	"Collinear Optical Mixing"
CPOM	"Count Propagating Optical Mixing"

ACKNOWLEDGMENTS

I would like to thank my thesis committee for their interest and responsivenss in reviewing the manuscript. I would also like to thank Walter Gekelman for his valuable, objective critique from the point of view of a physicist not directly involved in laser-plasma interactions.

I am grateful for the guidance provided by Professors F. F. Chen, J. M. Dawson, and C. Joshi, all of whose insights and physical intuition were instrumental in the development of the topic addressed in this thesis.

I also thank for their respective contributions in the laboratory, Dr. C. Clayton, K. Marsh, D. Umstadter, and R. Williams.

I am indebted to Dr. T. Katsouleas and W. B. Mori, without whose assistance the theory, in its present place and form, would not have been possible. I am also grateful to W. B. Mori for his assistance with the computer simulations.

Finally, I wish to give special thanks to Chan Joshi for his many sleepless nights spent in the lab during our experimental runs. His enthusiasm and perseverance have been a great inspiration to me.

VITA

1979 B. S., University of California, Los Angeles.

1979, 1980 Teaching Assistant, Department of Physics, University of California, Los Angeles.

1981 M. S., University of California, Los Angeles.

1980 - 1983 Research Assistant, Department of Physics, University of California, Los Angeles.

1983 - 1986 Research Assistant, Department of Electrical Engineering, University of California, Los Angeles.

PUBLICATIONS

"Development of Two-Dimensional Structures in Cavitons," D. L. Eggleston, A. Y. Wong, and C. B. Darrow, Phys. Fluids 25, 257 (1982)

"Simultaneous Observations of Caviton Formation, Spikey Turbulence and Electromagnetic Radiation," P. Y. Cheung, A. Y. Wong, C. B. Darrow, and S. J. Qian, Phys. Rev. Lett. 48, 1348 (1982).

"Ionospheric Cavitons and Related Nonlinear Phenomena," A. Y. Wong, J. Santoru, C. Darrow, L. Wang, and J. G. Roederer, Radio Science 18, 815 (1983)

"Relativistic Plasma Wave Excitation by Collinear Optical Mixing," C. Clayton, C. Joshi, C. Darrow, and D. Umstadter, Phys. Rev. Lett. 54, 2343 (1985).

"A Novel Small Angle Thomson Scattering System," C. E. Clayton, C. Darrow, and C. Joshi, Appl. Optics 24, 2823 (1985)

"Saturation of Beat-Excited Plasma Waves by Electrostatic Mode Coupling," C. Darrow, D. Umstadter, T. Katsouleas, W. B. Mori, C. E. Clayton, and C. Joshi, Phys. Rev. Lett. 56, 2629 (1986).

ABSTRACT OF THE DISSERTATION

Electrostatic Mode Coupling Of Beat Excited Electron Plasma Waves

by

Christopher Brian Darrow
Doctor of Philosophy in Physics
University of California, Los Angeles, 1986

The nature of the spectrum of electrostatic waves which is excited when two laser beams beat in a plasma containing a density ripple is investigated theoretically, experimentally and computationally.

A theoretical model for the beat wave excitation process in a rippled-density plasma is developed. The model predicts the generation of a rich spectrum of plasma modes with frequencies equal to the beat frequency of the two laser beams and wavenumbers equal to integer multiples of the ripple wavenumber. For commonly encountered experimental parameters a new beat wave saturation mechanism has been found which can limit the amplitude of the beat wave to a value well below that expected for the widely quoted relativistic detuning process. The effects of stimulated Raman scattering, ion wave harmonics, and other coupling mechanisms are also discussed.

CO_2 laser experiments designed to study and characterize beat wave excitation and mode coupling were conducted. The results of collective ruby laser Thomson scattering and other measurements of the electrostatic and scattered electromagnetic spectra are presented. Despite the richness in physics of the experiment, the simple model is able to predict the observed behavior and characteristics of the beat wave and coupled modes. Direct comparisons between the experimental results and theoretical predictions are made regarding mode saturation amplitudes. Evidence for electrostatic modes driven by SRS driven plasma waves and by the lasers when their frequency difference equals twice the plasma frequency is also presented.

Computer simulations were employed to both model the experiment and test the theory. The results of the simulations are in good qualitative agreement with both theory and experiment. In addition a mechanism for self stabilization of the mode coupling saturation mechanism is demonstrated.

CHAPTER I: INTRODUCTION

Collective particle accelerator schemes rely on the large space charge fields which arise when electrons are separated from ions to trap and accelerate charged particles to high energies[1,2] In the case of the Plasma Beat Wave Accelerator (PBWA) the electron plasma waves are created by the nonlinear force which arises when two collinear laser beams of slightly different frequencies beat in a plasma. This force causes longitudinal bunching of plasma electrons. The frequency and wavenumber of the bunching force equal the difference frequency ($\Delta\omega$) and difference wavenumber (Δk) of the two lasers. If $\omega_{es},k_{es}=\Delta\omega,\Delta k$ lies somewhere on the Bohm-Gross dispersion curve, plasma waves are resonantly driven by this force. The PBWA scheme exploits this resonance condition and the high fields attainable with present day lasers to drive the electron plasma waves to extremely large amplitudes for high gradient particle acceleration. For efficient operation it is desirable to excite plasma wave fields which are as large as possible and which remain coherent over the entire acceleration length. In this thesis effects which make it difficult to meet these two conditions will be investigated. In particular a mechanism which leads to saturation of the beat wave and disruption of its spatial coherence will be considered.

This mechanism involves the scattering of the plasma beat wave by density fluctuations present in the plasma. Alternatively this process can be thought of as mode coupling of the beat wave to larger- k electrostatic modes. These larger-k, low phase velocity modes can, through Landau damping, lead to efficient wave-plasma coupling of the high phase velocity beat wave. This mechanism is important to the PBWA because (1) The excitation of large-k modes leads to a spatially incoherent accelerating field and (2) The beat wave grows to a smaller amplitude because the driver energy is distributed among a large number of modes. Experimentally the density fluctuations of interest are likely to be encountered when stimulated Brillouin scatter (SBS) driven ion waves are excited by either of the two incident laser beams.

Our theoretical work on mode coupling differs from previous work by other authors who have studied the evolution of resonantly excited plasma waves with the pump but without the ripple[3,4,5,6] and with the ripple but without The pump[7,8].

In Ch. II we begin the study of this topic by reviewing the formulation of the beat wave problem. After reviewing the results of previous work which has treated beat wave excitation in uniform plasmas we present a model for beat excitation in a cold plasma containing a sinusoidal density ripple. We then go on to consider corrections for finite plasma temperature in preparation for interpretation of the experimental results. In Ch's. III and IV we present the results of our experimental studies of beat wave excitation and the coupled mode spectrum. In Ch. V we present the results of computer simulations which have been used to further corroborate the theoretical and experimental results.

CHAPTER II: THEORY OF BEAT WAVE EXCITATION

It is our purpose here to derive the plasma response to an excitation resulting from two beating laser beams. We will derive a simple equation of motion for the electron plasma wave electric field using the cold plasma fluid equations for a uniform plasma. We will then build upon this simple model to include beat wave growth in a density ripple and the effects of finite temperature.

COLD PLASMA

We begin with the warm electron fluid equations:

$$\frac{\partial n}{\partial t} + \vec{\nabla}\cdot(n\vec{v}) = 0 \qquad (1a)$$

$$mn\left[\frac{\partial \vec{v}}{\partial t} + (\vec{v}\cdot\vec{\nabla}\vec{v}) \right] = -ne\left[\vec{E} + \vec{v} \times \vec{B}/c \right] + \vec{\nabla}p \qquad (1b)$$

$$\vec{\nabla}\cdot\vec{E} = 4\pi e\,(\, n_i - n_e \,) \qquad (1c)$$

where the ions are assumed fixed and we build sufficient generality into the density to allow for the presence of density fluctuations (to be included later) by defining the densities as

$$n_e = n_o + \delta n + n_1 = n_o(x) + n_1(x,t)$$
$$n_i = n_o + \delta n \qquad = n_o(x).$$

Linearizing in the perturbed quantities,

$$n_e = n_0 + n_1$$

$$\vec{v} = 0 + \vec{v}_1$$

$$\vec{E} = 0 + \vec{E}_1$$

one obtains

$$\dot{n}_1 + n_0 v_1' = 0 \tag{2a}$$

$$n_0 m\, v_1' - \gamma T_e n_1' = n_0 e E_1 - n_0 e v_y B_z / c \tag{2b}$$

$$E_1' = -4\pi e n_1 \tag{2c}$$

where it has been assumed that the longitudinal electric field lies along the x-axis and that all quantities vary in x only. Differentiating Eq. 2a with respect to t and substituting 2c gives

$$\frac{\partial}{\partial x} \left[\ddot{E}_1 - 4\pi n_0 e \dot{v}_1 \right] = 0$$

Differentiating Eq. 2c with respect to x gives

$$E_1'' + 4\pi e n_1' = 0$$

Using these two results to eliminate all variables in Eq. 2b except E yields a wave equation for the electric field:

$$\ddot{E}_1 + \omega_{po}^2 E_1 + c_e^2 E_1'' = \omega_{po}^2 F_{nl}/e \qquad (3)$$

where $c_e^2 = \gamma T_e/m_e$ and F_{nl} is the nonlinear bunching force (ponderomotive force) provided by the beating laser beams:

$$F_{nl} = -ev_y B_z/c \ . \qquad (4)$$

Physically the bunching occurs because, as the electrons undergo quiver motion in the transverse electric field of the pump, the $\vec{v}_{quiver} \times \vec{B}_{pump}$ force acts in the x-direction. Since this force is largest where the field is largest (largest v_{quiver}) electrons are expelled from those regions and accumulate in the low field regions, i.e. at the nulls of the laser beat pattern. Eq. 3 shows that the plasma electric field responds like a simple harmonic oscillator with a driver force given by F_{nl}/e. We now derive an explicit expression for the driver "force".

The two pump magnetic and electric field components, assumed to vary as

$$\vec{e}_1 = \hat{y}\ e_{10} \sin(k_1x - \omega_2 t), \qquad \vec{e}_2 = \hat{y}\ e_{20} \sin(k_2x - \omega_2 t) \qquad (5a)$$

$$\vec{b}_1 = \hat{z}\ e_1 \qquad\qquad \vec{b}_2 = \hat{z}\ e_2, \qquad (5b)$$

give rise to electron quiver motion and its associated quiver velocity,

$$v_y = v_{y1} + v_{y2}, \qquad \text{where } v_{yi} = -(ee_{i0}/m\omega_i)\cos(k_i x - \omega_i t) \qquad (6)$$

The nonlinear force in Eq. 4 can now be written as

$$F_{nl} = -e/c(\ v_{y1} + v_{y2}\ )\ (e_{y1} + e_{y2}\ ). \qquad (7)$$

Substituting for v_y and explicitly including the temporal and spatial dependencies $\theta_i = k_i x - \omega_i t$, one finds

$$F_{nl} = e^2/mc \left[e_1^2/2\omega_1 \sin 2\theta_1 + e_2^2/2\omega_2 \sin 2\theta_2 + \right.$$

$$\left. \frac{e_1 e_2}{2}\left[\frac{1}{\omega_2} + \frac{1}{\omega_1}\right]\sin(\theta_2+\theta_1) + \frac{e_1 e_2}{2}\left[\frac{1}{\omega_1} - \frac{1}{\omega_2}\right]\sin(\theta_2-\theta_1) \right] \qquad (8)$$

Only those terms in F_{nl} which do not vanish when time averaged over the fast oscillation period will contribute to the relatively low frequency plasma wave driver. Averaging over the fast oscillation period Eq. 8 reduces to

$$F_{nl} = \frac{e^2 e_1 e_2}{2mc}\left[\frac{1}{\omega_1} - \frac{1}{\omega_2}\right]\sin(\Delta\theta)$$

where $\Delta\theta = \theta_2 - \theta_1 = \Delta kx - \Delta\omega t$, $\Delta k = k_2 - k_1$, and $\Delta\omega = \omega_2 - \omega_1$. For notational purposes we define $\alpha_i = ee_{io}/mc\omega_i = v_{osc}/c$, $E_{cold} = mc\omega_{po}/e$, and invoke the resonance condition $\Delta\omega \cong \omega_{po}$, where ω_{po} is the plasma frequency of the background plasma excluding any density perturbations (ripples). The driver force then takes the form

$$F_{nl}/e = \frac{1}{2} E_{cold}\, \alpha_1\alpha_2 \sin(\Delta kx - \Delta\omega t)$$

Normalizing the electric field E_1 in Eq. 3 to the cold plasma wave breaking field E_{cold} defined above, the equation of motion of the driven plasma wave electric field takes the dimensionless form

$$\ddot{E} + \omega_p^2(x)E + c_e^2 E'' = \frac{1}{2}\alpha_1\alpha_2\omega_{po}^2 \sin(\Delta kx - \Delta\omega t) \qquad (9)$$

Eq. 9 is the equation which governs the evolution of the electric field of the plasma wave driven by the ponderomotive force of two collinear laser beams beating in space. We have allowed for nonuniformities in the plasma density through $\omega_{po}(x)$. In treating plasmas containing density inhomogeneities we will only require that these inhomogeneities be such that an average density n_o can be defined so that $\omega_p(n_o) = \omega_{po} \cong \Delta\omega_{lasers}$.

Assuming a driver which "turns on" at t=0 and neglecting the thermal velocity c_e for now the solution to Eq. 9 can readily be shown to be

$$E(x,t) = \frac{\omega_{po}^2 F}{\omega_p^2 - \omega_{po}^2} \left[\sin(k_p x - \omega_{po} t) + \frac{\omega_{po}}{\omega_p} \sin(\omega_p t)\cos(k_p x) - \cos(\omega_p t)\sin(k_p x) \right] \qquad (10)$$

where $F = \frac{1}{2}\alpha_1\alpha_2$ parameterizes the beat wave driver strength and we now denote the driver ω and k as $\Delta k = k_p$, $\Delta\omega = \omega_{po}$.

UNIFORM PLASMA

Exactly resonant beat wave excitation in the absence of damping leads to resonant growth of a plasma wave to an arbitrarily large amplitude. To study the behavior we therefore consider the solution of Eq. 10 for "near-resonant" excitation by writing $\omega_p = \omega_{po} + \delta\omega$ where $\delta\omega/\omega_{po} << 1$. With this form for ω_p, Eq. 10 can be written as

$$E(x,t) = \frac{\omega_{po}^2 F}{2\omega_{po}\delta\omega} \left[\sin(\delta\omega t)\cos(k_p x - \omega_{po} t) - \frac{\delta\omega}{\omega_p} \cos(k_p x)\left\{ \cos(\delta\omega t)\sin(\omega_{po} t) + \sin(\delta\omega t)\cos(\omega_{po} t)\right\} \right] \qquad (11)$$

For $\delta\omega t << 1$ and $\delta\omega/\omega_{po} << 1$, $\sin(\delta\omega t) \cong \delta\omega t$, $\cos(\delta\omega t) \cong 1$, and Eq. 11 simplifies to

$$E(x,t) = \frac{\omega_{po}F}{2}\left[\ t\cos(k_px)\cos(\omega_{po}t) - \frac{1}{\omega_{po}}\cos(k_px)\sin(\omega_{po}t)\right].$$

For arbitrarily near-resonant excitation the beatwave field is seen to grow linearly in time (for $E(t=0) = 0$ as the initial condition) with a growth rate $\gamma = \alpha_1\alpha_2\omega_{po}/4$. The growth continues to an arbitrarily large field amplitude until the assumption $\delta\omega t<<1$ is violated. This behavior is modified when relativistic effects are included in the electron fluid equation of motion, Eq. 2b. Rosenbluth and Liu[6] and others, by using a fully relativistic equation of motion for the electron fluid, have studied such effects. In the relativistic case the field grows linearly in time at early times with the same growth rate as given above. However the field saturates abruptly upon reaching an amplitude $E = (16\alpha_1\alpha_2/3)^{1/3}$. Saturation occurs because of the relativistic electron mass increase incurred by the electrons as they attain relativistic quiver velocities in the plasma wave field. This mass increase shifts the electron plasma frequency and detunes the electrons from the driver. This saturation limits the field amplitude of the beat wave and is therefore of importance in the PBWA scheme.

INHOMOGENEOUS PLASMA: DENSITY RIPPLE

Eq. 9 provides a means for the study of the evolution of the beat wave in inhomogeneous plasmas through $\omega_p(x)$. It has been shown that in homogeneous plasmas there exists a mechanism whereby the amplitude of the beat wave is limited[6]. We now consider the beat wave process in plasmas containing density inhomogeneities for the purpose of determining what other processes, if any, can limit the beat wave amplitude. We consider inhomogeneities or spatial fluctuations of the form

$$n(x) = n_o\ (1 + \epsilon \sin k_i x) \qquad (12)$$

This form of an inhomogeneity is particularly interesting since (1) A sinusoidal ripple is easily excited under beat wave experimental conditions due to the cogeneration of low frequency ($\omega_{ac} << \omega_p$) SBS driven ion acoustic waves and (2) An arbitrary inhomogeneity can be decomposed into its spatial Fourier components. The understanding of how one such component scatters the beatwave gives insight into how the beat wave would be affected by an arbitrary inhomogeneity. In the development which follows we will be particularly interested in characterizing the growth and maximum amplitude of the beat wave.

Some insight into the problem can be gained prior to any further mathematical manipulations. We have already observed that the plasma responds to a driving force of frequency ω_{po} much as a simple harmonic oscillator of natural frequency ω_p. The magnitude of the response depends on how well the frequencies of the oscillator and driver are matched. In a plasma containing a ripple

$n = n_o(1 + \varepsilon \sin k_i x)$, where $\omega_p(n_o) = \omega_{po}$, the response at the points along x where $\sin(k_i x) = 0$ will be large while the response at points where $\sin(k_i x) = 1$ will be weaker. Other points in the profile will have some intermediate response. At some time t the waveform E(x) will have a variation in x with one component of spatial periodicity $2\pi/k_i$. Since $k_{driver} = \Delta k$ is small for waves with $v_\phi \cong c$, the driver may be considered nearly uniform in space over many density ripple wavelengths, $\lambda_i = 2\Pi/k_i$. Although the driver is nearly uniform in x the resulting waveform develops spatial Fourier components with $k \cong k_i$. Since the response is nonlinear in $\omega_p - \omega_{po}$, E(x) does not simply follow n(x) but instead has a complex k-spectrum whose components consist of the various spatial harmonics of k_i.

To rigorously treat the evolution of the beat wave excited in a plasma containing a density ripple we return to the solution of Eq. 9 given by Eq. 10 and adopt the complex notation

$$E(x,t) = \frac{1}{2i}\left[\, y(x,t) - \text{complex conjugate} \,\right] \qquad \text{where} \qquad (13)$$

$$y(x,t) = \frac{\omega_{po}^2 F}{(\omega_p^2 - \omega_{po}^2)} \Bigg[\exp\left\{i(k_p x - \omega_{po} t)\right\} - \exp\left\{i(k_p x - \omega_p t\ )\right\}$$

$$- \frac{\omega_p - \omega_{po}}{2\omega_p}\left[\ \exp\left\{i(k_p x + \omega_p t)\right\} - \exp\left\{i(k_p x - \omega_p t)\right\}\right]\Bigg] \qquad (14)$$

where as before $\omega_p = \omega_p(x)$, $\omega_p(n_o) = \omega_{po}$, $F = \alpha_1\alpha_2/2$, and $E = E_1/E_{cold}$. We consider small density ripples

$$n(x) = n_o\Big[\, 1 + \varepsilon \sin k_i x \,\Big], \quad \varepsilon \ll 1 \tag{15}$$

so that

$$\omega_p(x) = \omega_{po}\Big[\, 1 + \varepsilon \sin k_i x \,\Big]^{1/2} \cong \omega_{po}\Big[\, 1 + \frac{\varepsilon}{2} \sin k_i x \,\Big] \tag{16}$$

Substitution of this form of ω_p into Eq. 14 and rearranging terms yields

$$y = \frac{\omega_{po}^2 F}{(\omega_p^2 - \omega_{po}^2)} \exp\Big\{ i(k_p x - \omega_{po} t) \Big\} \times$$

$$\Bigg[1 - \exp\Big\{ -i \frac{\varepsilon\omega_{po} t}{2} \sin k_i x \Big\} + \frac{\varepsilon}{4} \sin k_i x \times$$

$$\Big[\exp\Big\{ -i \frac{\varepsilon\omega_{po} t}{2} \sin k_i x \Big\} - \exp\Big\{ i\omega_{po} t \,(2 + \frac{\varepsilon}{2} \sin k_i x) \Big\} \Big] \Bigg] \tag{17}$$

Writing $-i\frac{\varepsilon\omega_{po} t}{2} \sin k_i x = i\frac{\varepsilon\omega_{po} t}{2} \sin(-k_i x)$ and applying the Bessel identity

$$\exp\Big\{ i x \sin\theta \Big\} = \sum_{n=-\infty}^{+\infty} J_n(x) \exp\Big\{ i n\theta \Big\}$$

Eq. 17 becomes

$$y = \frac{\omega_{po}^2 F}{(\omega_p^2 - \omega_{po}^2)} \left[e^{i(k_p x - \omega_{po} t)} - \sum_{n=-\infty}^{+\infty} J_n\left(\frac{\varepsilon \omega_{po} t}{2}\right) \exp\left\{ i \left[(k_p - nk_i) - \omega_{po} t \right] \right\} + \right.$$

$$\frac{\varepsilon}{4} \sum_{n=-\infty}^{+\infty} J_n\left(\frac{\varepsilon \omega_{po} t}{2}\right) \sin k_i x \left[\exp\left\{ i \left[(k_p - nk_i) x - \omega_{po} t \right] \right\} - \right.$$

$$\left. \left. \exp\left\{ i \left[(k_p + nk_i x) + \omega_{po} t \right] \right\} \right] \right]$$

From the definition of E in Eq. 13, it follows that the electric field can be written as

$$E(x,t) = \frac{\omega_{po}^2 F}{(\omega_p^2 - \omega_{po}^2)} \left[\sin\Psi_o - \sum_{n=-\infty}^{+\infty} J_n\left(\frac{\varepsilon \omega_{po} t}{2}\right) \sin(\Psi_o - nk_i x) + \right.$$

$$\left. \frac{\varepsilon}{4} \sum_{n=-\infty}^{+\infty} J_n\left(\frac{\varepsilon \omega_{po} t}{2}\right) \sin k_i x \left[\sin(\Psi_o - nk_i x) - \sin(\bar{\Psi}_o + nk_i x) \right] \right]$$

where $\Psi_o = k_p x - \omega_{po} t$ and $\bar{\Psi}_o = k_p x + \omega_{po} t$. Noting that $\omega_p^2 - \omega_{po}^2 = \varepsilon \omega_{po}^2 \sin k_i x$, the electric field E simplifies to

$$E(x,t) = \frac{F}{\varepsilon} \left[\frac{\sin\Psi_o}{\sin k_i x} - \sum_{n=-\infty}^{+\infty} J_n\left(\frac{\varepsilon \omega_{po} t}{2}\right) \frac{\sin(\Psi_o - nk_i x)}{\sin k_i x} + \right.$$

$$\left. \frac{\varepsilon}{4} \sum_{n=-\infty}^{+\infty} J_n\left(\frac{\varepsilon \omega_{po} t}{2}\right) \left[\sin(\Psi_o - nk_i x) - \sin(\bar{\Psi}_o + nk_i x) \right] \right] \quad (18)$$

Eq. 18 shows the complex electrostatic ω-k spectrum which arises when plasma waves are "resonantly" excited in a rippled density plasma. For the purpose of comparison with experimental results it is of interest to cast Eq. 18 into the form

$$E(x,t) = \sum_{m} a_m(t)\, \exp(i\Psi_m) \quad \text{where } \Psi_m = i\left[(k_p+mk_i) - \omega_{po}t\right]. \qquad (19)$$

In Eq. 19 the coefficients a_j describe the slow time behavior of the various spatial "harmonics" Ψ_m ($k_p + mk_i \cong mk_i$ since $k_p \ll k_i$) of the plasma wave electric field.

To explicitly project out the various Ψ_m components we expand $1/\sin k_i x$ in Eq. 18 in a Fourier series:

$$\frac{1}{\sin k_i x} = \sum_{m=0}^{\infty} 2 \sin\left\{(2m+1)k_i x\right\} \qquad (20)$$

Applying a trigonometric identity and rearranging terms yields

$$E(x,t) = \frac{F}{\varepsilon} \sum_{m=0}^{\infty} \left[\cos\left\{\Psi_o-(2m+1)k_i x\right\} - \cos\left\{\Psi_o+(2m+1)k_i x\right\} \right] -$$

$$\frac{F}{\varepsilon} \sum_{m=0}^{\infty} \sum_{n=-\infty}^{+\infty} J_n\left(\frac{\varepsilon\omega_{po}t}{2}\right) \left[\cos\left\{\Psi_o-\left[n+(2m+1)k_i x\right]\right\} - \cos\left\{\Psi_o-\left[n-(2m+1)k_i x\right]\right\}\right]$$

$$+ \frac{F}{4} \sum_{n=-\infty}^{+\infty} J_n\left(\frac{\varepsilon\omega_{po}t}{2}\right) \left[\cos\left\{\Psi_o-nk_i x\right\} - \cos\left\{\bar{\Psi}_o+nk_i x\right\}\right] \qquad (21)$$

The $a_j(t)$ coefficients are obtained by combining those terms in the sums of Eq. 21 for which $n \pm (2m+1) = j$ and $(2m+1) = j$:

Ψ_0 (beat wave) component:

1^{st} term: no contribution.

2^{nd} term: Consider m=0,1 and n=±1, ±2, and ±3.

$$m=0 \quad n=+1: \qquad \left[\cos(\Psi_0-2k_ix) - \cos(\Psi_0)\right] J_{+1}$$
$$m=0 \quad n=-1: \qquad \left[\cos(\Psi_0) - \cos(\Psi_0+2k_ix)\right] J_{-1}$$

$$m=1 \quad n=+3: \qquad \left[\cos(\Psi_0-6k_ix) - \cos(\Psi_0)\right] J_{+3}$$
$$m=1 \quad n=-3: \qquad \left[\cos(\Psi_0) - \cos(\Psi_0+6k_ix)\right] J_{-3}$$

. . . . . .

3^{rd} term: standing wave terms.

Combining the Ψ_0 terms one finds

$$E(\Psi_0) = \frac{2F}{\varepsilon} \sum_{n=1(\mathrm{odd})}^{\infty} J_n\left(\frac{\varepsilon\omega_{po}t}{2}\right) . \qquad (22)$$

Similarly for the Ψ_{+1} component:

Ψ_{+1} (first coupled mode) component:

1^{st} term: m=0: $-\cos(\Psi_1)$

2^{nd} term: consider m=0,1,2,3 and n=±2,±4,±6,±8:

m=0	n=-2:	$J_{-2}\cos(\Psi_1)$	n=0:	$-J_0\cos(\Psi_1)$
m=1	n=-4:	$J_{-4}\cos(\Psi_1)$	n=2:	$-J_2\cos(\Psi_1)$
m=2	n=-6:	$J_{-6}\cos(\Psi_1)$	n=4:	$-J_4\cos(\Psi_1)$
m=3	n=-8:	$J_{-8}\cos(\Psi_1)$	n=8:	$-J_6\cos(\Psi_1)$
	. . .		. . .	

Since $J_{2n} = J_{-2n}$ one finds

$$E(\Psi_1) = \frac{F}{\varepsilon}\left[J_0\left(\frac{\varepsilon\omega_{po}t}{2}\right) - 1 \right]\cos(\Psi_1) \quad . \tag{23}$$

In the same way the temporal coefficients of the higher-k components follow. In the notation of Eq. 19 we can summarize the results for Ψ_0, Ψ_1, Ψ_2, and Ψ_3:

$$\Psi_0: \quad a_0 = \frac{2F}{\varepsilon}\sum_{n=1(odd)}^{\infty} J_n\left(\frac{\varepsilon\omega_{po}t}{2}\right) = \frac{2F}{\varepsilon}\int_0^t J_0\left(\frac{\varepsilon\omega_{po}t'}{2}\right)d\left(\frac{\varepsilon\omega_{po}t'}{2}\right) \tag{24a}$$

$$\Psi_{\pm 1}: \quad a_{\pm 1} = \mp\frac{F}{\varepsilon}\left[1 - J_0\left(\frac{\varepsilon\omega_{po}t}{2}\right) \right] \tag{24b}$$

$$\Psi_{\pm 2}: \quad a_{\pm 2} = \mp \frac{2F}{\varepsilon}\left[J_3\left(\frac{\varepsilon\omega_{po}t}{2}\right) + J_5\left(\frac{\varepsilon\omega_{po}t}{2}\right) + J_7\left(\frac{\varepsilon\omega_{po}t}{2}\right) + \ldots \right] \tag{24c}$$

$$\Psi_{\pm 3}: \quad a_{\pm 3} = \mp \frac{F}{\varepsilon}\left[1 - J_0\left(\frac{\varepsilon\omega_{po}t}{2}\right) - 2J_2\left(\frac{\varepsilon\omega_{po}t}{2}\right) \right] \tag{24d}$$

The results presented in Eqs. 24 can be verified by numerically calculating the exact solution of Eq. 9 given by Eq. 10 and then examining its Fourier k-spectrum.

In Fig. 1 we have plotted the numerical solution of Eq. 9 with (ε=.04) and without (ε=0) the density ripple. The beat wave driver is incident from the left and has just reached the right hand boundary. For the homogeneous plasma case (ε=0) a coherent beat wave is seen to grow secularly in time (note the linear ramping in x since the back edge of the pulse has had longer time to grow) and the Fourier spectrum shows a single mode at $k = k_p$ as expected. In the rippled plasma case (ε=0.04) higher-k components are also excited and, although the peak amplitude of the waveform still exhibits secular growth with the same growth rate, the relative size of the beat wave component (Ψ_0) is reduced.

In Fig. 2 we have plotted the temporal evolution of the first three k-components (a_0, $a_{\pm 1}$, and $a_{\pm 2}$) of the exact solution, Eq. 10. For the early times shown the exact solutions of Fig. 2 match the small $\varepsilon\omega_{po}t/2$ expressions (Eqs. 24) nearly exactly.

Referring to Fig. 2 it is seen that the two frequency pump

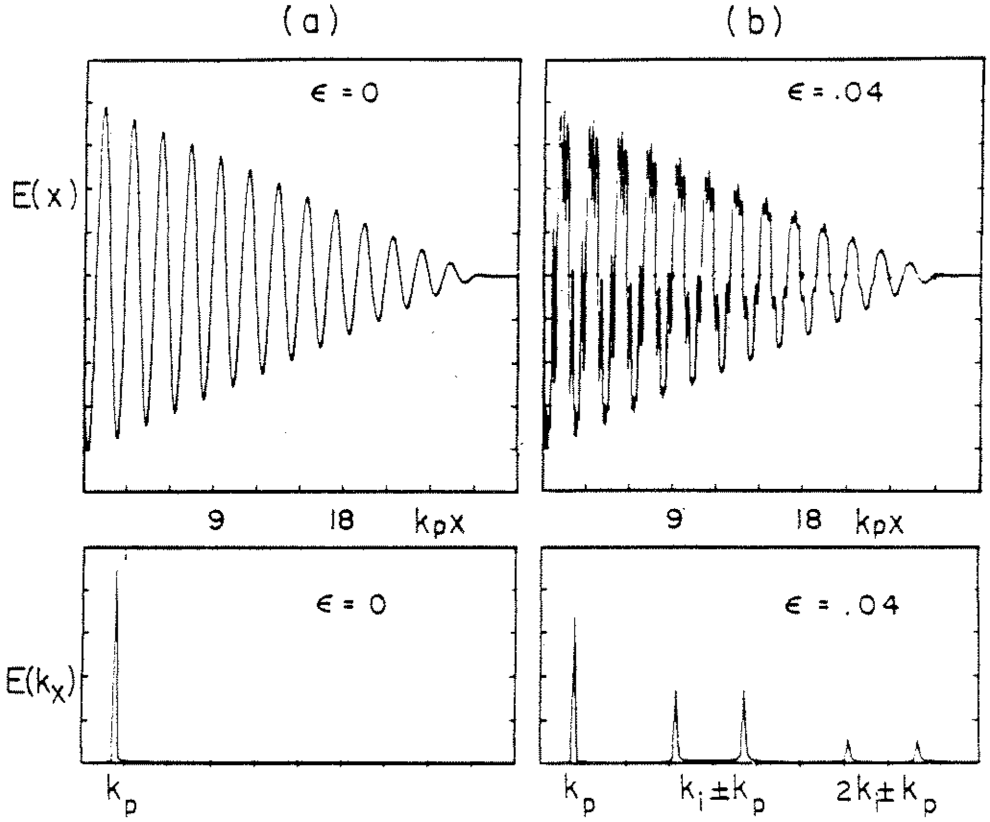

Fig. 1: Spatial evolution of the electric field with (ε = .04) and without (ε = 0) the ripple from the numerical solution of Eq. 9 with $\alpha_1\alpha_2 = 3 \chi 10^{-4}$ and $k_i/k_p = 5$. The spectra are taken at the left hand side of the box. (a) No ripple: $\varepsilon = 0$. (b) With a ripple: $\varepsilon = 0.04$.

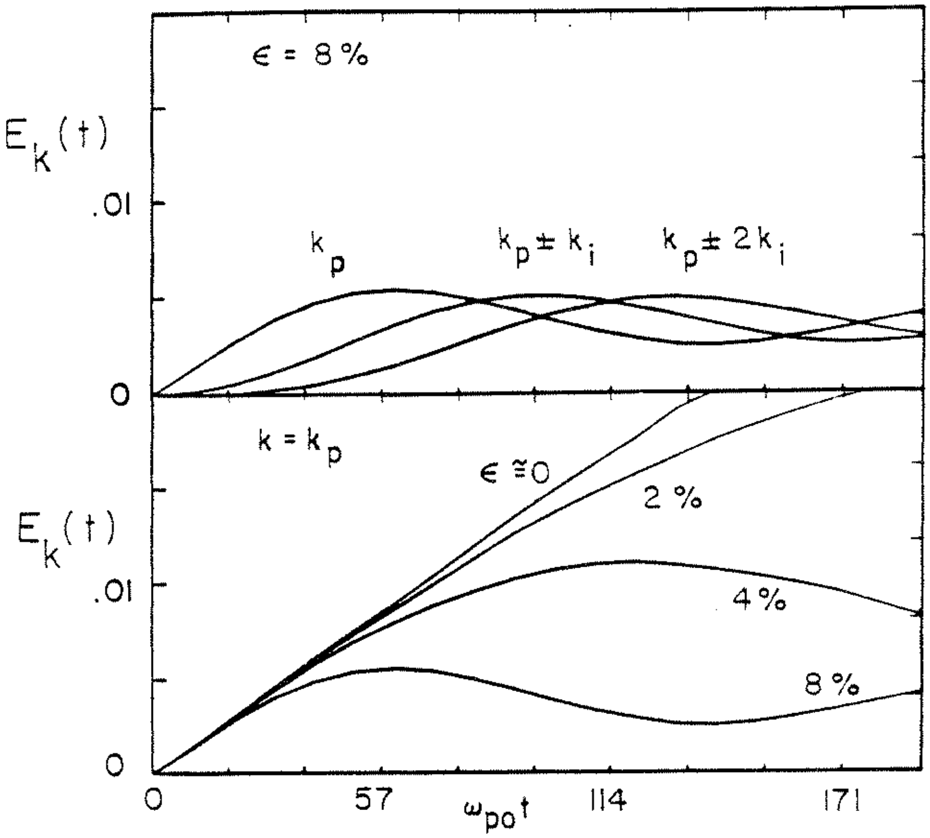

Fig. 2: Temporal evolution of the beat wave and coupled modes with $\alpha_1\alpha_2=3 \times 10^{-4}$. (a) Evolution of beat wave and first two coupled modes Ψ_m, $m = 0 \pm 1, \pm 2$) for $\epsilon = 0.08$ (b) Temporal evolution of beat wave for several ripple amplitudes, ϵ.

excites the beat wave (Ψ_0) component first. However the beat wave rapidly saturates as wave energy is coupled out of the beat wave and into the first coupled mode ($\Psi_{\pm 1}$). The first coupled mode begins to grow but then saturates as the second coupled mode is excited, and so on. For the above cold plasma treatment the coupling proceeds indefinitely to higher and higher-k modes.

One should note the limitations of the above formalism due to two approximations which were made in its development. First we neglected higher than first order terms when we expanded $\omega_p(x)$ in Eq. 16. While it reasonable to assume $\varepsilon << 1$, it is still possible that a significant contribution to the exponential phase can be made in Eq. 17 if $\omega_{po}t\varepsilon^2/8 \cong \Pi/10$. Thus the validity of our results is limited to $\omega_{po}t < 2.5/\varepsilon^2$ or, in the worst case in our work, $\omega_{po}t \leqslant 250$. Secondly the calculation (Eq. 9) has been carried out in Eulerian coordinates. This implicitly neglects electron excursions in the plasma wave electric field. In our work these excursions can only be important if the excursions approach the ripple wavelength (assuming $k_p < k_i$) and the electrons sample regions of appreciably different density[10]. Thus the results hold rigorously for $E = n_1/n_0 \leqslant k_p/k_i$.

One of the most significant results of this analysis which is of particular interest to the PBWA is the rapid saturation of the beat wave field amplitude as exhibited in Eq. 24a and in Fig. 2. This saturation can limit the effectiveness of the beat wave acceleration mechanism. The field amplitude of the beat wave at saturation is the subject of the next section.

BEAT WAVE SATURATION BY MODE COUPLING:

From Eq. 24a,

$$a_o = \frac{2F}{\varepsilon}\sum_{n=1(\mathrm{odd})}^{\infty} J_n\left(\frac{\varepsilon\omega_{po}t}{2}\right) = \frac{2F}{\varepsilon}S \quad \text{where} \quad S = \sum_{n=1(\mathrm{odd})}^{\infty} J_n(x), \quad x = \frac{\varepsilon\omega_{po}t}{2}$$

To determine the maximum strength to which the beat wave field grows we maximize S:

$$\left.\frac{\partial S}{\partial x}\right|_{x_o} = 0 = \sum_{n=1(\mathrm{odd})}^{\infty} J_n'(x_o) = \frac{1}{2}\sum_{n=1(\mathrm{odd})}^{\infty} (\ J_{n-1} - J_{n+1}\ )$$

$$= \frac{1}{2}\left[(J_o+J_2+\ldots)-(J_2+J_4+\ldots)\right] = \frac{1}{2}J_o(x_o)\ .$$

Thus S has its extremum at x_o where x_o=2.3937... is the first zero of J_o. Using the identity

$$\sum_{n=1(\mathrm{odd})}^{\infty} J_n(x_o) = \sum_{n=0}^{\infty} J_{2n+1}(x_o) = \frac{1}{2}\int_0^{x_o} J_o(x)dx$$

and performing the integration numerically yields S_{max} = 0.735 and

$$E(\Psi_o,\ \text{saturation}) = 0.735\ \frac{2F}{\varepsilon} \tag{25a}$$

with $\tau_{sat}(\Psi_0) \cong 4.8(\epsilon\omega_p)^{-1}$. Similarly, it is found that

$$E(\Psi_{\pm1}, \text{ saturation}) = 0.701 \frac{2F}{\epsilon} \qquad (25b)$$

with $\tau_{sat}(\Psi_{\pm1}) \cong 7.7(\epsilon\omega_p)^{-1}$.

Before comparing the characterists of beat wave saturation for mode coupling and relativistic detuning we consider the effects of finite electron temperature on the mode coupling beat wave saturation mechanism.

THERMAL EFFECTS:

Mode coupling brings about a saturation of the beat wave because energy which is pumped into the primary (beat wave) mode couples rapidly to an infinite number of higher-k modes. When the rate at which energy is coupled to these secondary modes equals the rate at which driver energy is supplied to the primary mode, the primary mode saturates; i.e. the beat wave saturates.

The introduction of a finite temperature alters the previous estimates of the mode coupling saturation times and amplitudes. Because the frequency difference between the primary mode and the m^{th} coupled mode increases with m (due to the finite Bohm-Gross frequency shift) only a finite number of secondary modes are excited to appreciable amplitudes since the maximum frequency difference allowed is equal to the variation of $\omega_p(x)$ within the density ripple. The larger the Bohm-Gross shift or the smaller the ripple depth ε, the smaller the number of eligible secondary modes[7,8].

The effect of finite temperature on the saturation is due to the finite number of coupled modes and the coupling efficiency for the off-resonance modes. Since primary mode energy has fewer avenues for depletion, the primary (beat wave) grows to a larger amplitude before saturating. We can also expect a longer saturation time.

To analytically take thermal effects into consideration we recall that the cold plasma solution can be written as

$$E(x,t) = \sum_m a_m(t) \exp \left\{ i(k_p - mk_i)x - \omega_{po}t \right\} . \qquad (26)$$

In the case of a warm plasma we have argued that only a finite number of secondary modes are eligible for coupling. We therefore approximate E(x,t) by truncating the summation in Eq. 26. For simplicity we allow only the first coupled modes $(n = \pm 1)$:

$$E_{warm} = a_0 e^{i\Psi_0} + a_{+1} e^{i\Psi_{+1}} + a_{-1} e^{i\Psi_{-1}} + \text{C.C.}$$

where again, $\Psi_0 = k_p x - \omega_{po} t$ and $\Psi_{\pm 1} = (k_p \pm k_i)x - \omega_{po} t$. Upon substitution of this form of a solution into the wave equation for E(x,t) (Eq. 9),

$$\ddot{E} + \omega_{po}^2(1 + \varepsilon \sin k_i x)E + c_e^2 E'' = F\omega_{po}^2 \sin(k_p x - \omega_{po} t)$$

we obtain three equations for the three a-coefficients above:

$$\dot{a}_0 + \frac{\varepsilon}{4}(a_{-1} - a_{+1}) - \frac{(c_e k_p/\omega_p)^2}{2i} a_0 - \frac{F}{4} = 0 \tag{27a}$$

$$\dot{a}_{+1} - \frac{1}{2i}\left[c_e(k_p + k_i)/\omega_p\right]^2 a_{+1} + \frac{\varepsilon}{4} a_0 = 0 \tag{27b}$$

$$\dot{a}_{-1} - \frac{1}{2i}\left[c_e(k_p - k_i)/\omega_p\right]^2 a_{-1} - \frac{\varepsilon}{4} a_0 = 0 \tag{27c}$$

Eqs. 27 govern the slow time behavior of the beat wave and first two coupled modes in a warm plasma. To determine the temporal evolution of the beat wave and coupled modes in a finite temperature plasma containing a density ripple we proceed to decouple Eqs. 27 and solve for a_0 and $a_{\pm 1}$. Differentiating Eq. 27a with respect to time and substituting Eqs. 27b,c we obtain an equation for a_0:

$$\ddot{a}_0 - \dot{a}_0(k_i/2i)^2 + a_0 \frac{\varepsilon^2}{8}\left[1 - 2(k_i/\varepsilon)^2(k_p/k_i)^2\right] + \frac{Fk_i^2}{8} = \frac{F}{4}\delta(t) \tag{28a}$$

where we have used the normalization $\dot{a}_0 = \dfrac{\partial a}{\partial(\omega_{po}t)}$ and the k's appearing in Eq. 28 have been normalized to ω_{po}/c_e (i.e. k_p is really $k_p c_e/\omega_{po}$). Similarly one finds for the coupled modes

$$\dot{a}_{\pm 1} - \frac{1}{2i} (k_p \pm k_i)^2 \, a_{\pm 1} = \mp \frac{\varepsilon}{4} a_0 \tag{28b}$$

The δ-function driver arises when one differentiates the driver force F which is represented by a step function turning on at t=0. The effect of this δ-function driver on a_0 is that a_0 receives an impulsive "kick" at t=0 such that $\dot{a}_0(0) = F/4$ while maintaining $a_0(0)=0$. Defining $a=(k_i/2)^2$ and keeping only the lowest order terms in k_p/k_i Eqs. 28a,b become

$$\ddot{a}_0 + 2ia\dot{a}_0 + \frac{\varepsilon^2}{8} a_0 = \frac{F}{4} \delta(t) - \frac{Fa}{2i} \tag{29a}$$

$$\dot{a}_{\pm 1} - \frac{1}{2i} k_i^2 \, a_{\pm 1} = \mp \frac{\varepsilon}{4} a_0 \tag{29b}$$

Noting that the particular solution of Eq. 29a differs from the homogeneous solution only by the constant Fa/2i (time independent driver for arbitrary times), one can first solve for a_0 subject to the initial conditions above and then substitute a_0 into Eq. 29b and obtain $a_{\pm 1}$. One finds

$$a_0 = \frac{4iFa}{\varepsilon^2} \left[1 - \left[\frac{c+1}{2c} + \frac{\varepsilon^2}{32a^2c} \right] e^{-ia(1-c)t} - \left[\frac{c-1}{2c} - \frac{\varepsilon^2}{32a^2c} \right] e^{-ia(1+c)t} \right] \tag{30a}$$

$$a_{\pm 1} = \frac{\mp F}{2\varepsilon} \left[1 - \left[\frac{c+1}{2c} \right] e^{-ia(1-c)t} - \left[\frac{c-1}{2c} \right] e^{-ia(1+c)t} \right] \qquad (30b)$$

where $c = (1 + 2\varepsilon^2/k_1^2)^{1/2} = (1 + \varepsilon^2/8a^2)^{1/2}$ and, as before, $a=(k_1/2)^2$. Recalling that the beat wave and first coupled mode components are given by

$$E_{bw} = a_0 e^{i\Psi_0} + a_0^* e^{-i\Psi_0}$$

$$E_{\pm 1} = a_{\pm 1} e^{i\Psi_{\pm 1}} + a_{\pm 1}^* e^{-i\Psi_{\pm 1}}$$

one can write

$$E_0 = \frac{-2Fp}{\varepsilon} \left[\sin\Psi_0 - C_1 \sin(\Psi_0 - B_1 t) - C_2 \sin(\Psi_0 - B_2 t) \right] \qquad (31a)$$

$$E_{\pm 1} = \frac{\mp F}{\varepsilon} \left[\cos\Psi_{\pm 1} - A_1 \cos(\Psi_{\pm 1} - B_1 t) - A_2 \cos(\Psi_{\pm 1} - B_2 t) \right] \qquad (31b)$$

where $A_1 = \frac{c+1}{2c} \qquad A_2 = \frac{c-1}{2c} \qquad (32a)$

$$B_1 = \frac{\varepsilon p}{4}(1-c) \qquad B_2 = \frac{\varepsilon p}{4}(1+c) \tag{32b}$$

$$C_1 = A_1 + \frac{1}{2cp^2} \qquad C_2 = A_2 - \frac{1}{2cp^2} \tag{32c}$$

and p is a thermal parameter defined by $p = 3(k_i c_e/\omega_p)^2/\varepsilon = 3(k_i\lambda_d)^2/\varepsilon$. Eqs. 31 describe the temporal evolution of the beat wave and first coupled modes in a finite temperature plasma. These results are presented in Fig. 3 where we have shown the temporal evolution of the beat wave and first coupled modes for one value of the thermal parameter p. In the cold plasma limit of the warm plasma model the beat wave and first coupled modes are seen to oscillate in time as energy is coupled back and forth between the three plasma modes (Ψ_0 and $\Psi_{\pm1}$) and the pump. As expected beat wave saturation is observed to occur. For warm plasmas ($p>0$) the beat wave saturates at higher amplitudes and at later times due to weaker coupling induced by the increase with temperature of the Bohm-Gross frequency mismatch between the fixed frequency driver at ω_{po} and the coupled modes. The coupled modes are observed to attain lower amplitudes for the same reason.

As in the case of cold plasmas energy supplied by the pump is distributed among the beat wave and coupled modes ($n = \pm1$). This diversion of pump energy from the beat wave again leads to beat wave saturation. From Eqs. 31 the warm plasma beat wave saturation amplitude and saturation time are found to be

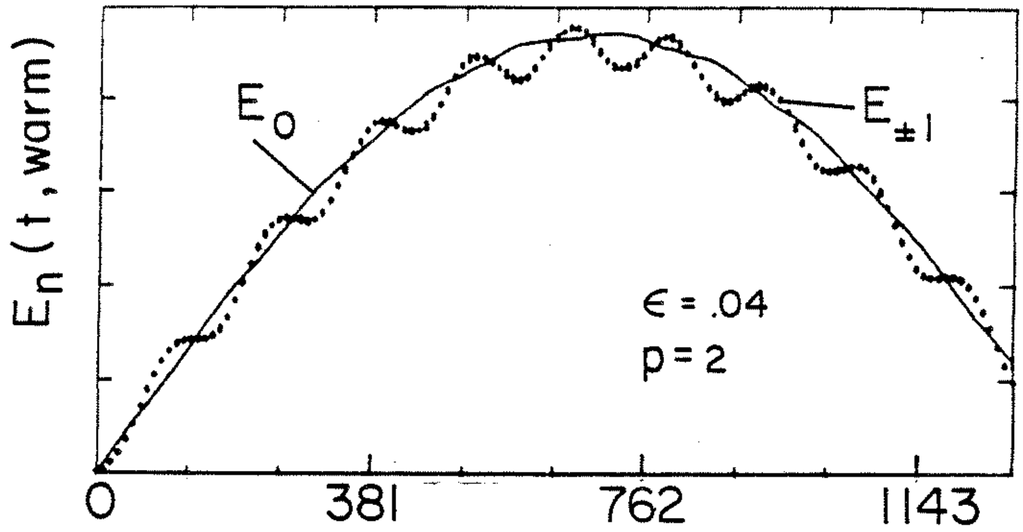

Fig. 3: Temporal evolution of the beat wave and first coupled mode from the warm plasma results of Eq's. 31,32 for $\alpha_1\alpha_2 = 3 \times 10^{-4}$, $\epsilon = 0.04$, and $p = 2$. The Ψ_0 component is plotted on a different scale and at saturation reaches roughly twice the amplitude of the first coupled mode for these parameters.

$$E_{bw}(\text{sat'n.}) = \frac{2F}{\varepsilon} \times f(p), \qquad f(p) = \left[p + (1+p^2)(2+p^2)^{-1/2} \right] \quad (33a)$$

$$\omega_{po} t_{sat}(\text{beat wave, warm}) \cong 12\ p/\varepsilon \quad (\text{for } p \geqslant .05) \quad (33b)$$

$$E_{\pm 1}(\text{sat'n.}) = \frac{2F}{\varepsilon} \quad (33c)$$

$$\omega_{po} t_{sat}(\Psi_{\pm 1}, \text{warm}) \cong 12p/\varepsilon \quad (33d)$$

One can see that the beat wave saturation amplitude is enhanced by the factor f(p) $\geqslant 2$ over that expected in cold plasma (Eq. 25a).

A reasonable question at this point is, to what extent the saturation amplitude estimate provided by Eq. 33 is valid since the assumption of coupling only to the $m = \pm 1$ modes seems somewhat arbitrary. Clearly in an experiment one would expect the parameters to be such that an exact treatment would lie somewhere between the two extremes (cold and warm) considered here. The warm plasma result of Eq. 33 can be checked in the limit of p approaching zero (cold plasma). It is easily shown that

$$\lim_{p \to 0} E_{bw}(\text{warm, sat.}) = .707\ \frac{2F}{\varepsilon} \quad \text{with } \tau_{sat} = (\varepsilon\omega_{po})^{-1} \quad (34)$$

in excellent agreement with the cold plasma estimate of Eq. 25a. This remarkable agreement is due to the fact that, at the time of saturation of the beatwave, the higher order coupled modes ($m>1$)

have had insufficient time to grow to an appreciable amplitude and therefore contribute little to the total electric field as is evident in Fig. 2. This result justifies the truncation used in obtaining Eq. 34. since p=0 provides a worst case check of this approximation.

RELATIVE IMPORTANCE OF SATURATION BY MODE COUPLING:

The relative importance of mode coupling as a beat wave saturation mechanism can be assessed by comparing the beatwave amplitude at saturation for the mode coupling and relativistic detuning cases. Recalling the beat wave saturation amplitudes for these two cases[6],

$$\text{Relativistic Detuning:} \qquad E_{bw}(\text{sat}) = \left[\frac{16}{3} \alpha_1 \alpha_2 \right]^{1/3} \qquad (35a)$$

$$\text{Mode Coupling:} \qquad E_{bw}(\text{sat}) = \frac{\alpha_1 \alpha_2}{\epsilon} f(p) \qquad (35b)$$

it can be seen that saturation by mode coupling dominates over that due to relativistic detuning whenever

$$\alpha_1 \alpha_2 < \left[1.6 \epsilon f(p) \right]^{3/2} \qquad (36)$$

For example in the case of a modest ripple size of $\epsilon \cong 4\%$ and a moderately warm plasma of $p \cong 2$, it is seen that saturation by mode coupling dominates unless $\alpha > .04$ (assuming equal laser line intensities, $\alpha_1 = \alpha_2$) or $I(CO_2) > 4 \times 10^{13}$ W/cm^2. Although the calculations used to arrive at these thresholds have not included pump risetimes it is evident that this new saturation mechanism can be quite important in moderate intensity or short wavelength laser experiments.

PROPERTIES OF COUPLED MODES:

Until now we have focussed on mode coupling as a beat wave saturation mechanism. However the higher-k modes which are generated are of interest in their own right because (1) the higher-k modes, unlike the high phase velocity beat wave, can interact strongly with the background electrons and (2) the generation of an infinite number of higher-k modes can lead to a quasi-turbulent electrostatic spectrum which is highly undesirable for particle acceleration[2].

Although real-life plasmas would ideally be studied for a parameter regime lying somewhere between the two extremes of the warm plasma and cold plasma models, a great deal can be inferred about the spectrum of the coupled modes from the cold plasma treatment. Eqs. 24 give the temporal evolution of the first few coupled modes as inferred from the total electric field given in Eq. 21.

The most distinguishing signature of the electrostatic mode coupling spectrum for cold (and cool) plasmas is the presence of modes which are fundamental in ω_p but harmonic in the ripple wavenumber k_i: $\omega \cong \omega_{po}$, $k = k_p \pm mk_i \cong \pm mk_i$ ($k_p << k_i$). Although an infinite number of wavenumber harmonics are generated only a finite number can be expected to be observed experimentally, even in cool plasmas, due to the steady increase of $k\lambda_d$ with m for the higher order coupled modes. The relative amplitudes of the various coupled modes can be calculated from Eqs. 24. However, since Eqs. 24 are calculated in the cold plasma limit, estimates of the relative amplitudes can only be approximated for real-life plasmas since these equations do not take into consideration the mismatch between the driver frequency (ω_{po}) and the Bohm-Gross frequency (ω_{BG}). Qualitatively Eqs. 24 and Fig. 2 show that the coupled modes also undergo saturation with the higher order modes saturating at later times and slightly lower amplitudes than the lower order modes. In finite temperature plasmas one can expect these modes to saturate at even earlier times and at lower amplitudes. This has already been seen in the case of the beat wave (c.f. Eqs. 25a and 33).

Another important signature of the electrostatic spectrum is its near symmetry in k. Eqs. 21 and 24 show explicitly that modes with both plus (Ψ_{+m}) and minus (Ψ_{-m}) k's are excited. For the mth order coupling the respective k's are $k_{+m} = k_p + mk_i \cong mk_i$ and $k_{-m} = k_p - mk_i \cong -mk_i$ in the underdense plasmas considered here where $k_p << k_i$. In this case modes with equal and opposite k's are expected. This feature will be discussed in greater detail in a later section.

OTHER COUPLING MECHANISMS:

So far we have considered the beat excitation of electron plasma waves by two laser beams whose frequencies differ by the mean plasma frequency ω_p. In the context of the PBWA the two laser beams are assumed to be incident on the plasma from the same direction so that the ponderomotive force of the beating lasers, and therefore the driven plasma wave, have $\vec{k}_p \cong \vec{k}_1 - \vec{k}_2$ and consequently $v_\phi \cong c$.

In a realistic experimental situation both laser beams can be expected to idependently undergo stimulated Brillouin scattering. In such a situation the effective driver consists of not only the beat envelope of the copropagating beams but also the envelope resulting from the beating of one incident laser line with the SBS backscatter from the other line. The latter contribution drives plasma waves with wavenumbers $k_{cpom} \cong k_1 + k_2', k_1' + k_2 \cong 2k_1 \cong 2k_2$ where the subscript cpom denotes "counter propagating optical mixing"[11] and the primes indicate the wavenumbers of the j^{th} pump component ($k_j \cong k_j'$ since $\omega_{ac} << \omega_1, \omega 2$). The direction of propagation of these large-k, low phase velocity waves can be forward or backward: assuming $|\vec{k}_2| < |\vec{k}_1|$,

$$\vec{k}_{cpom} = \vec{k}_2 - \vec{k}_1' = (k_2 + k_1')\hat{x} \cong +\vec{k}_i \qquad (37a)$$

$$\vec{k}_{cpom} = \vec{k}_2' - \vec{k}_1 = -(k_2' + k_1)\hat{x} \cong -\vec{k}_i \qquad (37b)$$

The modes excited by counter propagating optical mixing are seen to closely resemble modes generated by mode coupling of the high phase velocity beatwave. This direct generation mechanism for waves with $\omega \cong \omega_p$ and $k \cong k_i$ leads to ambiguities in the experimentally measured electrostatic spectrum because of the difficulty of resolving the subtle frequency and wavenumber differences between the COM and CPOM generated modes.

The previously introduced beat wave excitation model can be modified to facilitate the study of the CPOM problem by replacing the driver in Eq. 9 with its CPOM equivalent,

$$\ddot{E} + \omega_{po}^2(x)E + c_e^2 E'' = \omega_{po}^2 F_{cpom} \sin(\Delta kx - \Delta\omega t) \qquad (38)$$

where (for CPOM) $\Delta k = \pm \left[|\vec{k}_1| + |\vec{k}_2| \right] \cong k_i$, $k_p = |\vec{k}_1 - \vec{k}_2|$ as before, and $F_{cpom} = \frac{1}{2} \alpha_1 \alpha_j' \left[\frac{\Delta k}{k_p} \right]$ is the normalized laser intensity modified for the larger-k CPOM beat envelope and to take into account the fact that one pump component (α_j') has been fostered by SBS. The analysis following Eqs. 9 and 10 is general and one can therefore write the CPOM driven plasma wave electric field in the same form as given in Eqs. 21 and 24. Noting that for CPOM $\Psi_m(\text{cpom}) = \Delta k \pm mk_i \cong (m\pm1)k_i = \Psi_{m\pm1}$for forward/backward propagating $k = k_i$ modes, the CPOM field is

$$E_{CPOM} = \sum_{m=-\infty}^{\infty} a_m \cos\Psi_{m\pm1} \tag{39}$$

where the a_m are as given in Eqs. 24. The CPOM field, unlike the COM field, is seen to be asymmetric in its indices; the $(m\pm1)^{th}$ coupled mode grows as a_m. The zero-order or beatwave component is a $k = k_i$ wave; the first coupled modes are the $k = 0$ and $k = 2k_i$ modes; the second coupled modes are the $k = -k_i$ and $k = 3k_i$ modes and so on.

In an attempt to resolve the ambiguity which arises when both CPOM and COM are possible it is natural to ask to what amplitude the resulting CPOM fields are driven. Eq. 39 indicates that the saturation behavior of the $(m+1)^{th}$ coupled mode is governed by the m^{th} temporal coefficient (c.f. Eqs. 24). For example, assume conditions are such that a forward propagating ($\vec{k} = \vec{k}_i$) beat wave is excited. The beat excited wave evolves as $a_0(t)$ given in Eq. 24a and therefore saturates at an amplitude

$$E(\text{CPOM, sat}) = .735\ \frac{2F_{CPOM}}{\varepsilon} \quad . \tag{40}$$

Comparing the COM (Eq. 25b) and CPOM (Eq. 40) $k = k_i$ mode saturation amplitudes one finds that

$$\frac{E(\mathrm{CPOM,sat})}{E(\mathrm{COM,sat})} = (\alpha_j'/\alpha_j)\ (\Delta k/k_p) \qquad (41)$$

For PBWA experiments, where large $\gamma_{phase} = \omega_0/\omega_p$ is desirable, we take a typical value of $\omega_0/\omega_p \cong 10$ or $\Delta k/k_p \cong 20$. CPOM can in this example provide a significant or possibly dominant contribution to the experimentally detected levels of $k = k_i$ electrostatic modes when

$$\alpha_j'/\alpha_j \cong \left[I_{SBS}/I_{incident}\right]^{1/2} \cong 1/20 \quad \text{or } I_{SBS}/I_{incident} \cong 1/4\ \% \ , \qquad (42)$$

a condition easily met in most high intensity laser experiments. Finer points of the CPOM excitation mechanism will be addressed in a later section.

MODE COUPLING OF PLASMA WAVES DRIVEN BY SRS:

In the context of the PBWA the subject of mode coupling has arisen as an incidental process encountered while attempting to excite large amplitude, high phase velocity electron plasma waves for the purpose of particle acceleration. Although the importance of mode coupling as a beat wave saturation mechanism has been demonstrated, we have thus far said little regarding its more widespread implications and the role it can play in physical situations other than the PBWA.

An example of such a physical situation is that of stimulated

Raman scattered (SRS) of incident laser light. In SRS a single frequency laser beam is incident on an underdense plasma ($\omega_{laser} < \omega_p/2$). For sufficient laser intensity the nonlinear current from the ponderomotive force of the laser acting on thermal density fluctuations ($\tilde{\omega},\tilde{k}$) emits radiation which beats with the incident radiation (laser) and reinforces the initial density fluctuation. This perturbation grows exponentially in time to form a plasma wave. Note that the frequency of the resulting plasma wave may or may not equal the plasma wave frequency obtained under beat excitation. SRS is usually envisioned to occur in plasmas with sufficiently long density gradient scale lengths so that em-es ω and k matching is maintained over sufficient distance to generate coherent electromagnetic backscatter. When quasistatic small scale density fluctuations are present such that $k_i < 2\pi/L_n$, $L_n = (\frac{1}{n}\frac{\partial n}{\partial x})^{-1}$, mode coupling of the SRS driven plasma waves can occur resulting in the excitation of modes with $k = k_{SRS} + mk_i$. In underdense plasmas, $k_{SRS} \cong k_i$ ($\omega_p << \omega_{laser}$) and the driven and coupled modes have wavenumbers given respectively by k_i and $(1 \pm m)k_i$. Unlike the CPOM case the possibility of both the $+k_i$ and $-k_i$ modes exists without two frequency laser excitation; i.e. when operating the laser on a single line the spectral ambiguity encountered in two frequency operation is not encountered. Detection of a backward propagating electrostatic $k = k_i$ mode is conclusive evidence for the mode coupling process.

The analysis of SRS in the presence of a ripple is far less straight forward than for beat excitation. One crude approach is to consider the evolution of the plasma wave from a coherent oscillation to the coupled spectrum. In this approach the work of Kaw, Lin, and Dawson[8] is applicable. However a more realistic approach is to consider how the SRS and ripple (SBS) interdependently evolve together in time. Such a view has been taken by Aldrich et al.[12] who have solved a set of coupled fluid equations for the electromagnetic vector potential and the particle fluctuations at quarter-critical density. When the ion and plasma waves (SBS and SRS) are decoupled mathematically the SRS and SBS instabilities grow independently with wavenumbers $2k_0$ and $3/2k_0$ respectively (k_0 = pump wavenumber). When the coupling is included the early time behavior is similar to that in the uncoupled case. However at later times the plasma wave electric field phase locks to the $2k_0$ ion fluctuation. This represents the first coupling: $3/2k_0 \rightarrow 7/2k_0, -1/2k_0$. As time progresses the electric field continues to develop spatially. In k-space the coupling continues as $3/2k_0 \rightarrow 7/2k_0, -1/2k_0 \rightarrow 11/2k_0, -5/2k_0 \ldots$. The modes evolve qualitatively much as seen in Fig. 2 and therefore indicate the possibility of saturation of the SRS much as the beat wave saturates due to mode coupling in the presence of an SBS induced ripple. Abrupt quenching of Raman excited plasma waves has been reported by Walsh et al.[14] and Villeneuve et al.[15] have suggested the possibility of mode coupling playing a role in their experiment.

MODE COUPLING IN THE PRESENCE OF SBS HARMONICS:

Thus far we have considered density ripples which we have envisioned to arise from SBS driven ion acoustic waves of wavenumber $k = k_i$ where $k_i \cong 2k_{laser}$. This has been shown to lead to ambiguities in the electrostatic ω,k spectrum when both collinear optical mixing (COM) and counter-propagating optical mixing (CPOM) occur because of the degeneracy of the (ω_p,k_i) mode (and others). Another complication exists if we consider the role of ion wave harmonics[13]. The CPOM and COM coupled mode spectra now contain the components $(1\pm m)k_i$ and $k_p \pm mk_i$ respectively. Assuming that the ion wave harmonics cannot exist without the fundamental it can be seen that not only do degenerecies exist between the COM and the CPOM spectra, but also within each of the spectra individually. For example, in COM the mode $(\omega_p,2k_i)$ can arise from $\left[\omega_p,k_p+2\times(1k_i)\right] \cong (\omega_p,k_i)$ or from $\left[\omega_p,k_p+1\times(2k_i)\right] \cong (\omega_p,2k_i)$. Similar examples hold for CPOM spectrum.

The amplitudes of the modes resulting from mode coupling of ion harmonics can also be expected to be larger than those resulting from coupling from the fundamental because, from Eqs. 24, the saturation amplitudes scale as ε^{-m} where m is the harmonic number.

In this context we point out yet another possible process which can lead to the broadening of the k-spectrum of the plasma waves with $k \cong k_i$ (Raman scatter for $\omega_p << \omega_{laser}$, the Ψ_1 mode in COM or the Ψ_0 mode in CPOM). This is the parametric decay of the plasma wave into a backward propagating plasma wave and an ion acoustic wave: $(\omega_p, k_i) \longrightarrow (\omega_p - \omega_{ac}, -k_i) + (\omega_{ac}, k_i)$[16]. This process can be seeded by the second harmonic of the SBS driven ion wave which has frequency and wavenumber $(2\omega_{ac}, 2k_i)$. An interesting aspect of all these coupling processes is that the evolution of the plasma wave takes place in one spatial dimension. Even here the physics is extremely rich. If one allows for angular scattering even more possibilities exist.

CHAPTER III: EXPERIMENTAL APPARATUS AND PARAMETERS

In this section we describe the experimental apparatus and diagnostics used in obtaining the data which will be presented.

The goal of the experiments reported on here has been to excite and characterize the behaviour of beat-excited plasma waves and to understand other processes which can be influential in the PBWA. The emphasis has been on gaining a fundamental understanding of the beat wave mechanism rather than on demonstrating the acceleration of electrons by the beat excited electron plasma wave. For this reason the experiments performed have been performed using laser parameters which have been scaled down from "optimum" acceleration parameters and allow us to use proven technology which is both flexible and well suited for high data rates (number of shots per day). The use of proven laser technology allows us to concentrate on the physics of the experiment.

SYSTEM OVERVIEW:

Before giving a detailed description of the various subsystems which comprise the experimental system we will give a brief overview. Fig. 4 shows a diagram of the system and is intended as a reference for the following sections.

The target plasma is first created by a capacitive discharge across the gap between two electrodes in about two torr of an air-

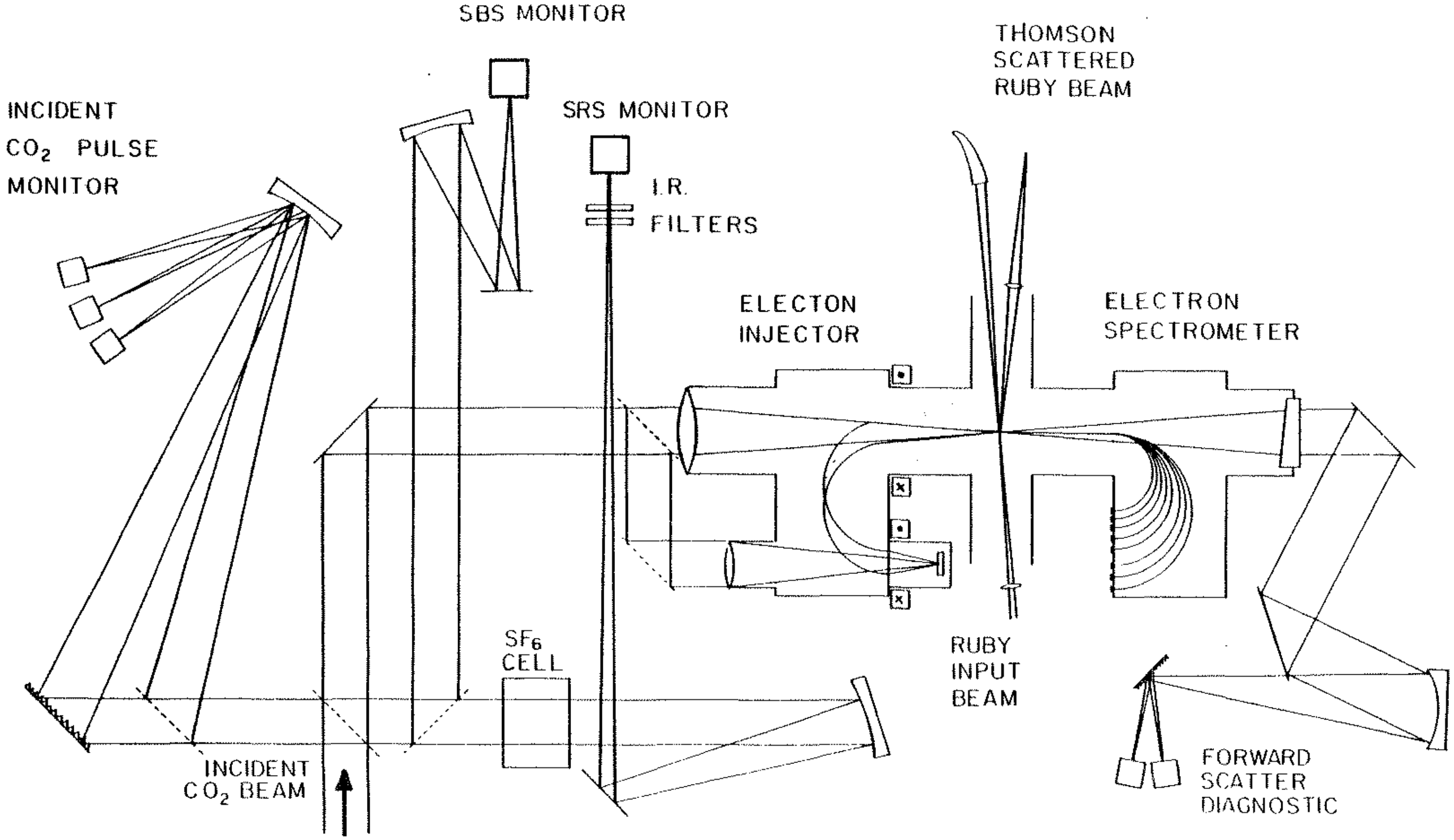

Fig. 4: Diagram of the CO$_2$ laser, Ruby laser, vacuum chamber, and diagnostic systems used in the experiments. The electron injector shown in the above diagram was not used in the experiments described in this thesis.

hydrogen gas mixture. At some specified time after the plasma discharge is initiated, the CO_2 laser oscillator, amplifiers, and diagnostic ruby laser flashlamp are triggered. One pulse, selected from the modelocked CO_2 oscillator output train, is amplified to about 10 - 20 J. and is focused onto the plasma by a lens which serves a second function as a vacuum window on the vacuum vessel. Concurrently a small portion of the CO_2 laser pulse is tapped off and used to trigger a spark gap, which in turn fires the Q-switch of the Thomson scatter diagnostic ruby laser. In this way the timing of the ruby laser pulse can be adjusted such that it and the CO_2 laser pulse arrive simultaneously at the interaction region within the plasma. As the plasma beat wave is created by the two frequency CO_2 laser pulse, ruby laser light is scattered at an angle which depends on the plasma wavenumber. The light emerging at this angle is collected by output optics and transferred by a fiber optic to a spectrograph. The spectra are either time integrated and displayed by a 500 channel optical multichannel analyzer (OMA) or time resolved by a streak camera and recorded on film. Back and forward scattered CO_2 laser light is also analyzed for spectral content and temporal character using either an infrared grating spectrograph or band pass IR filters in conjunction with a liquid helium cooled GeCu detector.

CO_2 LASER SYSTEM:

The CO_2 laser system consists of a TEA oscillator cavity followed by two stages of amplification. This system and its associated optical components are described in detail below.

The oscillator is actively modelocked by a 1 cm^2 × 1 cm germanium Bragg cell which is placed within the cavity at the beam waist. Standing acoustic waves are excited in the germanium by a LiNb piezoelectric transducer which is driven by a pulsed 33 MHz, 50 W peak RF source. These acoustic waves diffract the CO_2 laser beam within the cavity whenever the amplitude of the acoustic wave is non-zero and provides a periodically varying loss within the cavity. When the periodicity of this loss equals the optical round trip time of the cavity the resulting oscillator output is a train of $\cong$ 2 ns (fwhm) pulses separated in time by one round trip transit time of the cavity, $\cong$ 15 ns. To facilitate two frequency operation (for the beat wave experiments) an evacuated cell is situated within the oscillator cavity. For single line operation and for alignment, when more beam energy is desirable, the cell is left evacuated. Two frequency operation is accomplished by introducing traces of absorbing gases (Freon 115, 152) into the cell. The output beam , polarized predominantly in the vertical plane by Brewster windows within the cavity, is passed through a second polarizer. A spark gap driven CdTe Pockels Cell rotates the beam polarization by 90^o for approximately 15 ns insuring that at least one pulse within the train will have an orthogonal polarization. An analyzer, oriented 90^o with respect to the second polarizer, passes only the one rotated pulse and acts as a "switchout" for single pulse operation. The system can also be operated in a "full train" mode by inserting a 1/2-wave plate after the Pockels cell. This allows all but one pulse to pass providing more oscillator beam energy when needed for system alignment.

The switched out pulse is then passed through a 2:1 Keplerian beam expanding telescope. This telescope serves several purposes. It (1) allows more efficient use of the amplifier gain, (2) provides a means for controlling beam divergence, (3) acts as a spatial filter when a pinhole is placed at the focus , and (4) acts as a "plasma shutter" to protect sensitive "upstream" optics from large levels of amplified laser light backscatter. The expanded beam is then double passed through a Lumonics 103 amplifier and amplified to an energy of about 200 mJ.

At this stage the beam is optically stored for about 100 ns to allow sufficient time for build-up of the Thomson scatter ruby laser gain (described below). Following the optical storage leg the beam is double passed through a pair of Lumonincs 600A amplifiers where it is amplified to about 10 J. The final beam is directed by two copper turning mirrors along the vacuum chamber axis (z- axis) where, after passing through an f/7.5 ZnSe lens, it is focused to a spot within the interaction region.

Detailed measurements of the CO_2 laser intensity distrubution at the focus were made. Fig. 5 shows isointensity contours taken on three separate occasions. In all three cases a small sample of

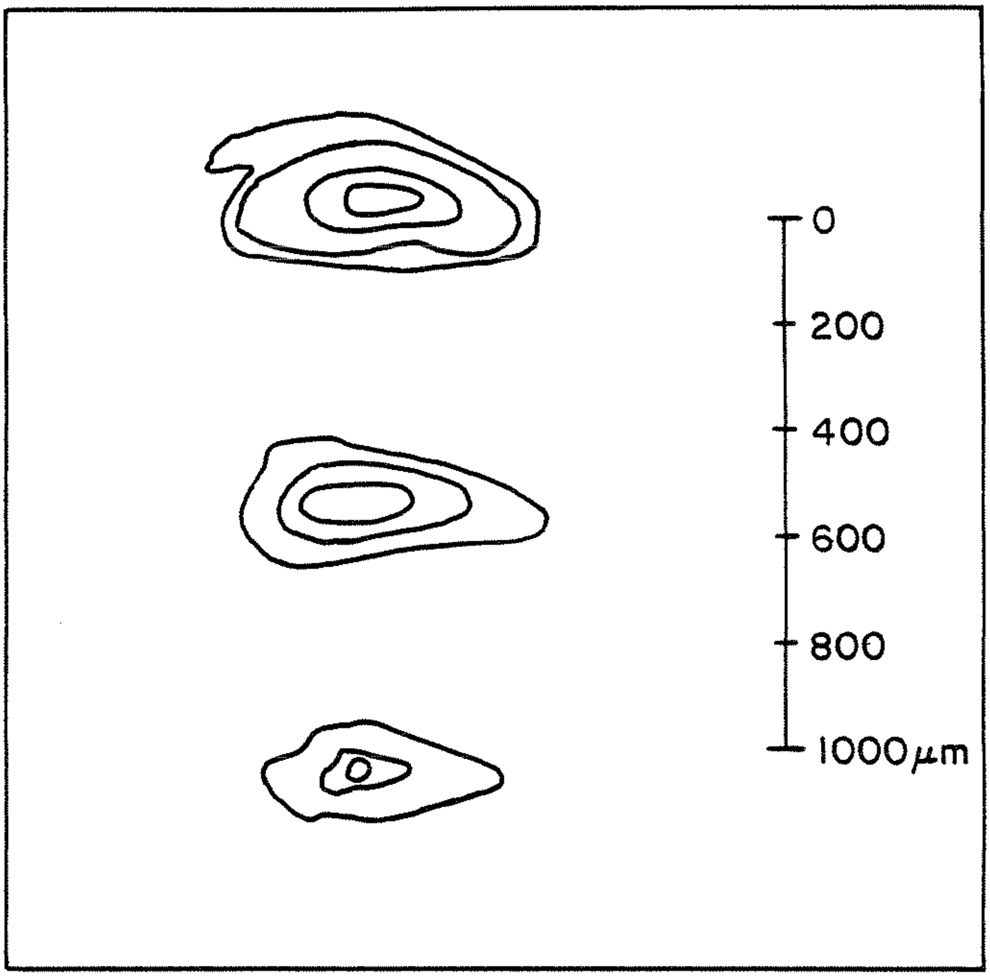

Fig. 5: Isointensity contours of the CO_2 laser beam at its focus obtained on three separate occasions. For all three cases the contours, when fit to a gaussian, indicate a slightly astigmatic focus of approximately 200 × 400 μm.

developed but unexposed black and white negative film was placed axially at the CO_2 laser focus. Starting with no beam attenuation, successive burns were taken while increasing the beam attenuation by a factor of two for each burn. The circumferences of the burns form isointensity contours corresponding to the burn threshold for the film and the level of beam attenuation used for a given shot. The film samples are projected, traced, and superimposed as shown. Because care was taken when aligning the CO_2 laser oscillator to insure, to the extent possible, that the beam consisted exclusively of the TEM_{00} mode, the isointensity contours were fit to a gaussian distribution. The optical configuration employed in the system gave a slightly astigmatic focal spot size of about 200x400 μm.

Prior to entering the focussing optics, the beam passes through a beam splitter which allows us to collect a small portion of both the incident and backscattered laser light (c.f. Fig. 4). The incident light was used to monitor pulse height, shape, energy and spectral content. The backscattered light was used to monitor light which was backscattered by SBS or SRS and, when analyzed for spectral content, provided information on plasma temperature and density respectively.

To monitor forward scattered CO_2 laser light collection optics were placed along the z-axis at the output vacuum port and used to direct the light onto a grating which is mounted on a calibrated rotation stage. The diffracted light was then focused onto a liquid helium cooled, copper doped germanium IR detector. This mono- chromator was calibrated using the various orders of a HeNe test laser and the 10.6 μm line of the CO_2 laser. By tuning the rotation stage we can monitor the wavelength of interest.

THOMSON SCATTERING DIAGNOSTIC

Collective Thomson scattering $(\alpha \geqslant 6)^{17}$ has been used extensively throughout the work reported on in this thesis. The Thomson scattering system consists of the synchronized ruby laser and its associated optics.

The ruby laser flashlamp is first fired by the system master trigger. Deterministic synchronization with the CO_2 laser is achieved by allowing a small portion of the CO_2 laser beam, tapped off just after emerging from the swithchout, to fire a spark gap which drives a Q-switch within the ruby laser cavity. The resulting ruby laser beam pulse has an energy of about 2 J and is about 20 ns in duration.

The ruby laser beam is directed along an axis which is nearly orthogonal to the CO_2 laser beam (c.f. Fig. 4). After sampling the interaction region (plasma waves) a portion of the ruby laser beam is diffracted at an angle which depends on the spatial periodicity $2\pi/k_{es}$ of the electrostatic mode which has been excited in the plasma by the CO_2 laser. In our experiments Thomson scattering measurements have been made in two regimes of scattering angles and plasma wavenumbers: large angle scattering at $7\frac{1}{2}$, 15 and $22\frac{1}{2}$

degrees and small angle scattering at 0.4 degrees.

For large angle Thomson scattering the f-number of the input optics is large enough that the scattered and unscattered components of the ruby laser beam are well separated in space. In this case a spherical optics system was used on both the input and output sections of the Thomson scattering system. Light focused onto the interaction region simply emerges at some angle (which is greater than the 1/f angle of the input optics) and is imaged by a spherical collection lens onto the face of a polished fiber optic for routing to the spectrometer.

If the same optics are used for small angle Thomson scattering ($\cong$ 7 mrad) the scattered and unscattered beams overlap almost completely and cannot be separated. Because the scattered light is typically down by 8 to 10 orders of magnitude from the unscattered beam the spherical optics configuration is unsuitable for small angle scattering. A system which overcomes the difficulties encountered in small angle scattering is described in detail in reference 18. The most important features of this system are described here.

The input optics consist of a beam reducing telescope and a cylindrical lens as shown in Fig. 6 The telescope collimates the light in the horizontal plane while the cylindrical lens focusses the light in the vertical plane to a horizontal line focus lying along the z-axis in the interaction volume. The output cylindrical optics focus in the horizontal plane and image in the vertical

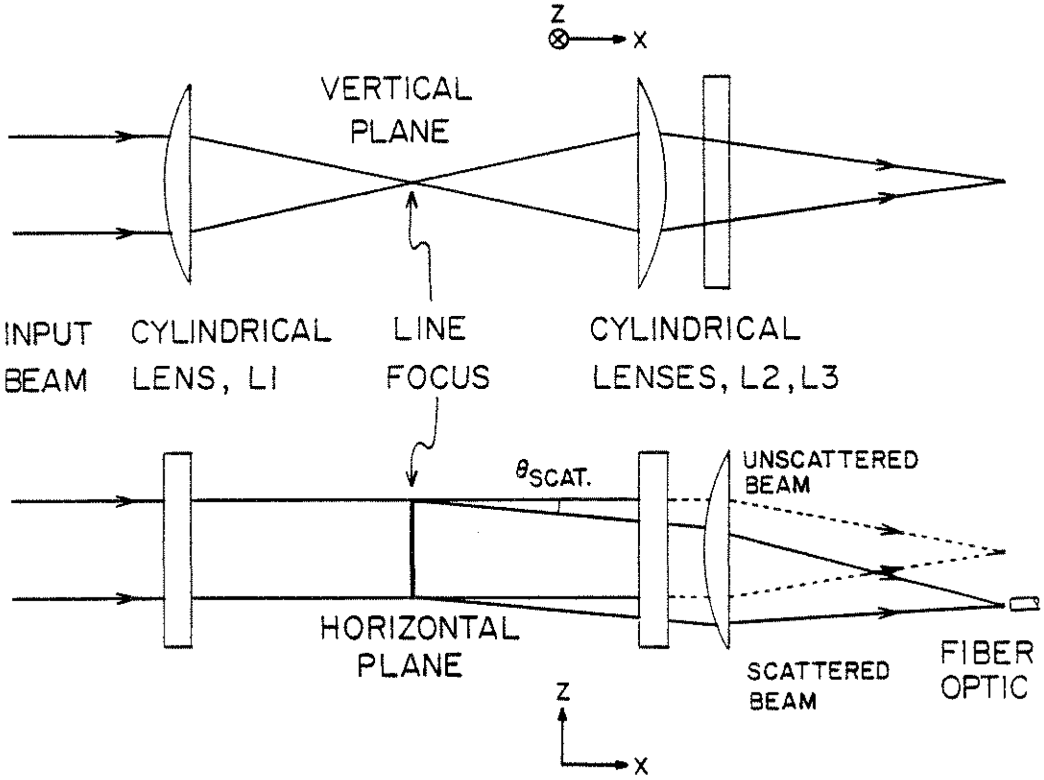

Fig. 6: Optical system used for small angle, collective ruby laser Thomson scattering. The input optics focus the collimated ruby laser beam to a line focus. The output optics separate the scattered and unscattered beams.

plane bringing the line focus to a spot focus at the fiber optic. Because the scattered and unscattered beams are diverging at a small scatter angle $\delta\theta$, the separation of the foci (of the scattered and unscattered beams) in the detection plane is $f\delta\theta$ where f is the focal length of the horizontal output focussing lens. Because the scattered and unscattered beams are separated in space they can be detected independently without the unscattered light overwhelming the detector. In practice an appreciable amount of stray light (due to specular reflections from the various optical components in the system) is in fact observed. Ultimately a satisfactory discrimination ratio of $\cong 10^{-11}$ is achieved through the use of interference filters which selectively attenuate the frequency unshifted ruby laser light (stray).

For either small or large angle Thomson scattering the scattered light is focused onto a polished fiber optic and routed to the input slit of a spectrometer. Two types of spectrometers have been used: A 2 m, high resolution spectrograph for resolving the frequency shift of SBS generated ion wave Thomson scatter and a low dispersion, 1/4 m spectrograph for detection of multiples of ω_p shifts arising from scattering from plasma wave modes and harmonics. The spectrometers image the input slit in the output plane with the appropriate chromatic dispersion.

At the spectrograph output plane the spectra are recorded by either a 500 ch optical multichannel analyzer (OMA) or streak camera. With the OMA the resolution attainable is typically $\cong 2$ Å with the low resolution spectrograph and ≅ 0.3 Å for the high resolution spectrograph. The streak camera gives slightly lower resolution with either spectrograph and has been used with temporal resolutions as high as 1 ns/cm for a 1 cm streak on the recording film.

In practice the angle of incidence with respect to $\hat{z}$ of the ruby laser probe beam is chosen such that ω and k matching between the incident and scattered probe beams and the electrostatic plasma mode of interest is achieved. The input and output optics are aligned to this angle for a given experimental run and data are recorded as Thomson scattered ruby laser light frequency spectra for a given scatter angle. These spectra are then interpreted as the electrostatic mode frequency spectrum for modes with $k = k(\theta)$. That is for a given geometry, we record $P_{scat}(\omega,k(\theta))$. Discreteness in k for certain modes has been verified. This will be discussed in greater detail when experimental results are presented.

PLASMA PREIONIZATION

As mentioned above the CO_2 laser excites the plasma beat wave in a preformed target plasma. This plasma is formed by discharging a capacitor across the gap between two electrodes which are fixed within the vacuum vessel. The plasma is taken to full ionization upon arrival of the CO_2 laser pulse. Preforming the plasma yields more uniform and reproducible plasmas and expends less laser energy for full ionization than a neutral gas target. The arc discharge is typically created in 2 torr hydrogen-air gas mixture. Two types of electrodes have been successfully used; a rail-gap electrode 3 mm × 20 mm and a ball and point electrode. The rail-gap configuration appeared to give a more uniform plasma along $\hat{z}$ but the ball and point electrode was used for most of the experiments because it yielded a plasma which was more reliably positioned along the z-axis. Both types of electrodes suffer from severe surface erosion of the cathode due to bombardment by energetic ions. This problem was controlled to some extent by critically damping the L-C circuit formed by the charged capacitor and lead inductance. This, however, typically yielded lower density plasmas and often lead to plasma conditions which were, for undetermined reasons, less favorable for the excitation of the beat wave and other modes.

It was found that the most controlled method of varying the plasma density (inferred from the frequency shift of the SRS backscatter) was to vary the relative timing of the initiation of the arc discharge and arrival of the CO_2 laser pulse. We hypothesize that this was due to thermal expansion of the neutral gas in the partially preionized discharge. By adjusting the arc timing so that the CO_2 laser arrives later in the discharge after appreciable neutral gas expansion has occured, fewer neutrals are available for ionization by the laser and the resulting plasma density is lower. Similarly early arrival of the CO_2 laser pulse as a rule yielded higher plasma densities. The required timing variation of the arc trigger was typically 1 - 3 μs with respect to the CO_2 laser trigger. Plasma parameters will be discussed in more detail when we present results of SBS and SRS diagnostic measurements.

CHAPTER IV: EXPERIMENTAL RESULTS

In carrying out our studies of beat excited electron plasma waves several classes of experiments have been performed. We begin with a review of the experiments performed.

In that beat wave excitation is a resonant process, the success of which depends on ones ability to create a resonant density plasma of sufficient length ($\cong 10\lambda_{es}$), our initial experiments focused primarily on the characterization of the plasma. A most important diagnostic of plasma conditions (density and scale length) was provided by collective Thomson scattering from plasma waves produced by stimulated Raman backscatter.

Having established and adjusted plasma conditions, beat excitation was achieved. Thomson scattering from the beat-excited plasma waves was again critical in verifying resonance, interaction length and spectral content. The forward scattered light was analyzed as an independent check to verify the excitation of the high phase velocity beat wave.

Further study of the Thomson scatter spectra at various scattering angles lead to the discovery of mode coupling in beat wave experiments. As will be discussed, many mode coupling mechanisms are possible in an underdense plasma because of the similarity of the wavenumbers of SBS driven ion waves and SRS driven plasma waves.

CHARACTERIZATION OF THE PLASMA

The arc plasma production technique, although used quite successfully in SBS experiments, was the subject of initial testing. Of particular concern was whether or not a plasma of sufficient density (10^{17} cm^{-3}) and length ($10\lambda \cong 1$ mm) could be produced.

To answer this question a single pulse of a single frequency CO_2 laser beam was focused onto the preformed arc plasma created in a variety of neutral gases. The backscattered laser light was split into two beams. One was detected directly and used to monitor SBS backscatter. The other was passed through a gas cell (SF_6, 10.6 μm absorbing) and a series of interference filters. These filters were low (frequency) pass filters which passed light above 11.1 and 11.75 μm. Selectively attenuating the 10.6 μm (SBS) component provided sufficient signal to noise ratio for detection of the frequency downshifted (wavelength upshifted) SRS backscatter. Since the frequency shift of the SRS backscatter equals the plasma wave frequency ($\cong \omega_p$) at the scatter layer, these two filters cut off at frequencies corresponding to plasma densities of 3×10^{16} and 1.2×10^{17} cm^{-3} respectively.

Substitution of filters while observing the SRS backscatter allowed us to roughly estimate the plasma density while varying arc parameters since no low density SRS backscatter could pass through the 11.75 μm filter. A 10.6 μm band pass filter (10.6 ± 0.2 μm) was substituted for the low pass filters. The absence of a signal when the band pass filter was in place verified that the signals were indeed frequency shifted and not due to stray light.

SRS measurements were carried out using several neutral gases and mixes. The gas mix which produced the most reproducible Raman backscatter consisted of 1 torr each of hydrogen and air, although on various occasions, significant variations of this mix were successfully used (e.g. 1 torr H_2, 0.1 torr air). The plasma density, inferred from the frequency shift of the backscatter, could be roughly tuned to resonance by adjusting such parameters as arc voltage, arc timing, neutral gas pressure, and laser energy.

Of particular interest early in our experiments was the shot to shot reproducibility of plasma density for a given set of arc parameters. Fig. 7a shows a histogram of the number of occurences versus SRS frequency shift of the Thomson scatter spectrum measured in OMA channels where 10 OMA channels corresponds to a shift of about 0.028 ω_{po}. In Fig. 7a one can see some variations of the SRS frequency shift from shot to shot. These variations were sensitive

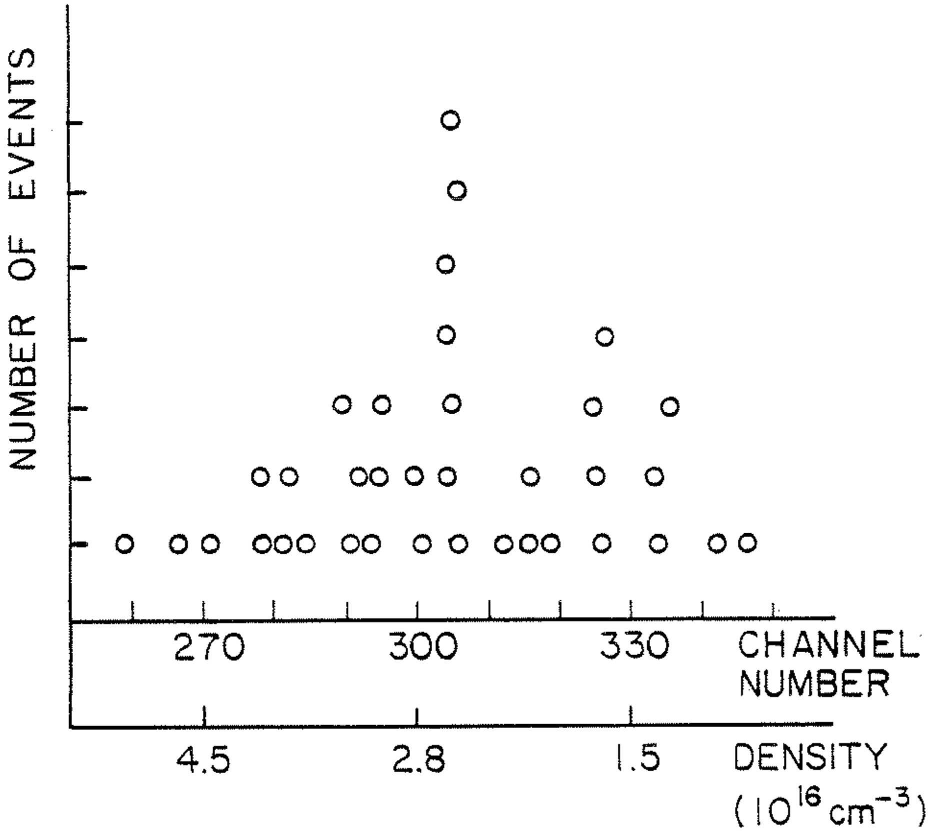

Fig. 7a: Histogram of number of occurences of a given frequency shift versus frequency shift. The shifts are measured in OMA channels and are also indexed as plasma density.

to laser energy and the condition of the arc electrodes. Typically we observed larger variations early in a given experimental run when the electrodes, polished prior to each run, underwent a period of "burn-in". This burn-in period typically required about 30 - 40 shots. The irreproducibility also became more pronounced after several hours of continuous operation due to electrode degradation caused by ion bombardment of the cathode.

Under stable arc and CO_2 laser conditions it was possible to tune the plasma density by adjusting the arc timing and voltage. Fig. 7b shows Thomson scatter spectra obtained from scattering from SRS driven electron plasma waves at three different densities. With the gas mix with which we typically operated (1 torr H_2, 1 torr Air) densities of $2 \times 10^{16} - 2 \times 10^{17}$ cm^{-3} were attainable.

A crude estimate of plasma uniformity was obtained from the gradient threshold for the SRS instability. Since SRS is observed, the gradient threshold is assumed to have been exceeded and the plasma length is inferred to be greater than or equal to the scale length appearing in the gradient threshold formula[19] $(v_{osc}/c)^2 = 2(k_{laser}L_n)^{-1}$. Using our laser intensity of 10^{13} W/cm², we estimate $L_{plasma} > 8$ mm.

A second method of estimating the plasma uniformity is to vary the position of the CO_2 laser focal spot with respect to the

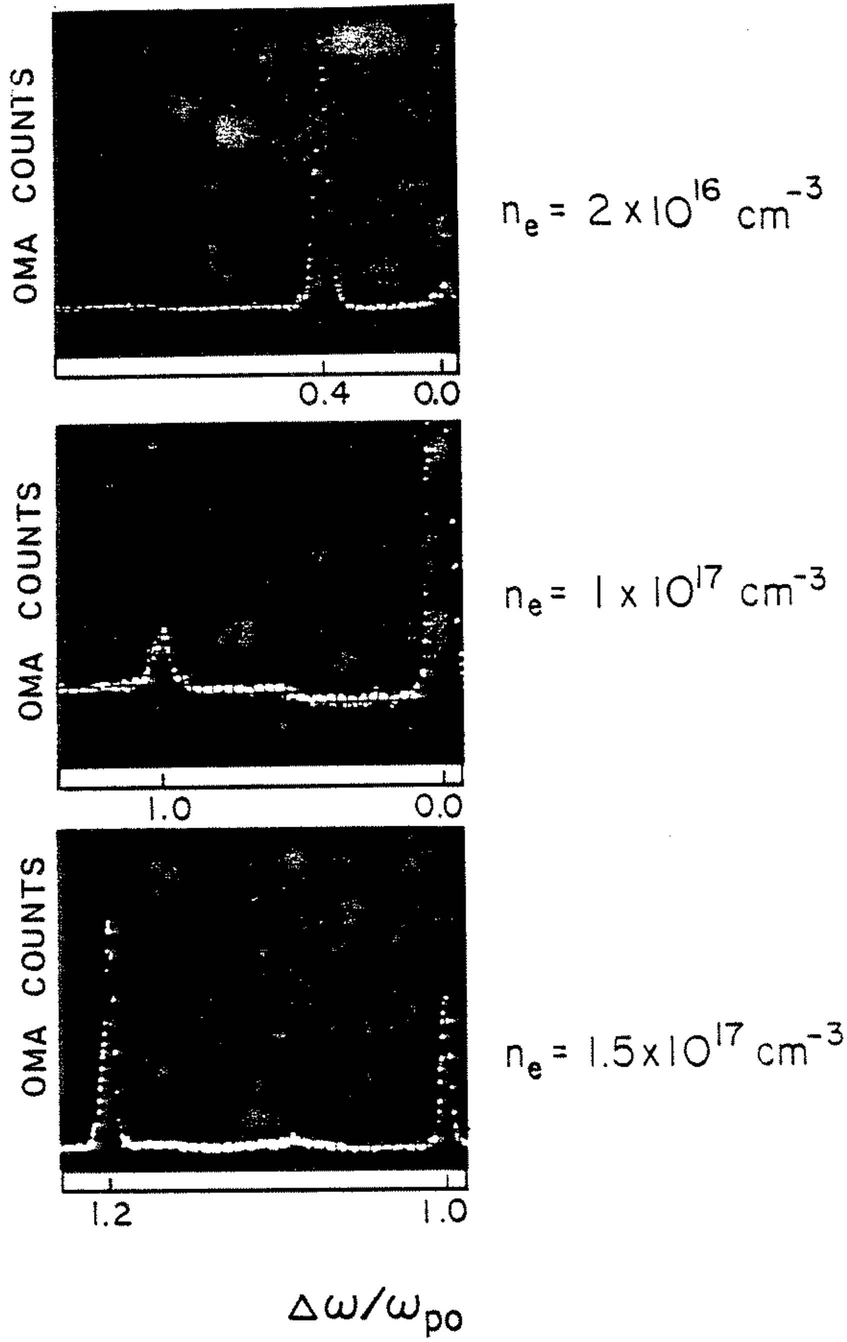

Fig. 7b: Thomson scatter frequency spectra of SRS produced plasma waves. The three different ω_p shifts shown in these examples correspond to three different plasma densities.

preionizing electrodes while recording the corresponding variation in the level of SRS backscatter. This technique, in effect, measures the strength of the SRS response as a function of axial position within the plasma. The strength of the response is assumed to be largest in regions where the plasma is uniform and small where the plasma contains stronger density gradients. To accomplish this measurement the CO_2 laser focusing lens was scanned axially with respect to the fixed axial position of the preionizing electrodes. For each lens position the average SRS signal was monitored on the backscatter detector and recorded. Fig. 8 shows the results of this measurement which show the SRS to be detectable over an axial range of about 4 mm. It should be kept in mind that although the electrode served to preionize the plasma, the CO_2 laser beam was ultimately responsible for bringing the plasma to a fully ionized state. Thus this measured axial profile of the SRS demonstrates the importance of preionization for plasma uniformity.

EXCITATION OF THE BEAT WAVE

The ability to control the plasma conditions, as demonstrated by the SRS measurements, provided us with a well controlled environment in which to conduct a study of plasma beat wave excitation.

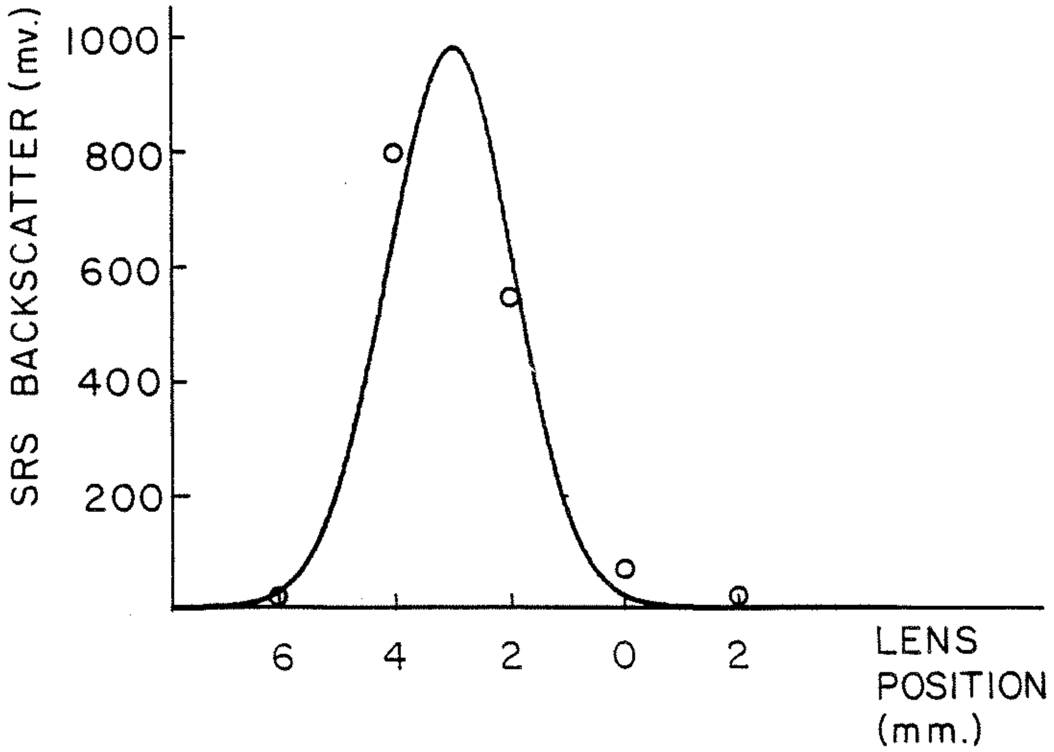

Fig. 8: Axial profile of SRS backscatter intensity measured by varying the position of the CO_2 laser focusing lens with respect to the prionizing electrodes. The solid curve shown is intended to serve as a visual reference only.

The most direct evidence for existence of the plasma beat wave was obtained from small angle Thomson scatter spectra. In these experiments the diagnostic ruby laser optical system, as described previously, was aligned for a scatter angle of 0.4° (ω and k matching to the $\lambda \cong 100$ μm beatwave). The CO_2 pump laser was initially operated on a single laser line (10.59 μm). Arc parameters were varied until the SRS backscatter frequency shift measurements indicated that a resonant plasma density had been attained. The CO_2 laser was then operated on two frequencies (10.59 + 9.56 μm) by introducing absorbing gases into the CO_2 laser cavity gas cell.

Fig. 9 shows a Thomson scatter frequency spectrum taken at 0.4°. As expected the frequency shift of the beatwave spectral peak (left) corresponds exactly to the frequency separation of the two laser lines. The peak on the right, unlike the SBS spectral peak appearing in the $2k_{CO_2}$ ($7\frac{1}{2}^{\circ}$) Thomson scatter spectra of Fig. 7b, is due to stray ruby laser light (i.e. the $2k_{CO_2}$ SBS waves are not ω and k matched to the ruby laser at 0.4°).

Further evidence for the existence of the plasma beat wave was obtained by analyzing the transmitted (forward scattered) CO_2 laser light. Fig. 10a schematically shows the transmitted CO_2 laser light spectrum. In addition to the two CO_2 laser lines at 10.6 and 9.6 μm two discrete lines frequency downshifted from the 10.6 μm laser

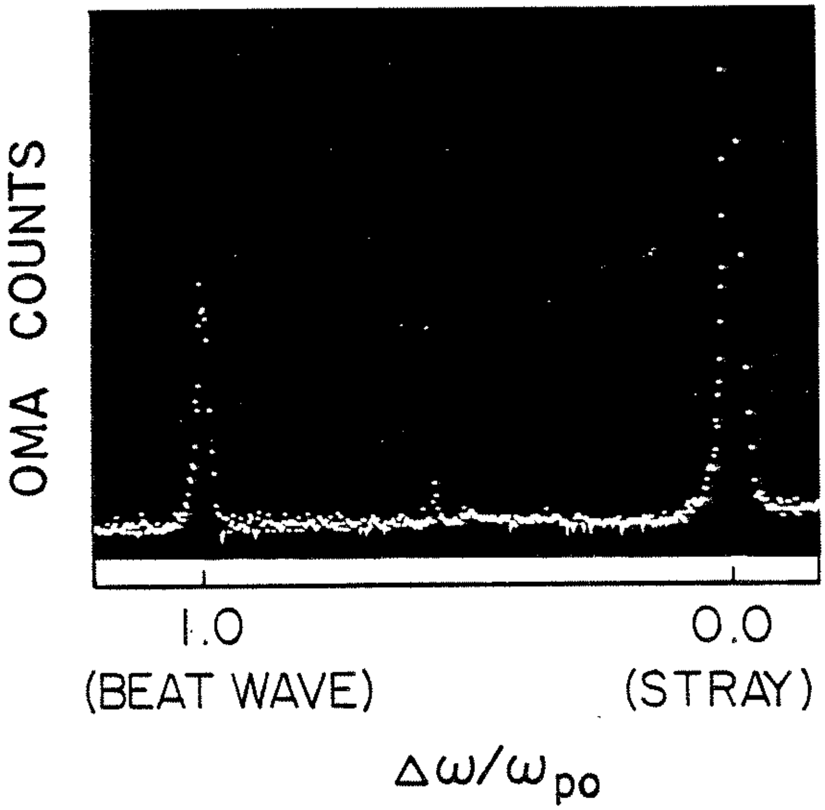

Fig. 9: Thomson scatter frequency spectrum of the high phase velocity, beat-excited plasma wave (Beat Wave).

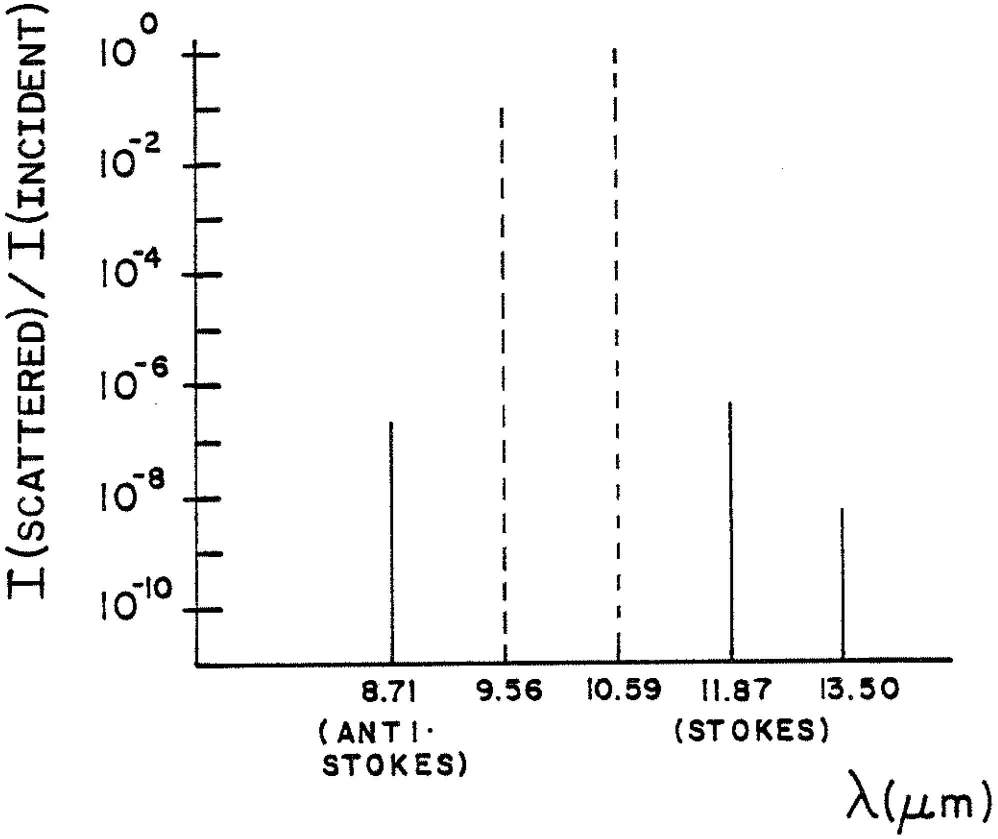

Fig. 10a: Schematic representation of the measured forward scattered (transmitted) CO_2 laser light frequency spectrum. The dashed oines correspond to the two (10.6 and 9.6 μm) incident CO_2 laser lines.

line by ω_{po} and one line frequency upshifted from the 9.6 µm laser line by ω_{po} were detected. These "Stokes" (frequency downshifted) and "anti-Stokes"[20,21,22] (frequency upshifted lines are attributed to scattering of the CO_2 laser light by the plasma beat wave. Note also that, in principle, contributions to the first Stokes line and the first anti-Stokes line can arise from scattering of the 9.6 and 10.6 µm lines from the second harmonic of the beat wave. Similarly the second Stokes and second anti-Stokes can scatter off of the beat wave fundamental and make contributions to the first Stokes and first anti-Stokes lines.

This situation is further complicated by the fact that the forward scatter measurements integrate along the entire axial extent of the interaction region where, as one might expect, the spectral character of the cascaded electromagnetic spectrum varies along the direction of propagation of the plasma wave. It is therefore possible to draw limited conclusions from the relative amplitudes of the various spectral features in Fig. 10a. However the structure of the electromagnetic spectrum (spectral peaks spaced with $\Delta\omega = \omega_{po}$) is unambiguous evidence for the existence of the high phase velocity beat wave since only the short- k beat wave can ω and k match to the CO_2 laser lines to produce the observed electromagnetic spectrum. As expected when the CO_2 laser was operated on a single laser line, no Stokes of anti-Stokes lines were observed. Also when the laser was operated on two frequencies but with vacuum in place of the plasma (null test), no Stokes or anti-Stokes sidebands were observed.

Discreteness of the first Stokes and anti-Stokes lines was verified by scanning the grating used to analyze the forward scattered CO_2 laser light as shown in Figs. 10b,c. The fine structure of the Stokes line is believed to be due to the frequency content of the CO_2 lasing line. Occasionally the laser operates on two vibrational-rotational transitions in the 10.6 μm band (separated by approximately 200 GHz) in addition to operating on the 9.56 μm line.

Important to the coherence of the plasma beat wave is the discreteness in ω and k of that mode. Discreteness in ω has already been demonstrated in the Thomson scatter spectrum of Fig. 9. A detailed plasma beat wave k-spectrum, shown in Fig. 11, was taken by scanning the fiber optic in the ruby laser Thomson scatter detection plane. This spectrum was taken over many shots and statistically found to peak at the expected $k_p = k_{10.6} - k_{9.6}$ with a half-power width of about 20 % (of k_p). Note also that the discreteness in k of the transmitted CO_2 laser light (c.f. Figs. 10b,c) supports the conclusion that the plasma beat wave is discrete. As mentioned above, when the fiber was scanned to a position corresponding to the angle for scattering from the plasma beat wave second harmonic, no signal was observed indicating that

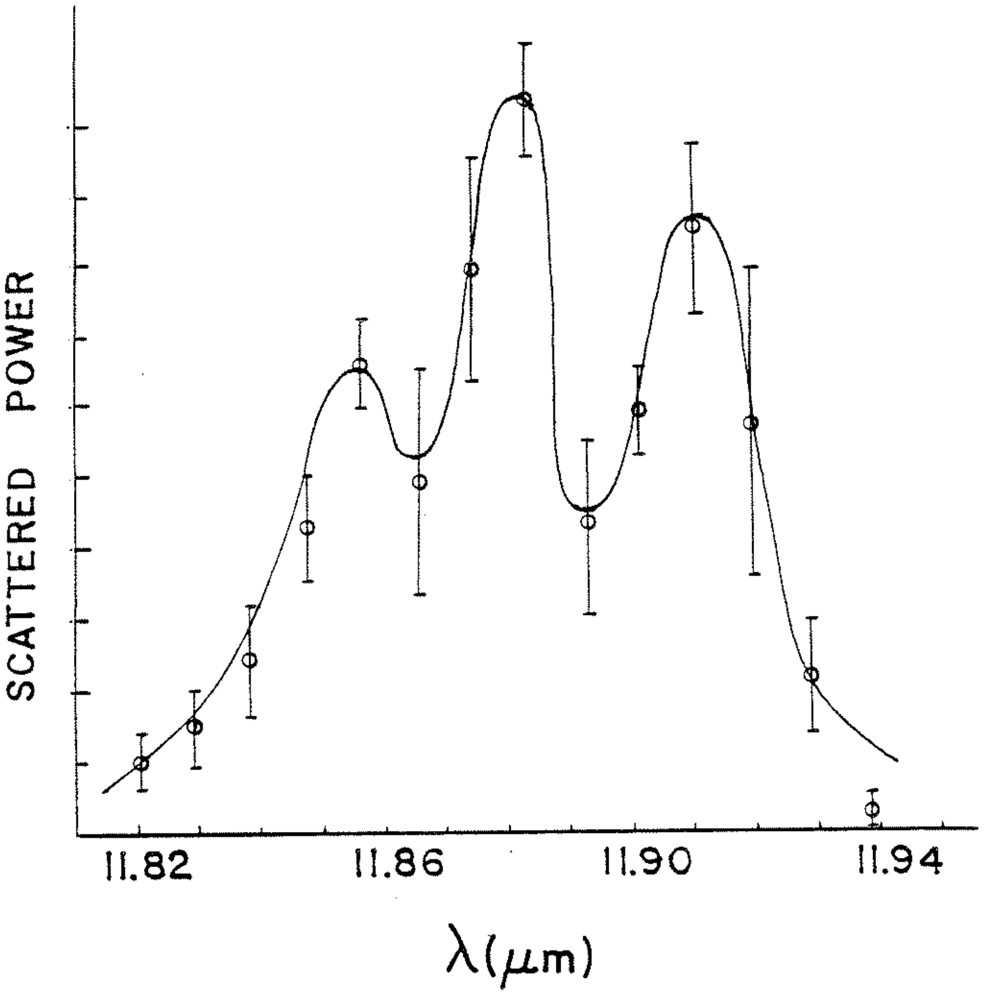

Fig. 10b: Detailed spectrum of forward scattered, frequency upshifted (Stokes) CO_2 laser light. The solid curve is is intended to serve as a visual reference only.

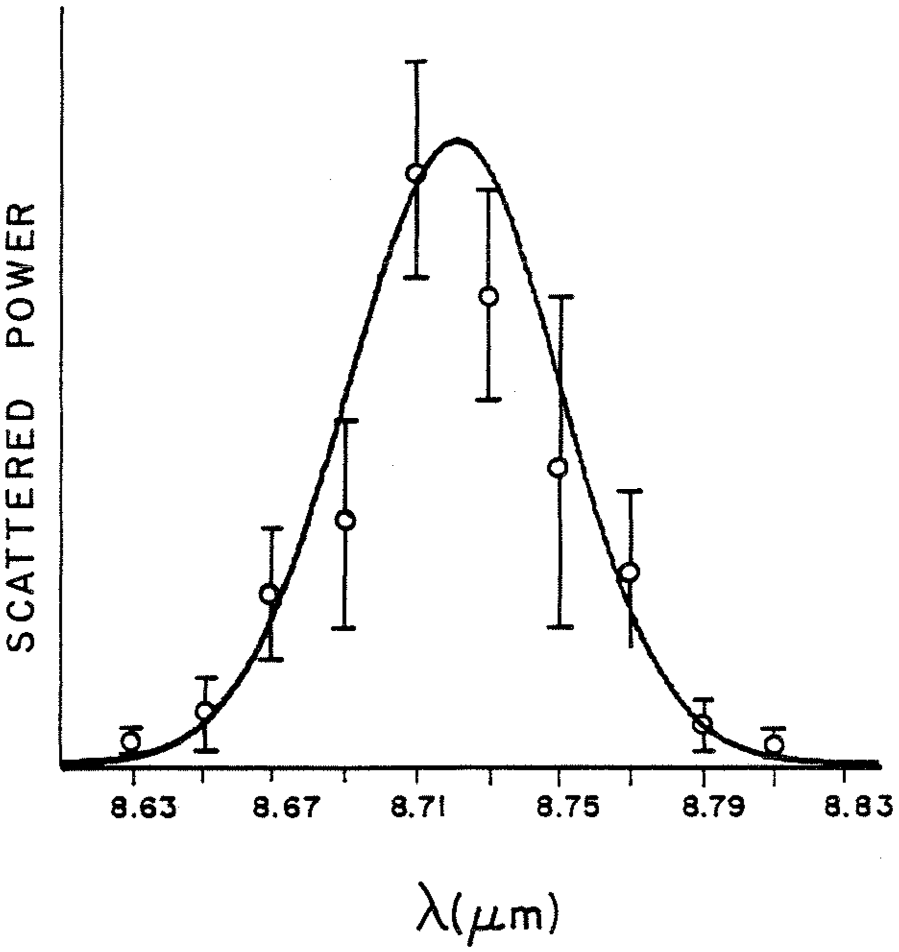

Fig. 10c: Detailed spectrum of forward scattered, frequency upshifted (Anti-Stokes) CO_2 laser light. The solid curve is intended to serve as a visual reference only.

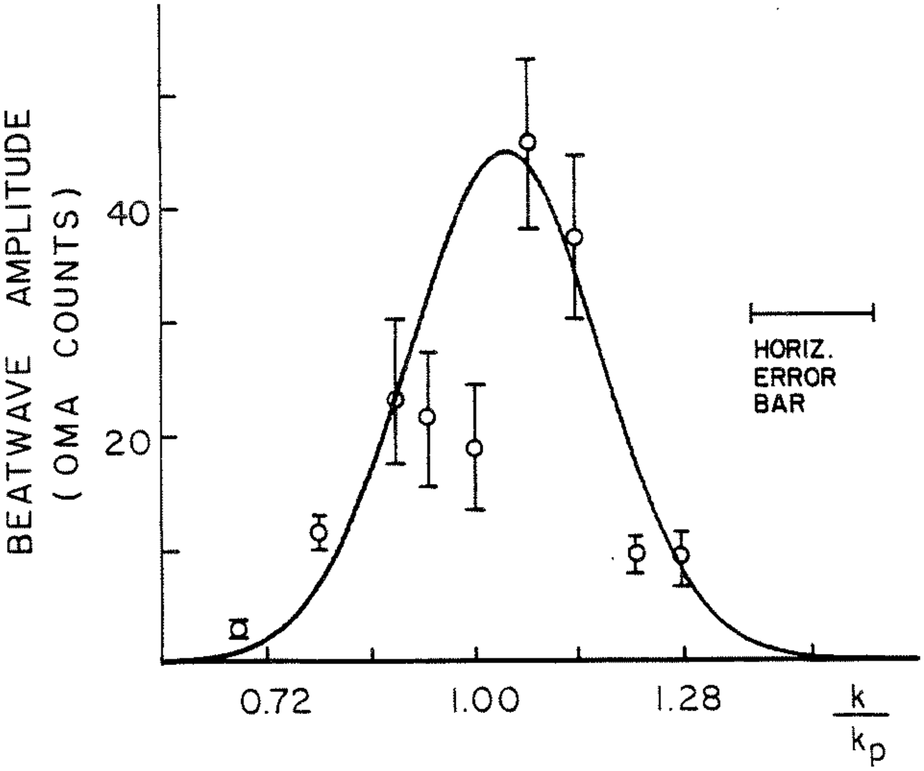

Fig. 11: Wavenumber spectrum of the high phase velocity, beat-excited plasma wave obtained by scanning the Thomson scatter detection fiber optic in the z-direction. The horizontal error bar shown is due to the positioning error and finite size of the light collecting fiber optic. The solid curve is intended to serve as a visual reference only.

the beat wave second harmonic was down in amplitude by a factor of 10 or greater.

Methods to estimate the plasma interaction length have been presented above for the non-resonant (single frequency) excitation. The cylindrical Thomson scatter optical system afforded us the opportunity to directly measure the resonant interaction length of the beat wave. Fig. 12 illustrates the technique used to make this measurement. The ruby laser input beam was masked by a vertical slit 460 μm in width. As a result the ruby laser beam was brought to approximately a line focus of length 460 μm along the z-axis. By positioning the slit (horizontally along $\hat{z}$) to intercept different parts of the input beam we selectively probed different axial regions of the beat wave volume. The scattered probe beam intensity was recorded for various slit positions for many shots of the laser system and provided a statistical picture of the beat wave amplitude as a function of axial position (z). Note that resolution problems which can arise (poor focus quality in the detection plane) when illuminating a finite number of plasma wavelengths ($n \cong 5$) with the probe beam have been shown to be of no concern here because the spot size at the fiber optic detection plane was nearly equal to the fiber optic area[17]. Most of the scattered light (≅ 80 %) was collected and served as a reliable diagnostic of the beat wave amplitude at the selected region of the beat wave volume.

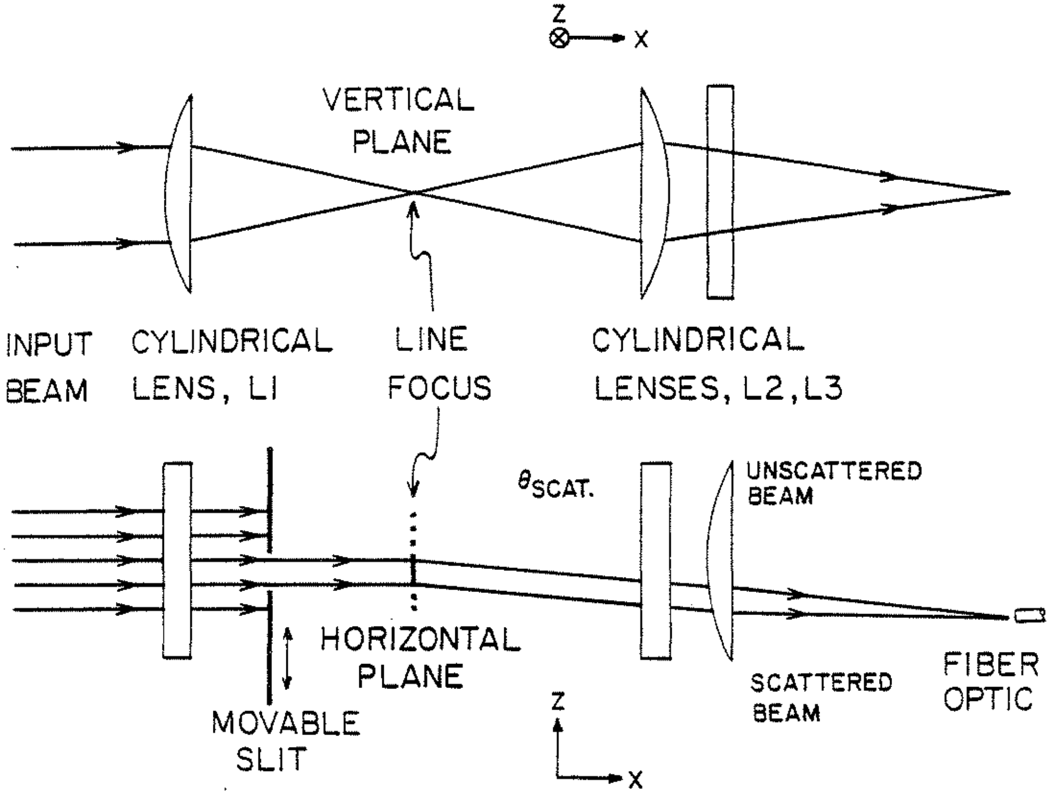

Fig. 12: Illustration of the technique used to determine the axial extent of the beat wave. By scanning the movable slit (along z), different axial regions of the beat wave scatter volume are probed.

The results of this measurement are shown in Fig. 13. The interaction region is found to be about 2mm or 20 plasma wavelengths in length. Because the plasma wave group velocity to phase velocity ratio is so small ($v_g/v_\phi \cong v_e^2/c^2$), one can expect that the wave field will grow to its saturation value long before convecting out of the resonant interaction region.

This conclusion is supported by the estimated wave field amplitude as inferred from the plasma beat wave Thomson scatter measurements. The interaction length and Thomson scatter intensity can be substituted into the Bragg scattering formula[23]

$$\frac{I_{scat}}{I_{inc}} = \frac{L_p}{L_r} \frac{\tau_p}{\tau_r} \left[\frac{\pi}{2} \frac{n_1}{n_o} \frac{n_o}{n_c} \frac{d}{\lambda_r} \right]^2 \qquad (43)$$

where L_p (L_r) is the plasma wave (ruby focus) length, τ_p (τ_r) is the plasma wave (ruby laser) duration, d is the plasma wave width (perpendicular to $\vec{k}_{es}$), λ_r is the ruby laser wavelength, $\tilde{n}$, n_o, and n_c are the perturbation, background plasma, and CO_2 laser critical densities respectively. Based on a maximum measured I_{scat}/I_{inc} of $\cong 10^{-10}$ for the ruby probe beam at 0.4°, Eq. 43 yields a plasma beat wave field amplitude of $\cong$ 1 - 3 %. In arriving at this figure we have included the statistical variation of the scattered probe beam. However an important subtlety in this

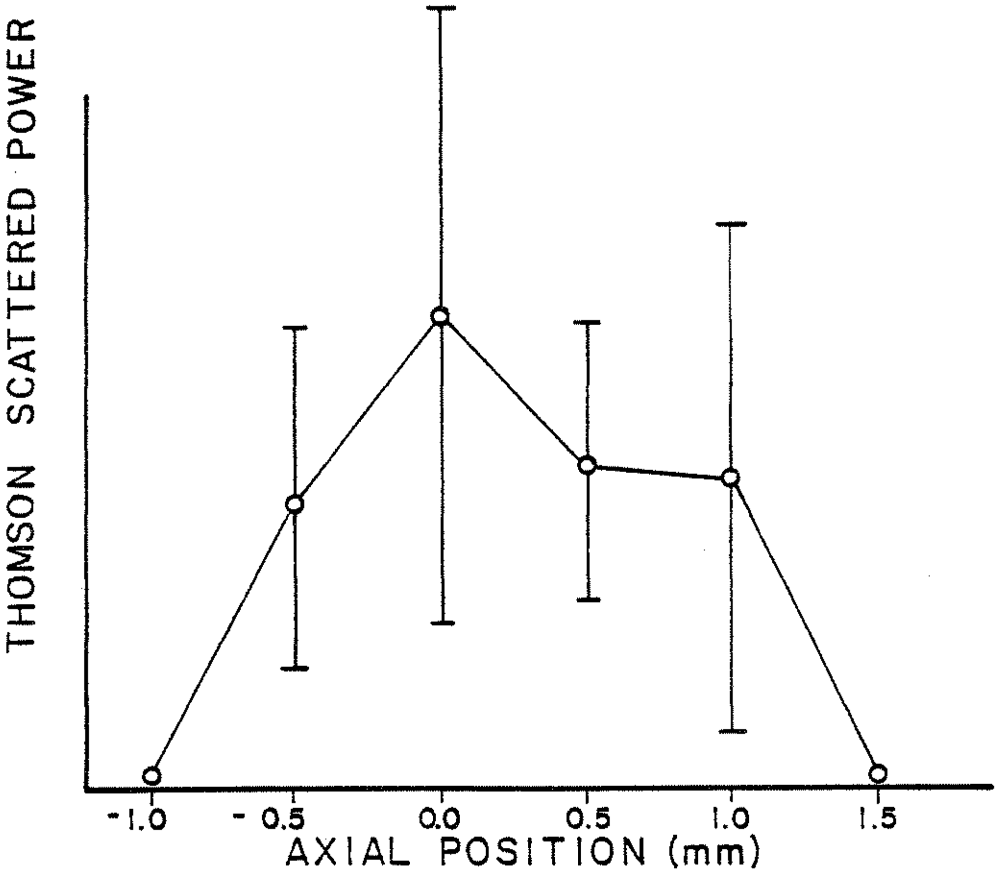

Fig. 13: Axial profile of the beat wave inferred from Thomson scatter measurements (c.f. Fig. 8).

beat wave Thomson scatter measurement was pointed out by Martin et al.[24,25] Assume, as in Fig. 14a, that at the CO_2 laser focus the two pump components are coaxial and drive an axially propagating beat wave with $\vec{k}_p = k_p\hat{z}$ where as before $k_p = k_{9.6} - k_{10.6}$. Although ω and k matching between the beat wave and the CO_2 laser pumps is satisfied, it is not possible to ω and k match to a Thomson scatter probe beam which is nearly normally incident as in the experiment. To see this note that because the Thomson scatter probe beam is shifted in frequency by ω_p, its wave vector necessarily changes in length by c/ω_p. Thus for perfect collinear optical mixing ($\vec{k}_{9.6}$, $\vec{k}_{10.6}$, and $\vec{k}_p$ all exactly along $\hat{z}$) ω and k matching with the Thomson scatter probe beam can only be achieved if it too is incident along $\hat{z}$ as in Fig. 14b. The resolution of this dilema lies in the realization that both CO_2 laser lines have a finite $k_\perp$ spectrum. Fig. 14c illustrates how ω and k matching between one such beat wave component and both the CO_2 laser and the Thomson scatter probe beams can occur. Two components of the CO_2 laser beam (one for each frequency) separated in angle by about 6^o optically mix to drive a beat wave which propagates at about 45^o with respect to the z axis. It is now possible for the Thomson scatter probe beam, incident nearly normal to $\hat{z}$, to ω and k match to the beat wave with a scatter angle very near the naively estimated scatter angle of 0.4^o.

From the above discussion it is clear that our Thomson scatter

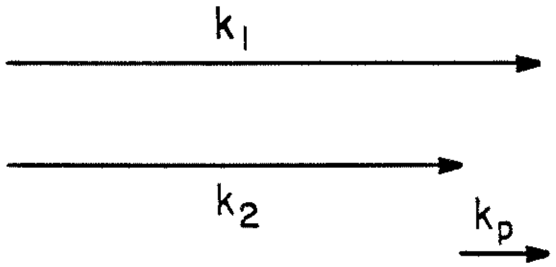

CO$_2$ Laser #1: $k_1 = \omega_1/c = 2\pi/10.59\ \mu m$

CO$_2$ Laser #2: $k_2 = \omega_2/c = 2\pi/9.56\ \mu m$

Plasma Wave: $k_p = k_2 - k_1$, $\omega_{po} = \omega_2 - \omega_1$

Fig. 14a: Diagram of ω and k matching of two collinear, axially propagating CO$_2$ laser lines.

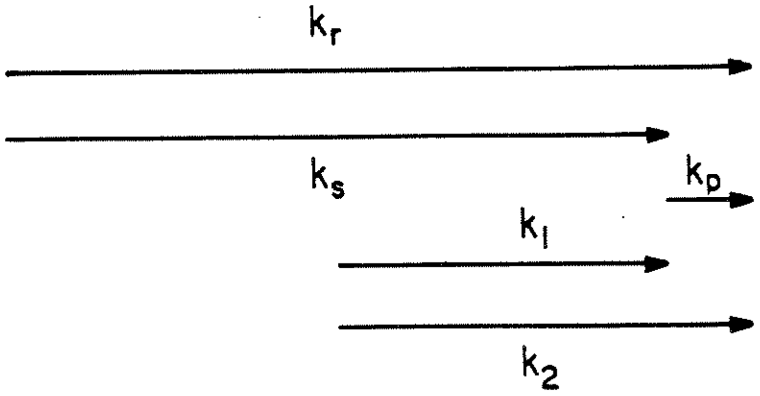

CO$_2$ Laser #1: $k_1 = \omega_1/c = 2\pi/10.59\,\mu m$

CO$_2$ Laser #2: $k_2 = \omega_2/c = 2\pi/9.56\,\mu m$

Plasma Wave: $k_p = k_2 - k_1$, $\omega_{po} = \omega_2 - \omega_1$

Ruby Laser (inc.): $k_r = \omega_r/c = 2\pi/.6943\,\mu m$

Ruby Laser (scat.): $k_s = (\omega_r + \omega_{po})/c$

Fig. 14b: Diagram of ω and k-matching of the beat-excited plasma wave and the incident and scattered diagnostic Ruby laser beams. Case shown is for perfect k-matching of the diagnostic probe beam with the axial beat wave.

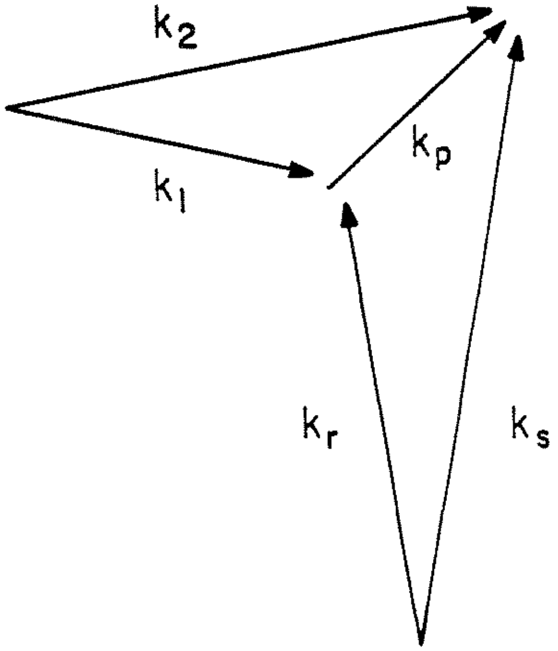

CO_2 Laser #1: $k_1 = \omega_1 / c = 2\pi / 10.59\ \mu m$

CO_2 Laser #2: $k_2 = \omega_2 / c = 2\pi / 9.56\ \mu m$

Plasma Wave: $k_p = k_2 - k_1$, $\omega_{po} = \omega_2 - \omega_1$

Ruby Laser (inc.): $k_r = \omega_r / c = 2\pi / .6943\ \mu m$

Ruby Laser (scat.): $k_s = (\omega_r + \omega_{po}) / c$

Fig. 14c: Diagram of ω and k-matching of the beat-excited plasma wave and the incident and scattered diagnostic Ruby laser beams. Case shown is for a nearly normally incident Ruby laser beam where the probe beam matches to a component of the beat wave which propagates at about a 45° angle with respect to the z-axis.

measurements detected the component of the beat propagating at about 45^o with respect to the z axis. However of greater interest for the PBWA is the electric field of the axially propagating component. To estimate this using our measured fields of the obliquely propagating component consider the bi-gaussian beat wave k-spectrum arising when the two gaussian CO_2 laser beams beat in space as shown in Fig. 15. The width in $k_\perp$ of the distribution can be estimated as $\Delta k_\perp = 2\Pi/D_{bw}$, where D_{bw} is the beat wave transverse dimension. Thus the measured amplitude of the obliquely propagating component is smaller than the axial component by a factor of approximately $\exp\left[-(D_{bw}/100\mu m)^2\right]$. In light of these considerations one is lead to estimate the field of the axial component of the beat wave to be a few times larger than the 1 to 3 % measured for the oblique component. A detailed discussion of the plasma beat wave field saturation amplitude will be given in a later section. However is it worth noting at this point that the measured field amplitude is consistent with the theoretical predictions of Ch. II.

OBSERVATIONS OF COUPLED MODES

To further characterize the electrostatic ω-k spectrum, Thomson scatter measurements were made at several scatter angles other than 0.4^o. These angles, $7\frac{1}{2}^o$, 15^o, and $22\frac{1}{2}^o$, were chosen so as to achieve ω and k matching between the ruby laser probe beam and the

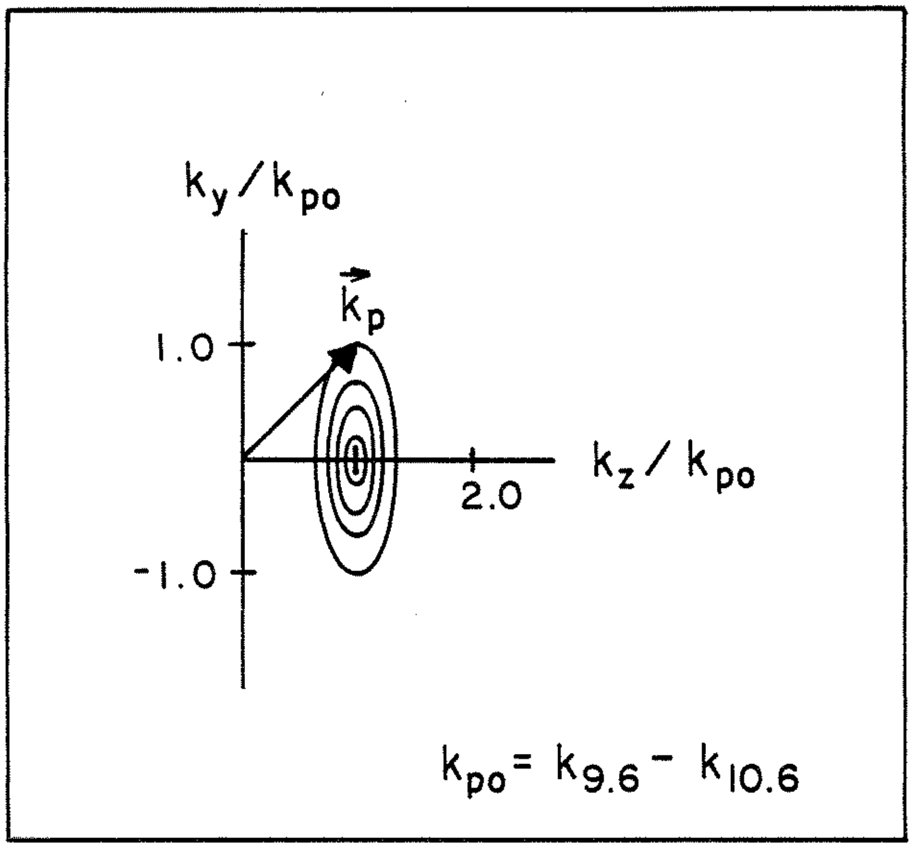

Fig. 15: k_x - k_y spectrum of the CO_2 laser beam at the focus. The finite $k_\perp$ (k_y) component gives rise to beat wave components which propagate at oblique angles with respect to the $\hat{z}$-axis.

$2k_{CO_2}$, $4k_{CO_2}$, and $6k_{CO_2}$ electrostatic modes respectively. This allowed us to construct the electrostatic ω,k spectrum by obtaining the ω-spectrum at the electrostatic k's of interest.

The results of measurements made at $7\frac{1}{2}^{\circ}$ using a single CO_2 laser line have already been discussed in a previous section. Fig. 16 shows a composite Thomson scatter frequency spectrum taken at $7\frac{1}{2}^{\circ}$ with a two frequency CO_2 laser beam. The central spectral peak is due to scattering from $k = k_i = 2k_{CO_2}$ SBS driven ion acoustic waves, and is present even with a single frequency CO_2 laser beam. Note that the SBS spectral peak appears to occur at the ruby laser frequency because the small acoustic frequency shift ($\omega_{ac}/\omega_p \cong 3.5 \times 10^{-3}$) is not resolvable on this scale. The peak on the left is blue shifted from the SBS spectral peak by exactly the CO_2 laser line frequency difference. The spectral peak on the right is red shifted by the same amount. The blue and red shifted lines correspond to forward ($+\hat{z}$) and backward ($-\hat{z}$) propagating modes in the plasma with $k \cong k_i$ (from now on we use k_i to denote the wavenumber of electrostatic waves with $k \cong 2k_{CO_2}$). Note that for large angle Thomson scattering one does not encounter ω and k matching difficulties to the same extent as in the case of small angle scattering. Because k_{es} is large ω and k matching is easily achieved for a nearly normally incident Thomson scatter probe beam and it is the axially propagating component which is indeed probed. One is tempted to attribute the blue shifted line to a $k \cong k_i$ Raman

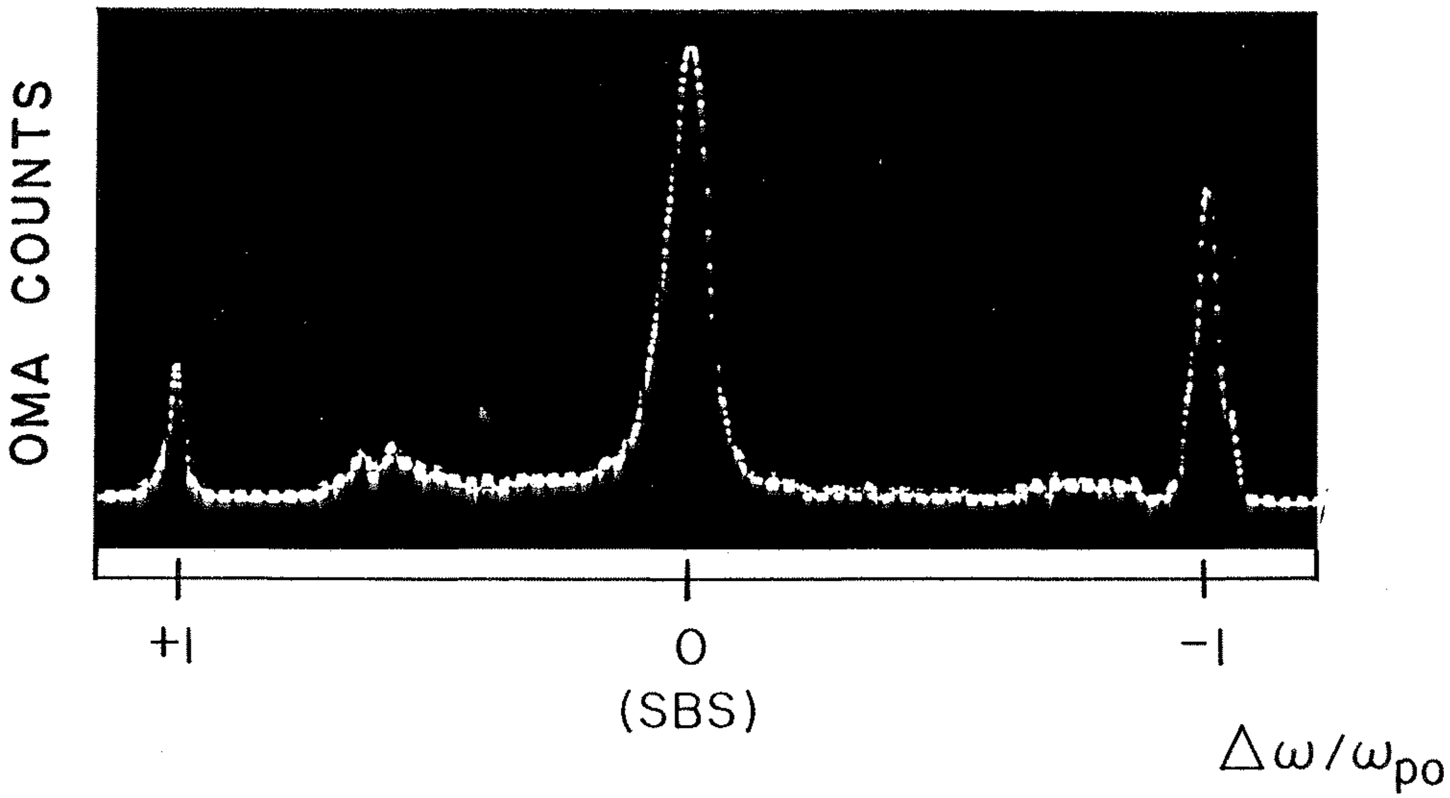

Fig. 16: Composite Thomson scatter frequency spectrum taken at a scatter angle of 7.5° showing an SBS spectral peak as well as peaks red and blue shifted by the beat frequency ω_{po}.

driven plasma wave, whereas no such explanation for the red line is readily obvious. A more plausible explanation is provided by the mode coupling model of Ch. II which predicts a symmetry in k of the resulting electrostatic (Thomson scatter) spectrum as seen in Fig. 16; that is both red and blue shifted lines are expected because modes with $\pm\vec{k}_i$ are excited when the high phase velocity plasma beat wave scatters from a density ripple with $k_{ripple} \cong k_i$. Thomson scatter measurements at $7\frac{1}{2}^{o}$ verify the presence of the ripple with $k \cong k_i$ driven by SBS from either of the two CO_2 laser lines.

Further evidence for the mode coupling process has been obtained while making Thomson scatter measurements at 15^o and $22\frac{1}{2}^{o}$, the angles corresponding to scatter from $k = 2k_i$ and $k = 3k_i$ modes respectively. Fig. 17a shows a Thomson scatter frequency spectrum taken at 15 degrees. The central peak, due to scatter from the second harmonic of SBS driven ion waves, is still unresolvable and appears unshifted on this frequency scale. The spectral peaks which are blue and red shifted by ω_{po} are due to scatter from forward $(\omega_{po},+\vec{k}_i)$ and backward $(\omega_{po},-\vec{k}_i)$ propagating coupled modes. These modes are generated when the beat wave scatters off of the density ripple: $(\omega_{po},\vec{k}_p) + (\omega_i,\vec{k}_i) \xrightarrow{m=+2} (\omega_{po},+2\vec{k}_i)$ and $(\omega_{po},\vec{k}_p) + (\omega_i,\vec{k}_i) \xrightarrow{m=-2} (\omega_{po},-2\vec{k}_i)$. The spectral peaks which are blue and red shifted by $2\omega_p$ are due to Thomson scatter from the $(2\omega_{po},\pm2\vec{k}_i)$ modes which are believed to arise when the beat wave second harmonic scatters from the ion wave ripple:

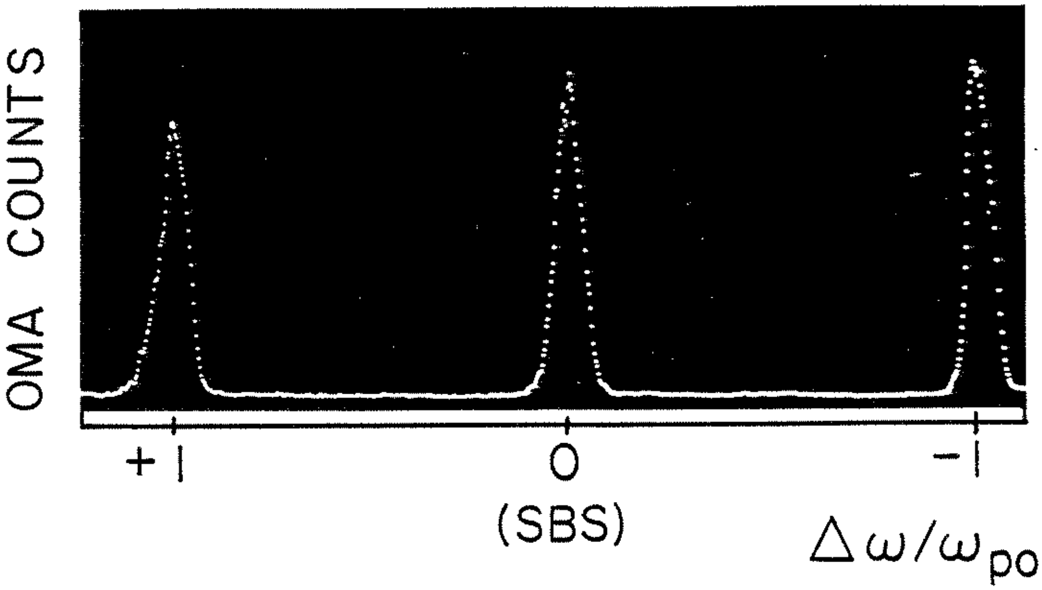

Fig. 17a: Composite Thomson scatter frequency spectrum taken at a scatter angle of 15°. The central spectral peak is due to scatter from the second harmonic of the SBS driven ion acoustic wave. The peaks red and blue shifted by ω_{po} are due to coupled modes.

$(2\omega_{po}, 2\vec{k}_p) + (\omega_i, \vec{k}_i) \xrightarrow{m=+2} (2\omega_{po}, 2\vec{k}_i)$ and $(2\omega_{po}, 2\vec{k}_p) + (\omega_i, \vec{k}_i) \xrightarrow{m=-2} (2\omega_{po}, -2\vec{k}_i)$. The experimental manifestations of the degeneracies of the $(n\omega_{po}, \pm m\vec{k}_i)$ modes mentioned in Ch. II are discussed in greater detail in a later section when other coupling mechanisms are considered.

Fig. 17b shows a $3k_i$ Thomson scatter spectrum taken on a single shot at $22\frac{1}{2}{}^{\circ}$ (a lower dispersion grating was used in the Thomson scatter spectrometer and allowed us to record up to the $\pm 3\omega_{po}$ lines simultaneously thus avoiding the need to assemble composite spectra as Fig. 7b which were composed of different portions of the Thomson scatter spectrum recorded on different shots). In Fig. 17b one again observes an unshifted spectral peak at the ruby laser frequency (center peak) due to scatter from the third ion wave harmonic. The spectral peaks which are red and blue shifted by ω_p are due to scatter from the coupled modes ($m = \pm 3$ coupling to the ion wave). Similarly the spectral peaks which are red and blue shifted by $2\omega_{po}$ are due to scatter from coupled modes arising when the second beat wave harmonic undergoes an $m = \pm 3$ coupling to the density ripple. Thus far no $3\omega_{po}, \pm 3\vec{k}_i$ modes have been observed. This is believed to be due to the relative weakness of the beat wave third harmonic.

The $\omega_{po}, \pm 2k_i$ and $\omega_{po}, \pm 3k_i$ modes described above are adequately explained by the mode coupling model of Ch. II. However the

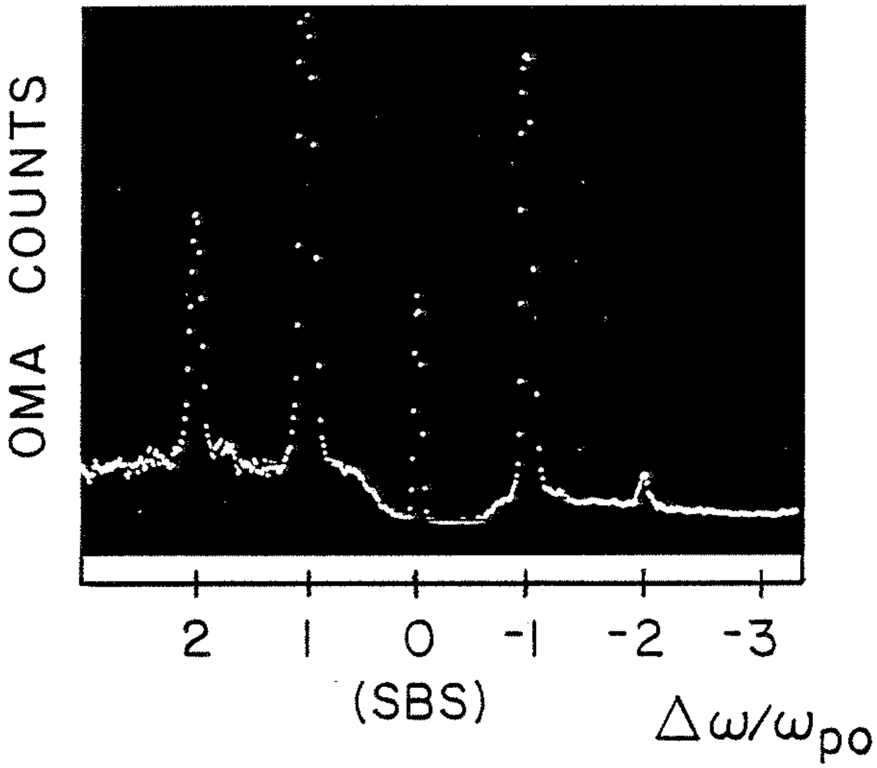

Fig. 17b: Thomson scatter frequency spectrum taken at a scatter angle of 22.5° for a single shot of the laser system. The central peak is due to scatter from the third harmonic of the SBS driven ion acoustic wave. The modes which are red and blue shifted by ω_{po} and $2\omega_{po}$ are attributed to coupled modes.

$2\omega_{po},\pm 3k_i$ lines do not fit neatly into this formalism without the introduction of beat wave harmonics. Although no second beat wave harmonic was directly observed, given the sensitivity of the 0.4^o Thomson scatter system and the characteristics of the forward electromagnetic scatter spectrum, the possibility of the existence of a beat wave second harmonic remains and these lines are attributed to $m = \pm 2$ and $m = \pm 3$ couplings of the beat wave harmonic through the SBS ion wave $\omega_i \cong 0$, k_i. Note also that the $\omega_{po},\pm 2k_i$ and $2\omega_{po},\pm 3k_i$ lines could also arise from an $m = 1$ coupling of the beat wave through the second and third ion wave harmonics $2\omega_i,2k_i$ and $3\omega_i,3k_i$. Fig. 18 summarizes the modes which have thus far been observed at the various Thomson scatter angles. Other possible excitation mechanisms for modes observed at k_i, $2k_i$, and $3k_i$ will be discussed in a later section.

An important criterion for the existence of coupled modes is the simultaneity of the ripple (due to SBS) and the coupled mode. Fig. 19 shows a time resolved Thomson scatter frequency spectrum taken at $7\frac{1}{2}^o$. The SBS ripple and ω_p,k_i mode (blue shifted) are seen to coexist in time. Note however that the SBS ripple turns on earlier and turns off later than the ω_p,k_i mode. This is believed to occur because the SBS is a non-resonant process and has a lower threshold and begins to grow exponentially early in the CO_2 laser pulse. Excitation of the beat wave on the other hand is a resonant process and can proceed only after the plasma is brought to the

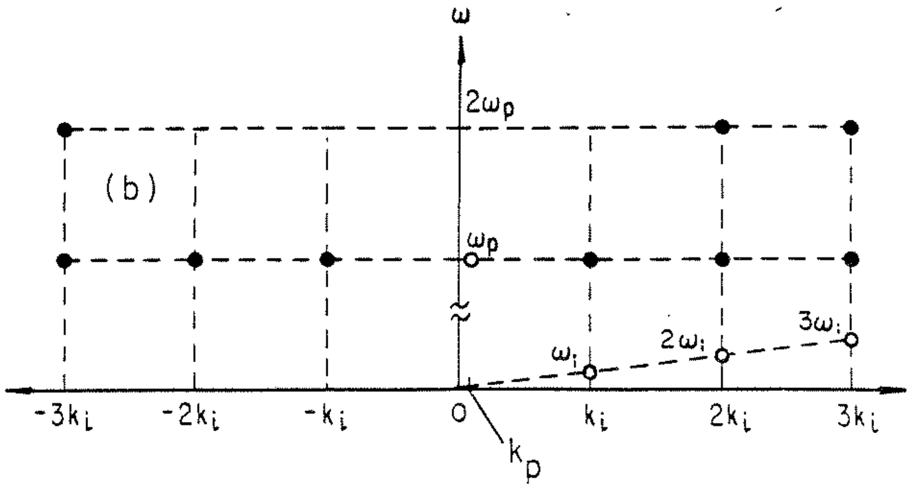

Fig. 18: Summary of the electrostatic modes which have thus far been observed in our experiments. Shown are the beat wave and SBS ion wave harmonics (open dots) as well as those modes exhibiting the signature of coupled modes (solid dots, fundamental in ω_p and harmonic in k_i)

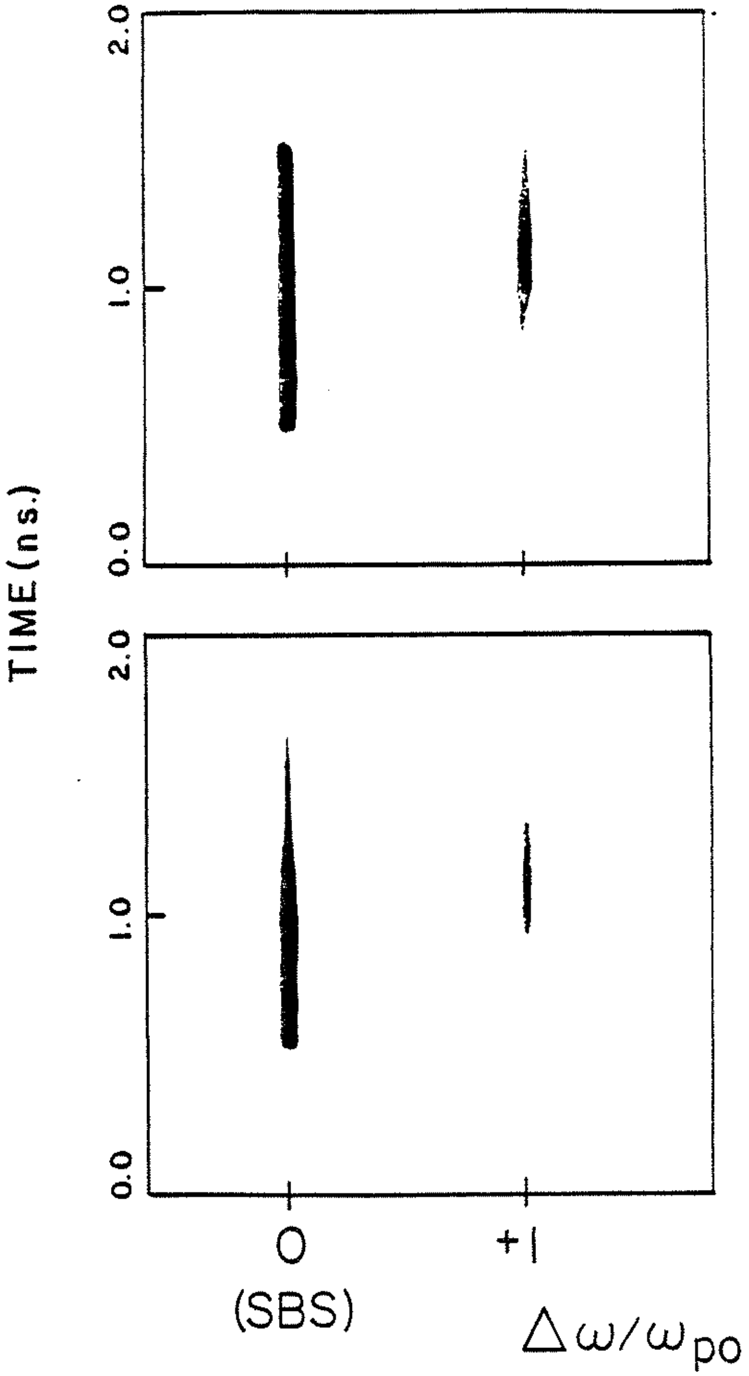

Fig. 19: Two typical examples of temporally resolved Thomson scatter frequency spectra taken at 7.5° ($k_{es} \cong k_i$) with two frequency laser excitation obtained on two separate occasions. The SBS and coupled mode are seen to coexist in time as expected.

fully ionized resonant density by the CO_2 laser. Once the resonant plasma density is finally reached the plasma beat wave, and therefore the coupled mode, are constrained to grow at the growth rate given in Ch. II, $\gamma = \frac{1}{4}\alpha_1\alpha_2\omega_{po}$. Note also that, due to finite laser pulse risetime, the growth rate early in the laser pulse is lower than at the peak of the pulse since the α's are functions of time. This effect delays the growth of the beatwave even further.

ESTIMATION OF MODE FIELD SATURATION AMPLITUDES

The theory of Ch. II provides a model with which to predict the field amplitude at saturation of the various coupled modes and the beat wave. Experimental estimates of the mode field amplitudes can be obtained from Eq. 43 where we assume the same mode spatial profile (i.e. L_p) as was directly measured for the beat wave. However some subtleties in the application of this formula to the two Thomson scatter geometries used in our experiments warrent further consideration.

Eq. 43 relates the fraction of scattered Thomson scatter probe beam power to the mode strength measured in $\tilde{n}/n_0$. This formula takes into consideration both the spatial and temporal coincidence of the mode of interest and the probe beam. While temporal conincidence is fixed for either geometry by the CO_2 and ruby laser pulse widths, the spatial coincidence (i.e. spatial overlap) factor L_p/L_r depends on the scatter geometry (i.e. large or small angle) used. Fig. 20 summarizes the situation for three different cases of probe beam and plasma mode spatial overlap. In Fig. 20a the ruby laser beam is seen to have a larger axial extent than the electrostatic mode as was the case with the cylindrical focus system used to diagnose the beat wave at 0.4°. The factor L_p/L_r in Eq. 43 correctly compensates for this situation when estimating the mode field amplitude. Fig. 20b shows the situation when the Thomson scatter probe beam and the electrostatic mode perfectly overlap in space. This is the case for Thomson scatter of the CO_2 laser beam from the beat wave which gave rise to the observed forward electromagnetic scatter spectrum (Stokes and anti- Stokes lines). Fig. 20c shows the situation for the spherical optics system used for large angle Thomson Scatter. Although the Thomson scatter probe beam samples only a portion of the electrostatic mode volume the overlap is complete for that portion of the volume probed. Thus in Fig. 20c we must take $L_p/L_r = 1$ That is, L_p/L_r never exceeds unity for large angle scattering measurements (which utilize spherical Thomson scatter optics.) Note that the transverse dimensions of the electrostatic mode volume and the probe beam are such that we have $L_{p\perp}/L_{r\perp} = 1$ for both large angle and small angle cases since the ruby transverse focal dimension is assumed to always be smaller than the electrostatic mode dimension due to the relative size of the Ruby and CO_2 laser wavelengths.

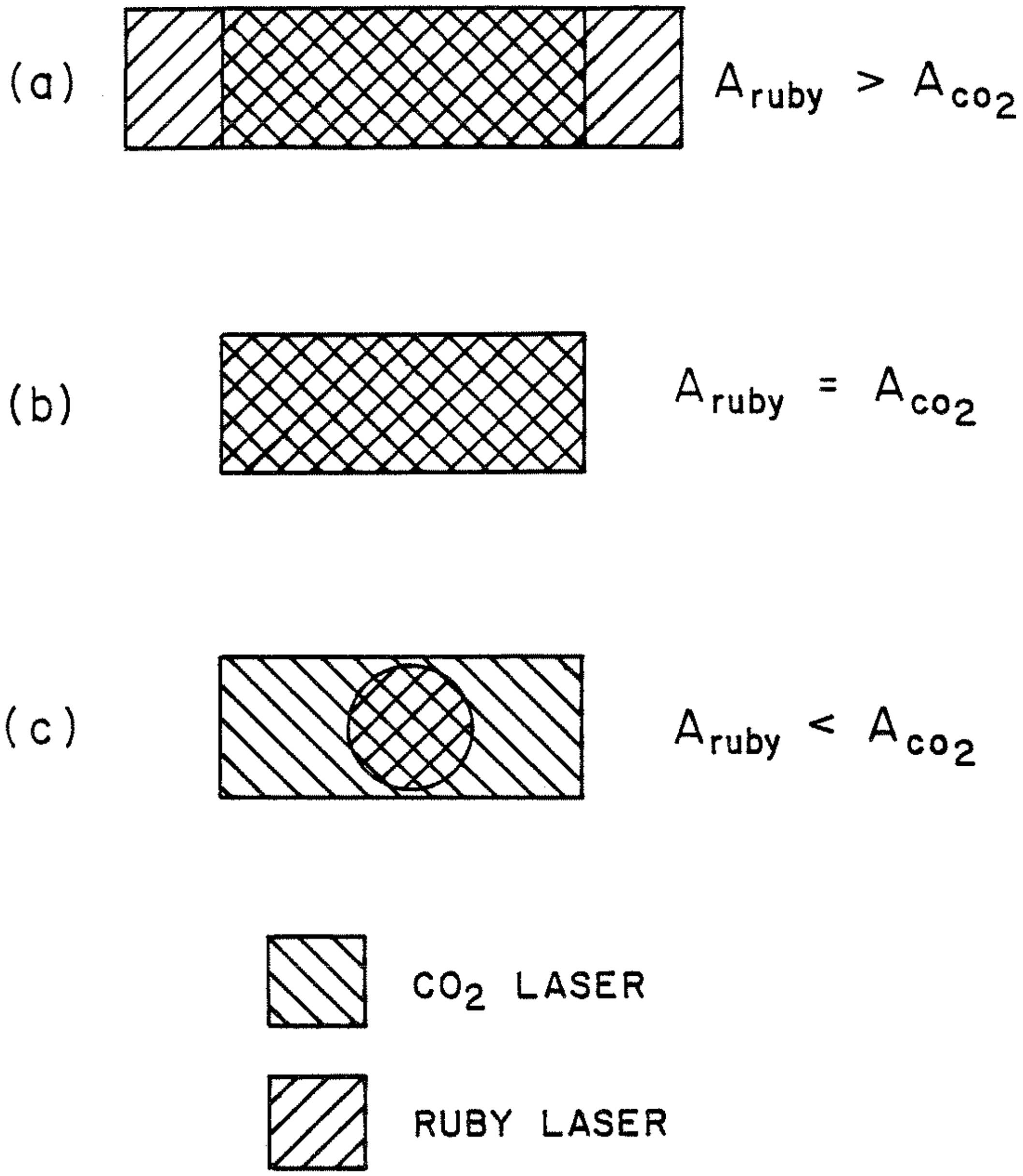

Fig. 20: Geometry of the Thomson scatter volume when (a) the Ruby laser focal spot is larger than the CO_2 laser focal spot as is the case for small angle Thomson scattering, (b) when the Ruby laser focal spot is the same size as the CO_2 laser focal spot, and (c) when the Ruby laser focal spot is smaller than the CO_2 laser focal spot as is the case for large angle Thomson scatter.

In light of these considerations we compare in Fig. 21 the predicted and observed electrostatic field amplitudes. The theoretically predicted amplitudes follow from the saturation values calculated above for warm and cold plasmas (Eqs. 25, 33) where for warm plasmas we have taken $p = 2$ and $\alpha_1\alpha_2 = 3 \times 10^{-4}$ as in the experiment. For reference we also compare the predicted beat wave saturation amplitude for relativistic detuning. The measured amplitude of the beat wave is ≅ 9 ± 6 %. From Eqs. 35 we expect a saturation amplitude of ≅ 13 % (8 % including pump risetime) for relativistic detuning and ≅ 3 % for saturation by mode coupling. Thus the measured beat wave amplitude is consistent with both the relativistic detuning and mode coupling saturation models. However, observations of the coupled modes and the fair agreement between their theoretically predicted and experimentally measured amplitudes are strongly suggestive of the significance of the contribution of the mode coupling saturation mechanism in our experiment.

OTHER FEATURES OF THE ELECTROSTATIC SPECTRUM

In this section we discuss a number of interesting results obtained from Thomson scatter studies of the electrostatic mode spectrum. Although these results often complicate the

	$E(\Psi_0)$	$E(\Psi_1)$
EXPERIMENT	3 – 9 %	.09 – 0.9 %
RELATIVISTIC DETUNING	8 %	———
COLD PLASMA MODE COUPLING	0.6 %	0.5 %
WARM PLASMA MODE COUPLING	3 %	0.8 %

Fig. 21: Summary of the theoretically predicted and experimentally estimated electrostatic field amplitudes for the beat wave (Ψ_0) and first coupled mode ($\Psi_{\pm 1}$) for $p \cong 2$ and $\varepsilon \cong 0.04$ as in the experiment.

interpretation of the physics of the experiment, they serve to illustrate the importance of the interrelations of the various physical processes occuring in the plasma.

Under two frequency excitation the nature of the electrostatic spectrum has been investigated for several electrostatic k's as described above. The spectra presented there are in good agreement with the mode coupling model of Ch. II. However Fig. 22 shows an example of a $2k_{CO_2} \cong k_i$ Thomson scatter frequency spectrum obtained under two frequency excitation which, although partially explained by the mode coupling model, contains additional spectral features. The central peak is again due to Thomson scatter from the SBS produced density ripple. The peak on the left is blue shifted from the zero frequency SBS spectral peak by the resonant plasma frequency ω_{po} ($\Delta\omega_{lasers} = \omega_{po}$) and is believed to be an ω_{po}, k_i coupled mode. Also seen are a large spectral peak blue shifted from the zero frequency peak by about $0.38\omega_{po}$ and a small spectral peak blue shifted by $0.68\omega_{po}$. These modes are believed to arise due to the non-resonant excitation of low frequency, $k = k_i$ electron plasma waves by SRS at points along the axis within the CO_2 depth of focus where the plasma density is different from the beat wave resonant density.

Fig. 23 shows another case where the low density $k = k_i$ mode occurs with a frequency exactly equal to $\frac{1}{2}\ \omega_{po}$. This is a

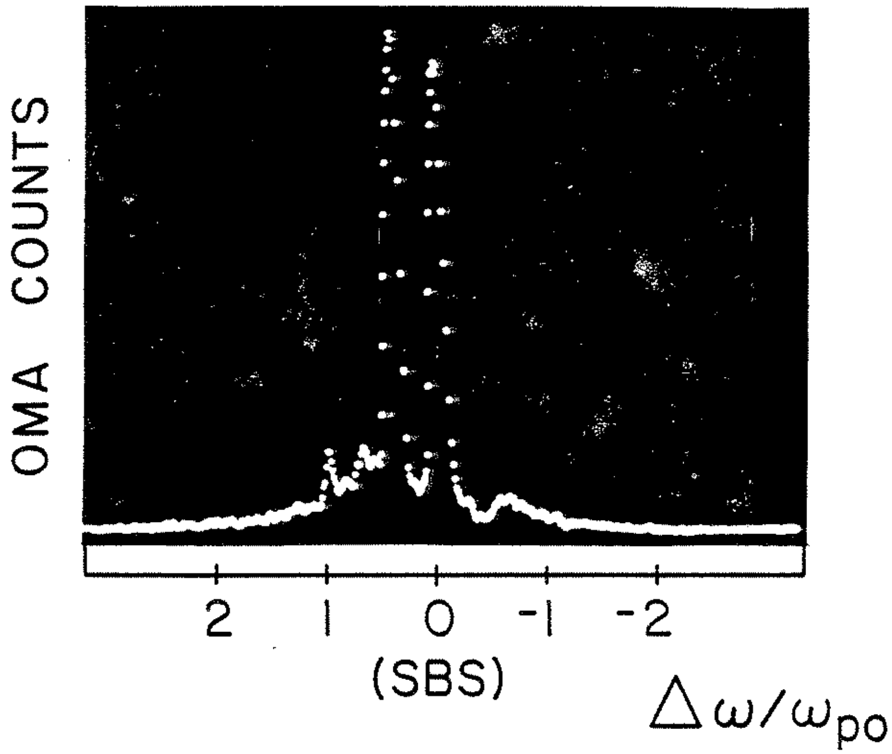

Fig. 22: Thomson scatter frequency spectrum taken an 7.5° for single frequency excitation showing peaks shifted by $0.38\omega_{po}$ and $0.69\omega_{po}$.

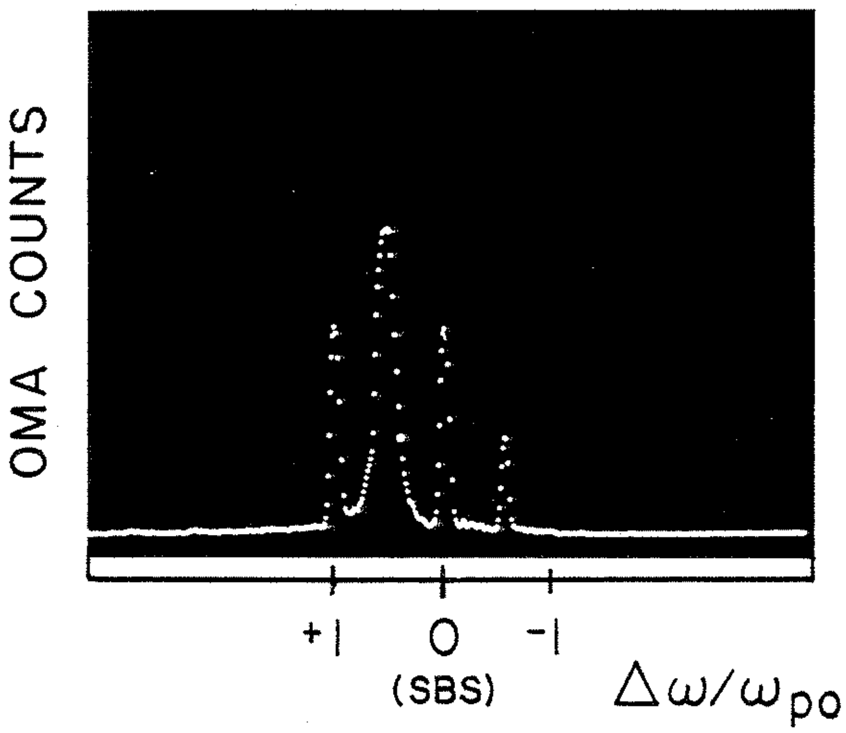

Fig. 23: Thomson scatter frequency spectrum taken at 7.5° for two frequency excitation. Clearly seen are spectral features shifted by exactly ω_{po} and $0.5\omega_{po}$.

particularly interesting case because, under these conditions, it is possible to parametrically excite an unstable mode with $\Delta\omega_{lasers} = 2\omega_{es} \cong 2\omega_p$ and $\Delta k_{lasers} = 2k_{es}$ where ω_p is the plasma frequency of the sub-resonant density plasma (i.e. $\omega_p = \frac{1}{2}\,\omega_{po}$)[6]. This mode is similar in character to the resonantly excited beat wave in that it too has $v_\phi = \omega_p/k_{es} \cong c$. While the low frequency ($\frac{1}{2}\,\omega_{po}$) mode in Fig. 23 could be due to a low density SRS driven plasma wave, it is interesting to speculate on the possibility of this mode arising from mode coupling of the parametrically excited $\frac{1}{2}\omega_{po},\vec{k}_i$ mode. Note also the presence of its red shifted complement, $\frac{1}{2}\omega_{po},-\vec{k}_i$. Unfortunately the Thomson scatter measurements used to obtain the k-spectrum of the beat wave (Fig. 11) were not extended to include observations at $\frac{1}{2}\,k_p$ where one would expect to observe the $\frac{1}{2}\omega_{po},\frac{1}{2}k_p$ mode directly, and we therefore have no conclusive evidence for the existence of of the $\frac{1}{2}\omega_{po},\frac{1}{2}\,k_p$ mode itself.

Assuming the blue shifted $\frac{1}{2}\omega_{po}$ mode is the quarter-resonant density, parametrically excited electron plasma wave it is not unreasonable to assume that the blue shifted ω_{po} mode can arise from mode coupling of the second harmonic of the $\frac{1}{2}\omega_{po},\frac{1}{2}k_p$ mode. Note in Fig. 23 that the relatively large amplitude of the $\frac{1}{2}\omega_{po}$ spectral peak compared with the ω_{po} spectral peak tends to support this assumption since one expects the coupled mode amplitudes to reflect the relative amplitudes of the fundamental and second harmonic parent mode amplitudes (c.f. Eq. 33c). It is also interesting that a mode identical in character (same ω and k) to the resonantly excited beatwave can be excited in a non-resonant density plasma; that is the beat wave fundamental is the same as the second harmonic of the low frequency, parametrically excited mode. The absense of the $\frac{1}{2}\omega_{po}$ mode at $2k_i$ and $3k_i$ (i.e. higher order mode couplings of the low frequency mode) may be due to the enhanced thermal quenching of the coupling in the quarter-resonant density plasma where $k_i\lambda_d$ is twice as large as in the resonant density case (c.f. Ch. II)

Perhaps the experimental evidence most supportive of the viability of the mode coupling mechanism was obtained under single frequency laser pumping of the plasma. As discussed in Ch. 1, under two frequency pumping many ambiguities exist in the Thomson scatter spectrum because of the similarity of the SBS, SRS and CPOM wave numbers ($k_{SRS} \cong k_{SBS} \cong k_{CPOM}$). Under single frequency pumping the CPOM process is not possible and the red shifted mode $\omega_p, m\vec{k}_i$ can only arise from mode coupling. Two Thomson scatter spectra taken under single frequency pumping which illustrate this point are shown in Fig. 24 for $k_{es} = k_i$ and $k_{es} = 3k_i$. It is important to distinguish between beat wave mode coupling and the mode coupling of SRS produced electron plasma waves illustrated in Fig. 24. Since the spectrum in Fig. 18a was obtained for single frequency pumping the primary waves are SRS driven plasma waves (the spectral peak which is blue shifted by ω_{po}). In Fig. 24a the red shifted

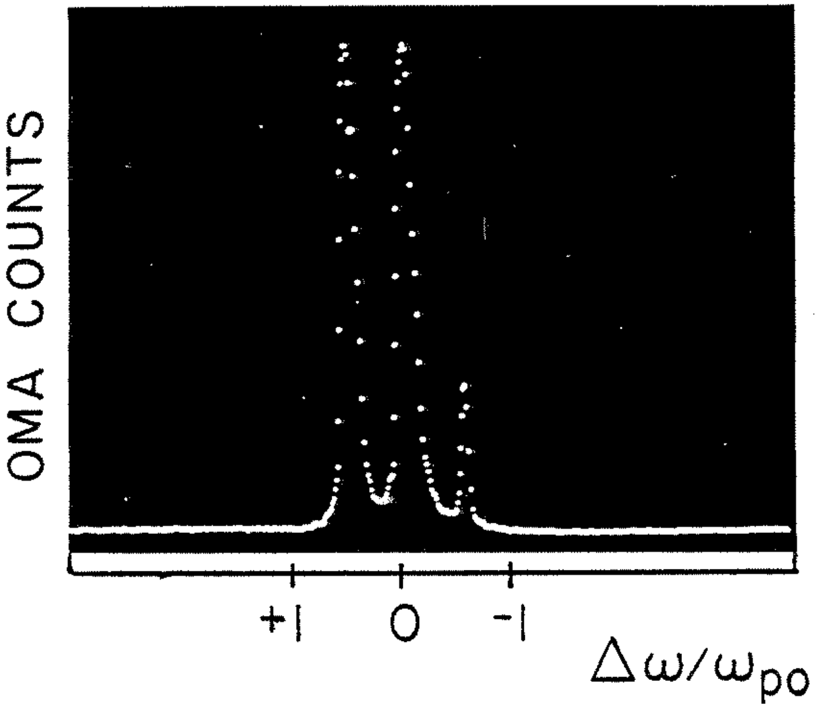

Fig. 24a: Thomson scatter frequency spectrum taken at 7.5° for single frequency laser excitation. Both forward and backward propagating modes symmetrically shifted from the central spectral peak (SBS) by ω_p are clearly observed and attributed to coupled modes driven by SRS.

peak arises when the $k = k_i$ primary wave undergoes an $m = -2$ coupling to the $k = -k_i$ mode. Similarly blue and red shifted peaks in Fig. 24b arise when the $k = \vec{k}_i$ primary mode undergoes an $m = +2$ (to $+3k_i$) and an $m = -4$ (to $-3k_i$) coupling respectively.

Due to the complexity and interdependencies of the many modes and excitation mechanisms it is not possible to decisively attribute a given observed mode to one particular mechanism. A further understanding of the various contributions to the observed modes could be gained by performing high temporal, frequency, and wavenumber resolution Thomson scattering experiments. Lacking such sophisticated diagnostics and the shot to shot reproducibility necessary to gather meaningful statistics, we attempted to correlate the various observables in the experiment. The results of such attempts to correlate observables were largely inconclusive. This is due primarily to the difficulty in isolating the many effects which any one diagnostic probes: SRS backscatter integrates along z; Thomson scattering is sensitive to both the interaction length and beat wave intensity which may have shot to shot variations; SBS can affect both SRS and beat wave excitation and further complicate the COM-CPOM mode spectrum. A powerful technique has subsequently been employed by other researchers at UCLA which provides unambiguous frequency information on the SBS spectrum and has made correlation of some observables possible. However for the work discussed in this

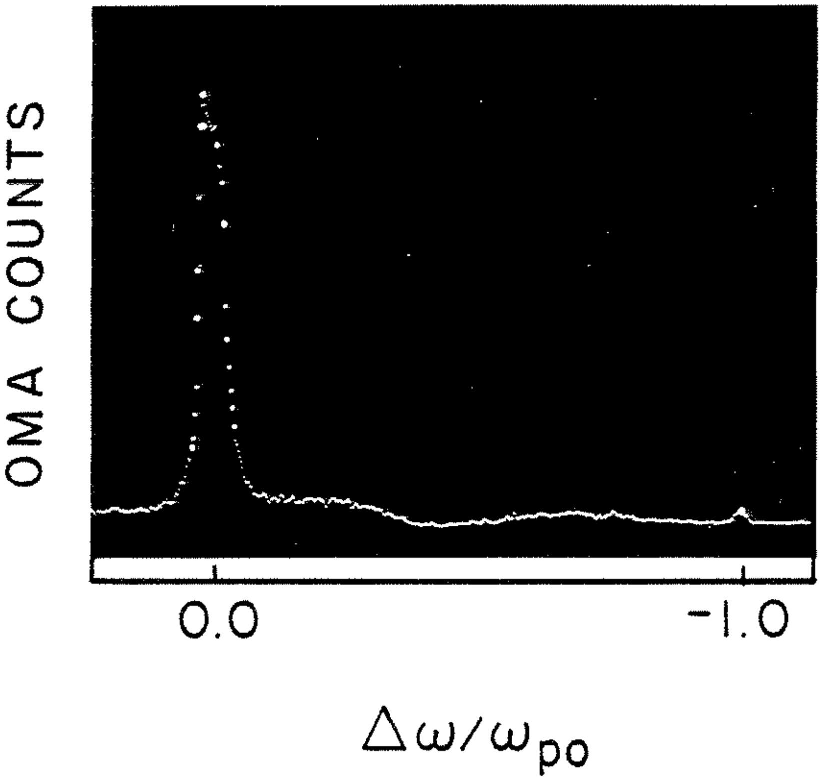

Fig. 24b: Thomson scatter frequency spectrum taken at 15° for single frequency laser excitation. Shown are the SBS and $-\omega_p$ coupled mode spectral features.

thesis we have employed computer simulations to aid us in addressing experimentally unresolved issues. The simulations are the subject of Ch. V.

CHAPTER V: COMPUTER SIMULATIONS OF BEAT WAVE MODE COUPLING

Use has been made of computer simulations to further corroborate the theoretical predictions and experimental observations of the mode coupling process and the coupled mode spectrum. Particular attention has been directed toward the study of the electrostatic k-spectrum and the observation of thermal effects.

These simulations were conducted using the particle code "WAVE"[28]. WAVE is a fully-relativistic, electromagnetic, particle in cell code. The simulations were carried out in essentially one spatial dimension on a 2 x 1500 grid of normalized dimensions 1 x 100 (normalized to c/ω_{po}). The code calculates and increments the electrons' positions and velocities for each time step. The positions and velocities are then used to calculate the new charge and current densities. The resulting fields and forces on the particles (electrons) are then calculated and the process is continued for the allotted number of time steps for which the simulation is to be run. In all simulations reported on here a total of 32,000 electrons was used. To model the density ripple the electrons and a fixed ion background were initialized at time t=0 with a sinusoidal ripple.

Before presenting the results of the simulations it is useful to establish a workable notation and describe the normalization. In the simulations, the laser pump is incident from the left along the x-axis and is polarized along $\hat{y}$. Distances are normalized to the collisionless skin depth c/ω_{po}, frequencies are normalized to the background (excluding the ripple) plasma frequency ω_{po}. The k's are normalized to ω_{po}/c and are denoted by "kx" in the figures (longitudinal wavenumber). For display purposes the wavenumbers are given in units of "mode number", the number of wavelengths of a given sinusoidal mode that will fit within the simulation box: kx(m.n.) = $kL/2\Pi$ where k and L are given in units of ω_{po}/c and c/ω_{po} respectively. Because L was chosen to be $100c/\omega_{po}$ for the simulations reported on here, k(m.n.) = 15.9 $k(\omega_{po}/c)$.

To model beat excitation one wants $\Delta\omega_{lasers} = \omega_{po}$. In our simulations the laser frequencies were chosen to be $\omega_1=5$, $\omega_2=4$. In simulation units, the dispersion relation for light waves in a plasma is

$$\omega_{1,2}^2 = 1 + k_{1,2}^2. \tag{43}$$

The chosen laser frequencies give a plasma wave number of $k_p = (24)^{1/2} - (15)^{1/2} = 1.03$. We were interested in a ripple of wavenumber $k_i > k_p$. For the simulations presented, the ripple wavenumber k_i was chosen to be either $2(24)^{1/2}$ or $1.2(24)^{1/2}$.

OBSERVATIONS OF MODE COUPLING

Figs. 25a,b,c show the results of one simulation with ε=0.25, p=0.508, $\alpha_1=\alpha_2=.05$ and $k_i=2(24)^{1/2}$. The simulation was set up to record plasma parameters every $\Delta(\omega_{po}t)$ = 30 (every 500 time steps). At $\omega_{po}t$ = 0 the system is intialized with the above parameters. At $\omega_{po}t$ = 60 the beat wave (Ψ_0) and first ($\Psi_{\pm 1}$) coupled modes are seen to be well established above the noise. The modes are discrete in k as expected from theory. At $\omega_{po}t$ = 90 the coupled modes and beat wave have continued to grow and the electron distrubution function begins to show evidence of electron heating in the longitudinal direction as the waves begin to trap background electrons. The heating is anisotropic in v_x because the right propatating coupled mode (Ψ_{+1}) has a lower phase velocity and can more efficiently trap background electrons than the somewhat faster (Ψ_{-1}) mode which travels to the left. Note that "heating" also arises due to the quiver motion of the electrons in the beat wave electric field even though no appreciable fraction of the electrons can be trapped by a beatwave traveling with $v_\phi \cong c$. At $\omega_{po}t$ = 120 the second coupled modes are observed to emerge from the noise at precicely the predicted, discrete wavenumbers. As time progresses the plasma continues to heat due to wave particle interactions between the first and second coupled modes and the plasma electrons. Eventually ($\omega_{po}t$ = 210,240) the beatwave saturates and the coupled modes begin to decrease in amplitude due to the increase in Landau

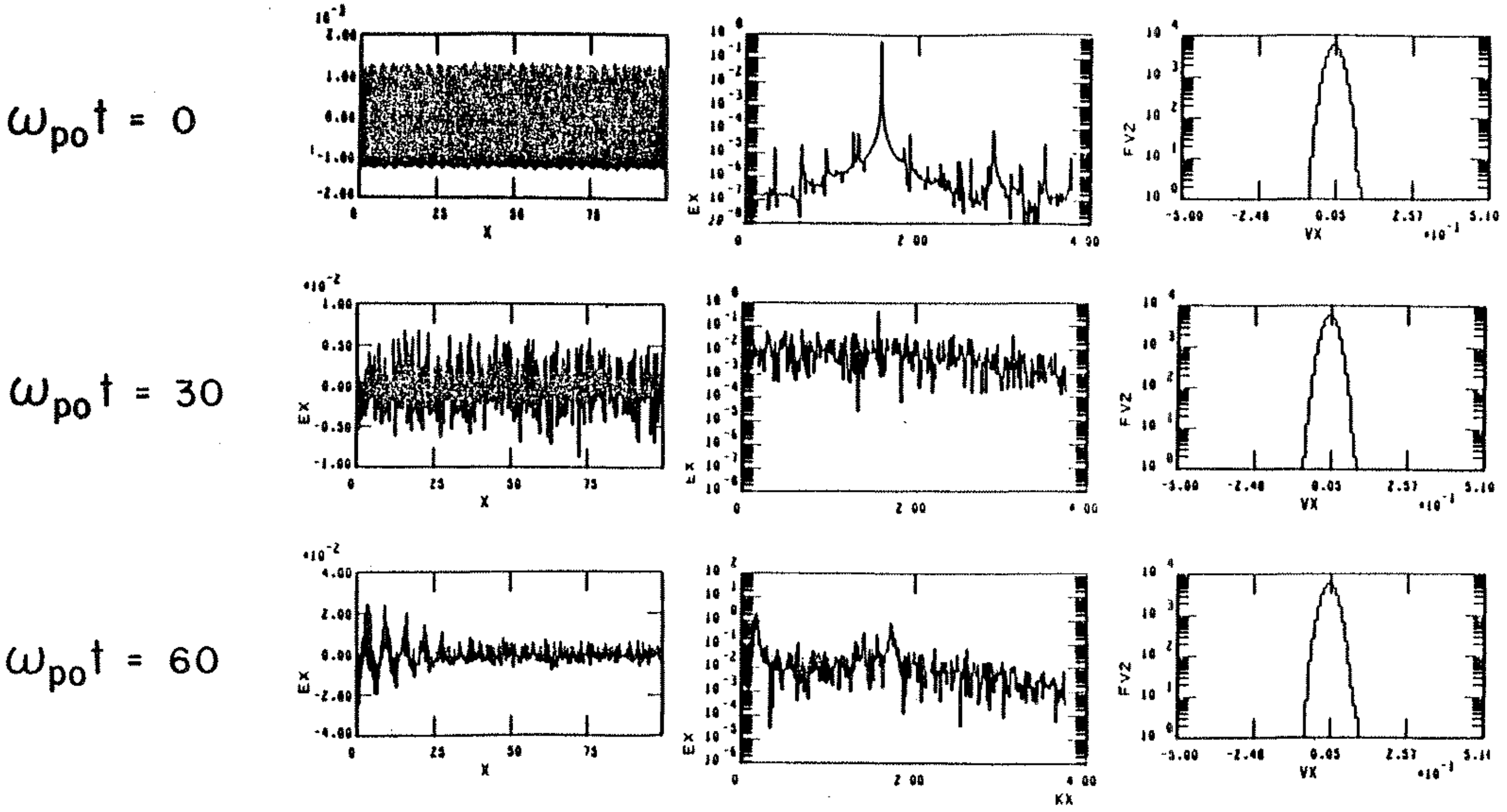

Fig. 25a: Plots of $E_{long.}(x)$, $E_{long.}(k_x)$, and the electron distribution function FV2 obtained from simulation (ϵ=0.25, α_1=α_2=.05, k_i=2(24)$^{1/2}$, and p=0.508). $E_{long.}(x)$ is normalized to $m c \omega_{po}/e$. Refer to the text for a description of the normalizations used for the x and kx axes.

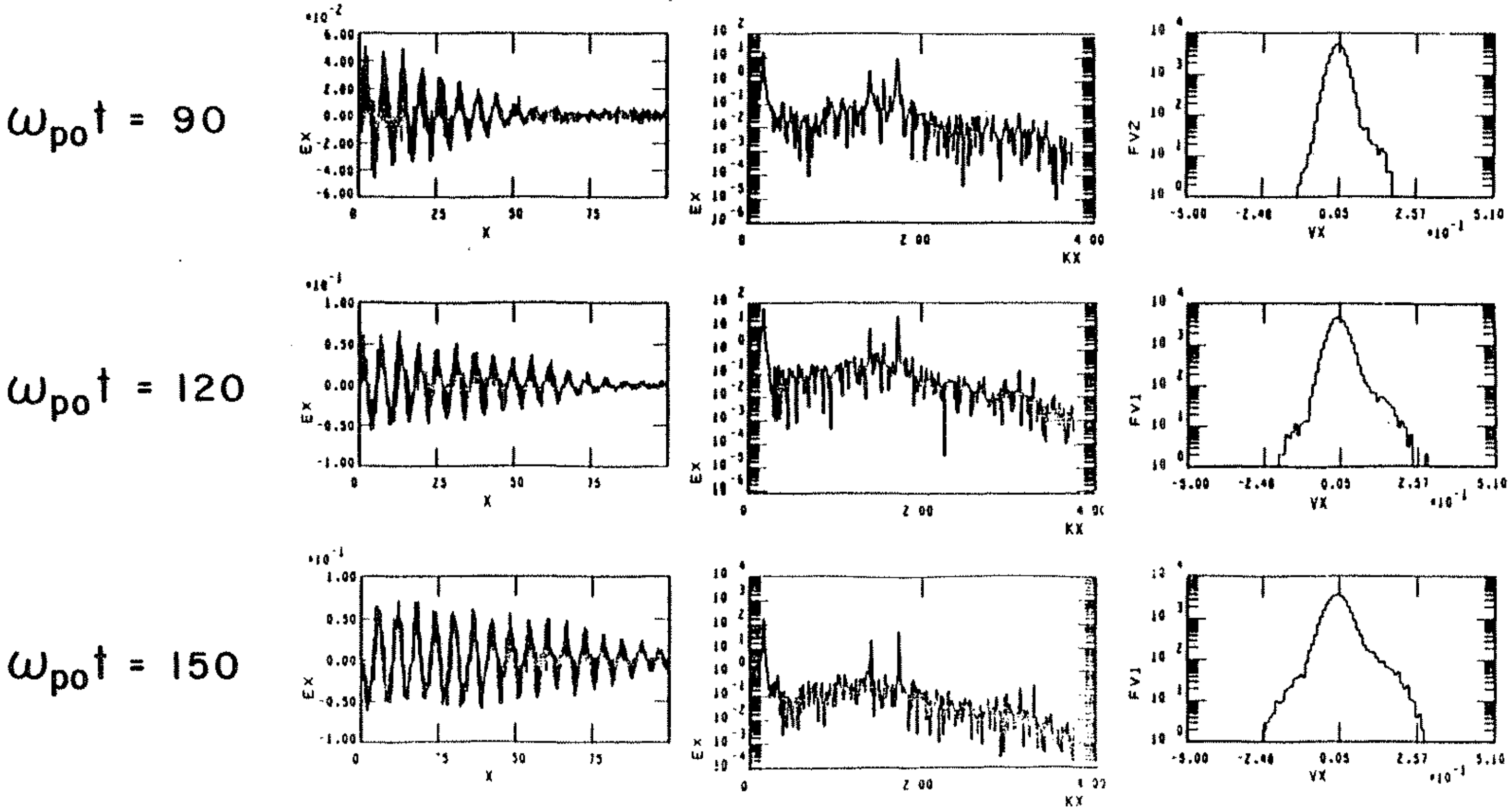

Fig. 25b: Plots of $E_{long.}(x)$, $E_{long.}(k_x)$, and the electron distribution function FV2 obtained from simulation (ϵ=0.25, α_1=α_2=.05, k_i=$2(24)^{1/2}$, and p=0.508). $E_{long.}(x)$ is normalized to $mc\omega_{po}/e$. Refer to the text for a description of the normalizations used for the x and kx axes.

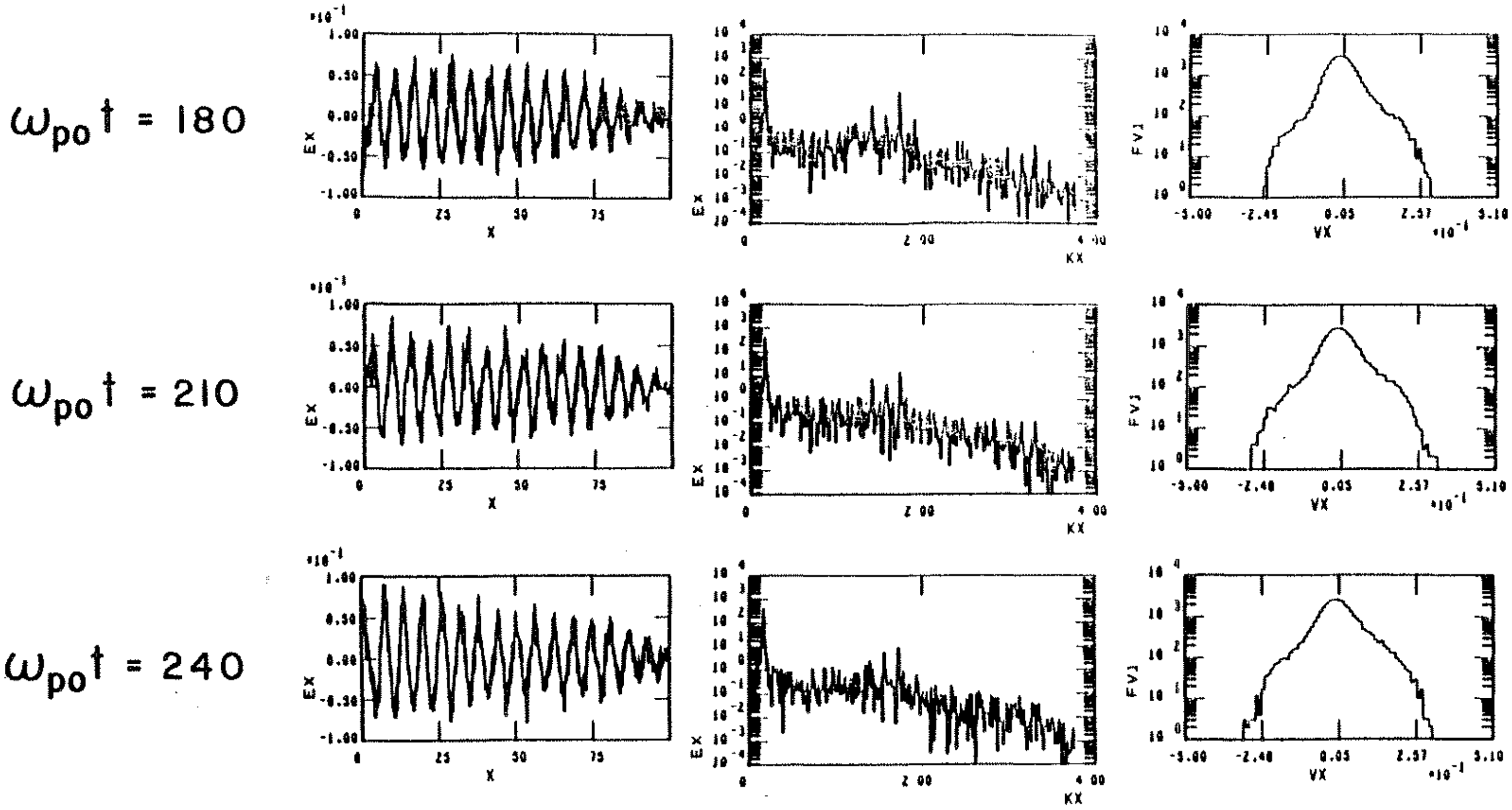

Fig. 25c: Plots of $E_{long.}(x)$, $E_{long.}(k_x)$, and the electron distribution function FV2 obtained from simulation (ϵ=0.25, α_1=α_2=.05, k_i=$2(24)^{1/2}$, and p=0.508). $E_{long.}(x)$ is normalized to $mc\omega_{po}/e$. Refer to the text for a description of the normalizations used for the x and kx axes.

damping and the decrease in the coupling efficiency between the fixed frequency driver and the now frequency shifted Bohm-Gross $\Psi_{\pm 1}$ and $\Psi_{\pm 2}$ modes. The supression by damping of the higher-k (short wavelength) components is evident in both the electric field waveforms and the k-spectra where the amplitudes of the $\Psi_{\pm 1}$ and $\Psi_{\pm 2}$ modes have fallen below the noise level.

SELF STABILIZATION OF SATURATION BY MODE COUPLING

In Ch. II it was postulated that saturation of the beat wave could be avoided by thermally quenching the coupling process. If the plasma is heated to a sufficient temperature the Bohm-Gross frequency shift of the $\Psi_{\pm 1}$ modes is so large that the frequency difference between the modes and the driver cannot be accomodated by the variation in $\omega_p(x)$ in the density ripple[7,8]. In this case the coupled modes cease to be excited and no longer provide a sink for beat wave energy. In the absense of those losses the mode coupling saturation mechanism is defeated and the beatwave amplitude is limited only by relativistic detuning.

Figs. 26a,b show the results of a simulation with $\epsilon=0.1$, $\alpha_1=\alpha_2=.05$, and $k_i=1.2(24)^{1/2}$. In addition the electrons were initialized at $\omega_{po}t=0$ with zero thermal motion to effect a "cold start". At $\omega_{po}t = 60$ both the electric field wave form and the k-spectrum show strong mode coupling while the electron distribution

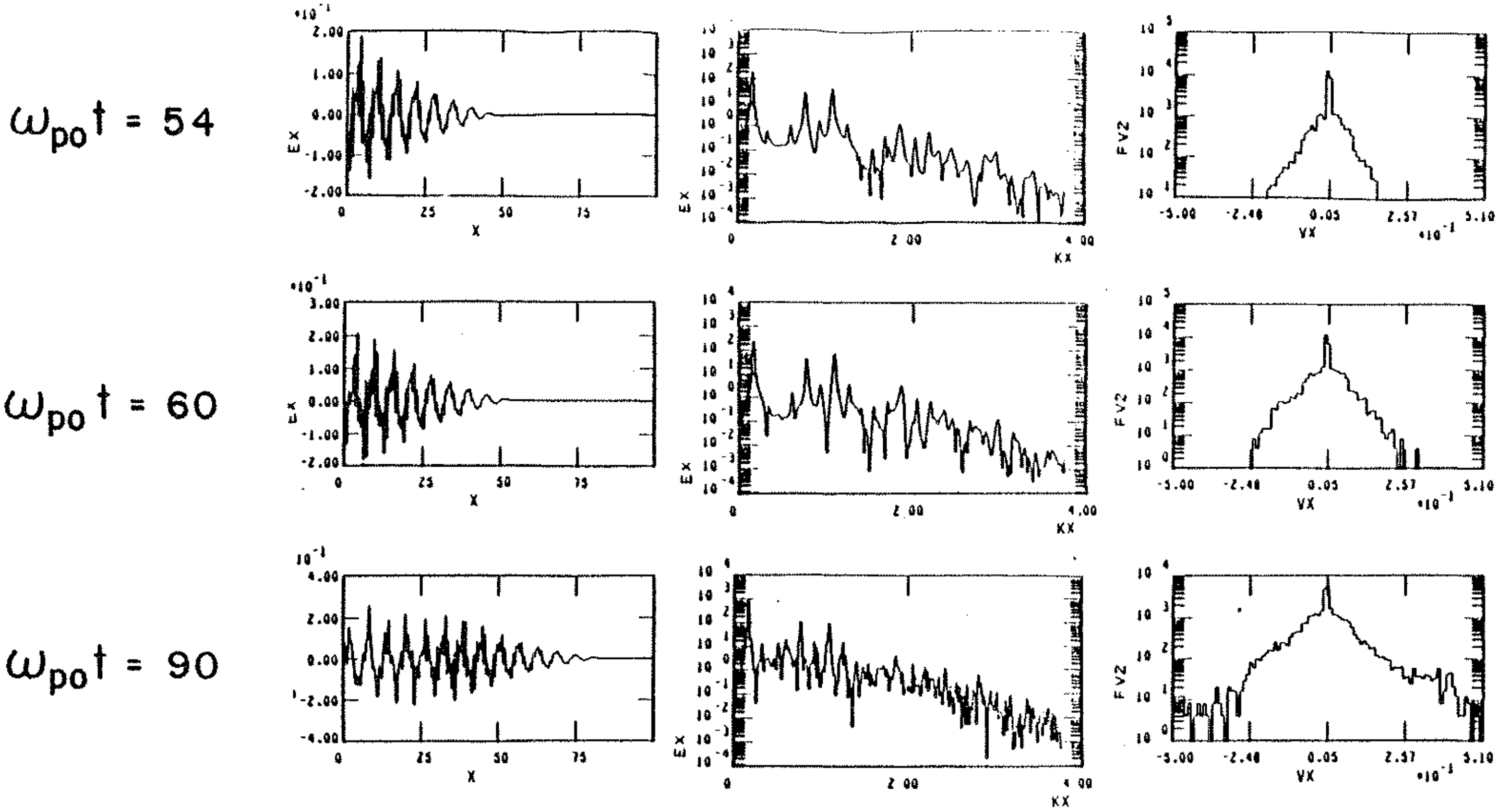

Fig. 26a: Plots of $E_{long.}(x)$, $E_{long.}(kx)$, and the electron distribution function FV2 obtained from simulation (ϵ=0.1, α_1=α_2=.05, k_i=1.2$(24)^{1/2}$, and p(t=0)=0). The electrons were initialized with zero thermal motion. $E_{long.}(x)$ is normalized to $mc\omega_{po}/e$. Refer to the text for a description of the normalizations used for the x and kx axes.

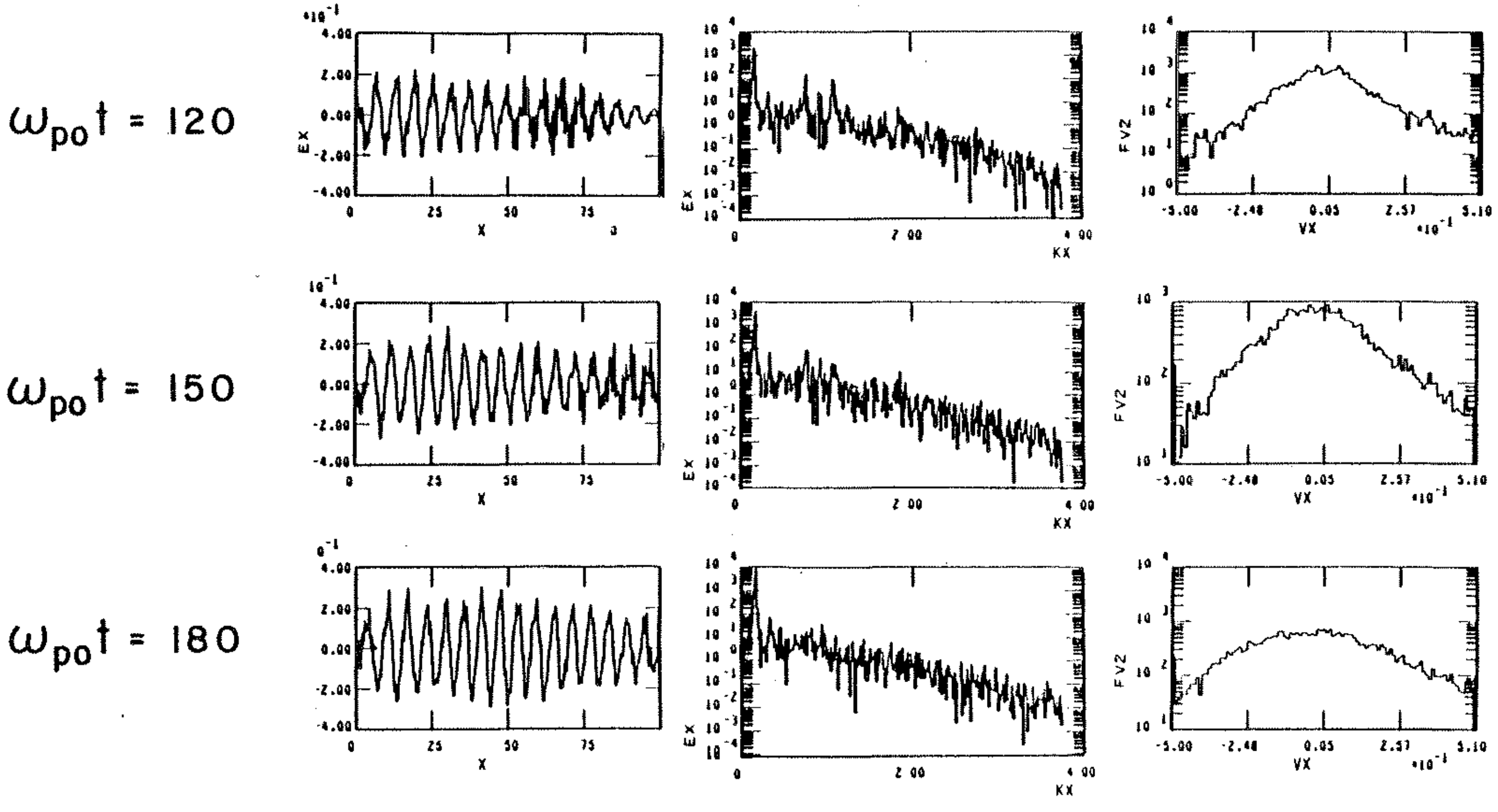

Fig. 26b: Plots of $E_{long.}(x)$, $E_{long.}(kx)$, and the electron distribution function FV2 obtained from simulation (ϵ=0.1, α_1=α_2=.05, k_1=1.2$(24)^{1/2}$, and p(t=0)=0). The electrons were initialized with zero thermal motion. $E_{long.}(x)$ is normalized to $mc\omega_{po}/e$. Refer to the text for a description of the normalizations used for the x and kx axes.

function indicates that the plasma is still quite cold ($k_i\lambda_d \leqslant 0.1$). At $\omega_{po}t = 120$ the electron distribution shows that significant plasma heating has occured and the electric field k-spectrum shows aprreciable supression of the coupled modes while the beat wave has continued to grow. Spatially the electric field waveform shows that at the back of the laser pulse, where the plasma has had longer time to heat, the waveform is devoid of high-k components. This is because the high-k components have Landau damped away and are no longer driven by the mode coupling process due to the thermally enhanced Bohm-Gross frequency shift of the heated plasma. At $\omega_{po}t = 180$ the plasma temperature has stabilized and virtually all traces of the coupled mode components of the wavenumber spectrum have vanished. At this time the beatwave has resumed its growth unabated by energy channeling to the coupled modes.

TEMPORAL EVOLUTION OF BEAT WAVE AND COUPLED MODES

Thus far the simulations have been in good agreement with the theory. In particular discreteness in wavenumber of the coupled mode spectrum and stabilization of the beat wave mode coupling saturation mechanism by thermal quenching have been demonstrated. To further explore the applicability of the warm plasma mode coupling theory it is of interest to test the theoretical predictions of the saturation amplitudes and saturation times of the beat wave and coupled modes using the results of computer simulations. However before doing so it is worthwhile to note an inherent limitation in the above simulation results.

When attempting to follow the growth in time of the beat wave and coupled modes one is naturally tempted to use the peak heights of the various modes obtained from the electrostatic k-spectra (e.g. Fig. 25). The difficulty lies in the fact that the k-spectrum represents an integration over the length of the simulation box. At later times, after the wave has progressed further accross the box, the k-spectra naturally reflect the fact that the box contains more of a given mode. In an absolute sense, the wave does not really contain more of that mode. Thus as in the $\omega_{po}t = 120$ case of Fig. 25, the amplitudes of the beat wave and coupled mode spectral peaks cannot be straight- forwardly interpreted and one cannot expect to unambiguously determine a growth curve for the beat wave or coupled modes.

To overcome this difficulty we performed simulations which sampled the electric field only in the left quarter of the simulation box (the first 375 grid points, $x = 0 - 25$). Thus for $\omega_{po}t \geqslant 25$, the field sampling region is completely filled with the beat wave field. There is still some inherent temporal averaging within the field sampling region because the leading edge of the beat wave has had less time to grow than the trailing edge.

In Fig. 27 we make a direct comparison of the temporal evolution of the beat wave (Ψ_0) and first and second ($\Psi_{\pm1},\Psi_{\pm2}$) coupled modes obtained from simulation and the warm plasma mode coupling theory. Fig. 27a shows the growth curve obtained from the simulation for $\epsilon=0.1$, $p=0.466$, and $\alpha_1=\alpha_2=.05$, and $k_i=1.2(24)^{1/2}$. The electrostatic field at the left hand side of the simulation box was sampled every $\Delta(\omega_{po}t)=10$ (every 167 time steps) and the peak amplitude of the beat wave (Ψ_0) and first ($\Psi_{\pm1},\Psi_{\pm2}$) first two coupled modes were recorded. The peak amplitudes were then plotted versus $\omega_{po}t$ as shown (the points plotted for the $\Psi_{\pm1}$ and $\Psi_{\pm2}$ modes represent the averages $\frac{1}{2}\left[E(\Psi_1) + E(\Psi_{-1})\right]$ and $\frac{1}{2}\left[E(\Psi_2) + E(\Psi_{-2})\right]$ respectively). Similarly the theoretical curves in Fig. 27b were generated by sampling the spectrum of Eqs. 31,32 at regular intervals and plotting the mode amplitudes versus $\omega_{po}t$. It is immediately evident that early in time the warm plasma mode coupling theory predicts the qualitative behaviour of the simulation fields with remarkable accuracy. The beat wave is seen to grow first in time. A short time later the first coupled mode begins to grow. After growth of the first coupled mode has stabilized, the beat wave growth is curtailed and a temporally local beat wave maximum is reached as energy is coupled out of the beat wave and into the first coupled mode. This in turn leads to diminished growth of the first coupled mode.

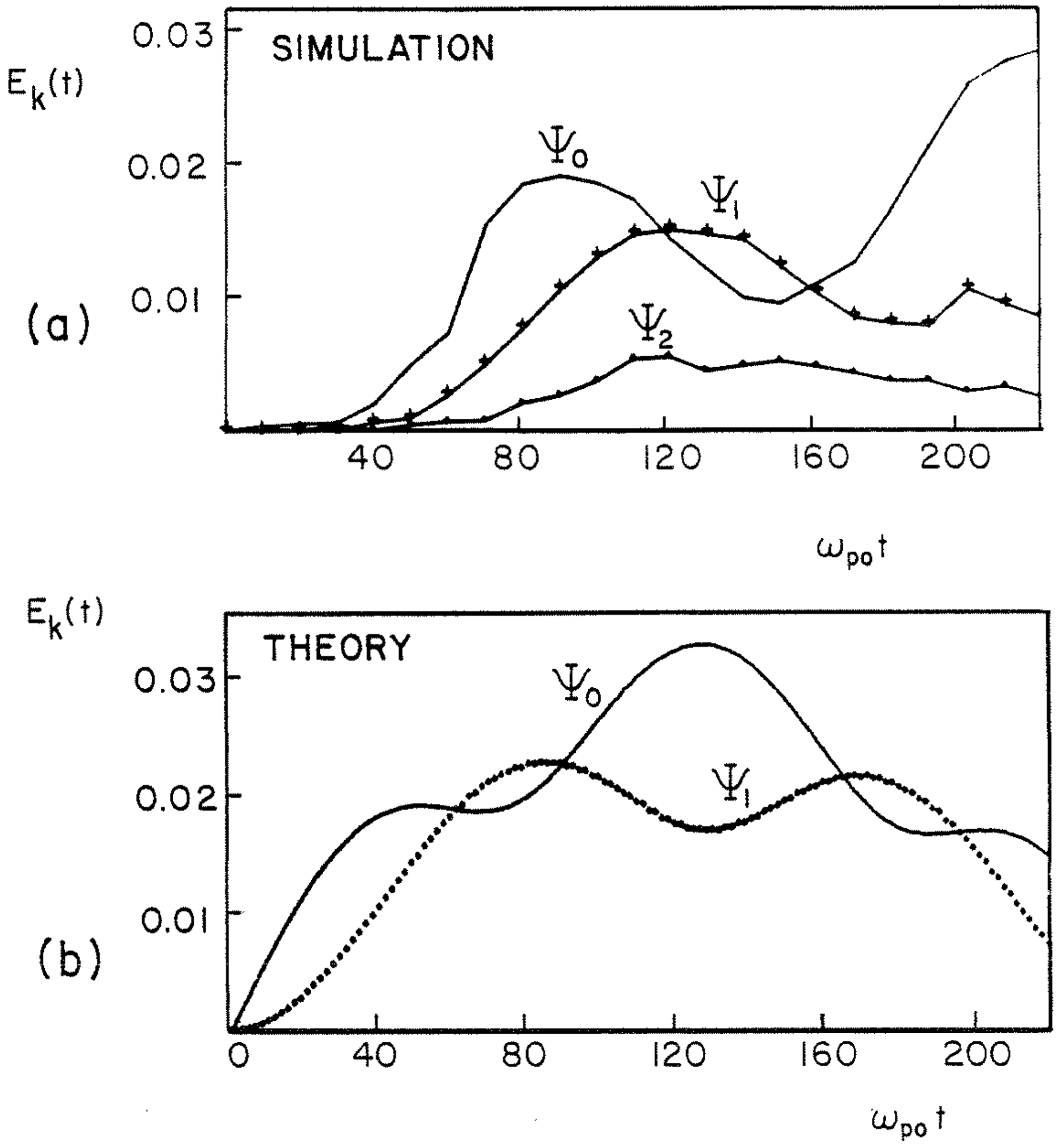

Fig. 27: Comparison of the beatwave (Ψ_0) and first ($\Psi_{\pm 1}$) coupled mode growth curves obtained from (a) Simulation and (b) Theory. In both cases E_k is normalized to $mc\omega_{po}/e$. Shown also for the simulation is the growth curve for the $\Psi_{\pm 2}$ mode, not included in the theory.

Several features of the temporal evolution curves are worthy of comment early in this discussion. It is apparent that the growth of the modes in the simulation curve lags that of the theory curves by about 30 - 50 $\omega_{po}t$. This behaviour is expected in light of two considerations. First, the beat wave required about $25\omega_{po}^{-1}$ to fill the region sampled by the field diagnostic in the simulation. Secondly, the laser rise time ($\omega_{po}t_{rise} = 50$) adds to the delay since the growth rates scale as $\alpha_1\alpha_2$ for early times (although rigorously shown only for the cold plasma case it is a reasonable approximation for early times in the warm plasma case.) Although, with the theory in its present form, one cannot hope to completely assess the effects of pump risetime, it is fruitful to take these time delays into consideration when comparing the theory and simulation growth curves. In Fig. 28 we have offset the simulation curves by $\omega_{po}t = 40$ and separately superimposed the Ψ_0 and $\Psi_{\pm 1}$ theory curves for comparison. The qualitative agreement is of course preserved but one now can see good agreement between theory and simulation regarding saturation times of the Ψ_0 and $\Psi_{\pm 1}$ modes. Refering to Fig. 28 one can see that, in some sense, the term "saturation time" is not well defined. For example in the simulation curve of Fig. 28a, the beat wave first "saturates" at $\omega_{po}t = 50$ and then again at $\omega_{po}t = 180$. This is of course not true saturation behaviour if the beat wave continues to "step up" every $\omega_{po}t \cong 140$ for $\omega_{po}t \gg 180$. However, based on the theoretical predictions for $\omega_{po}t \gg 180$, the two local maxima do represent

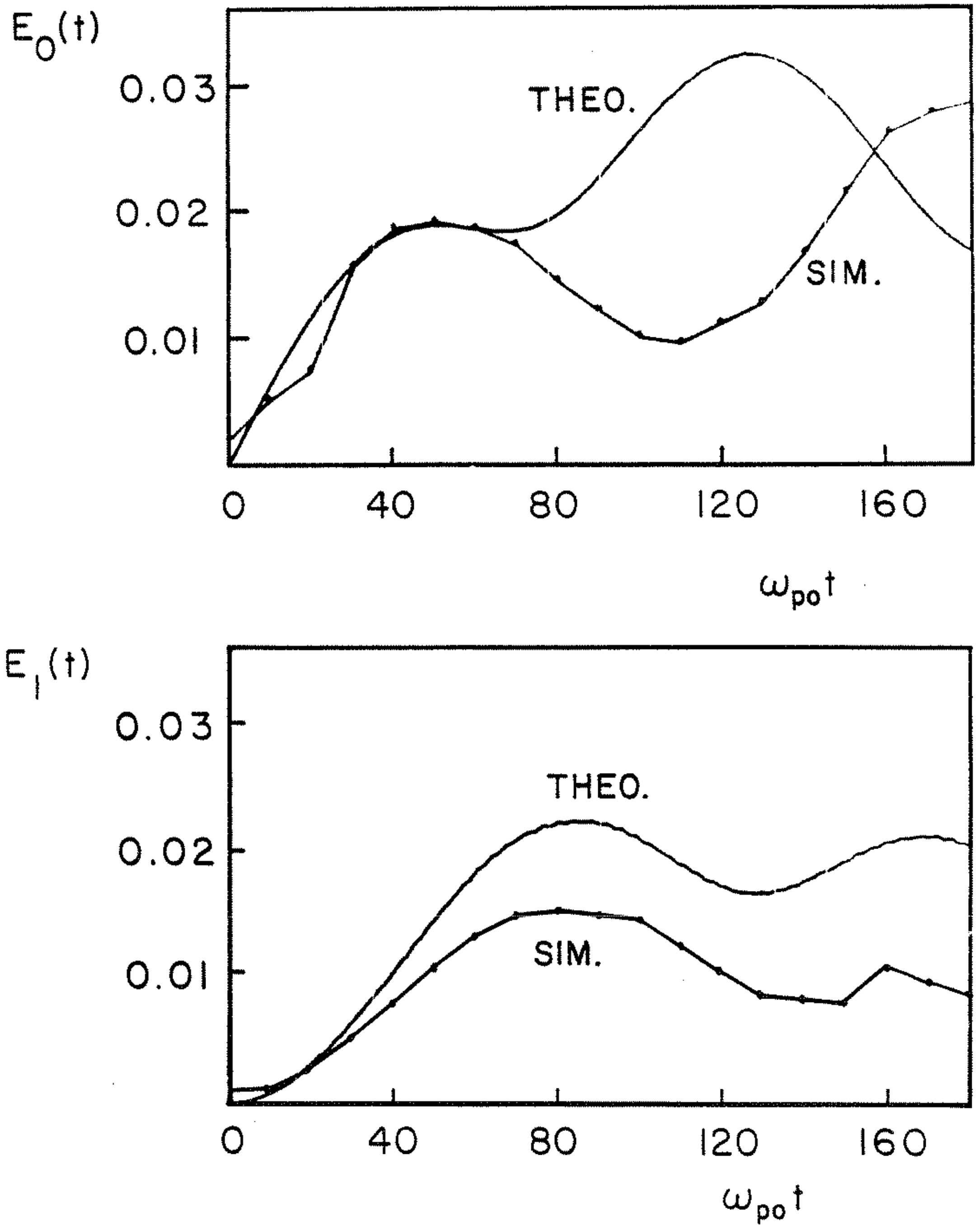

Fig. 28: Direct comparison of the theory and simulation growth curves for (a) the Beatwave (Ψ_0 mode) and (b) the first ($\Psi_{\pm 1}$) coupled mode. The simulation growth curves have been offset to the left by $40\omega_{po}t$ to compensate for the laser risetime and the "fill time" of the simulation field diagnostic region. The fields are normalized to $mc\omega_{po}/e$.

global maxima because the growth curves are periodic with periodicity $\omega_{po}t \cong 250$. This point is illustrated in Fig. 29 where we have plotted the warm plasma mode amplitudes (Eqs. 31,32) out to $\omega_{po}t = 1100$. The long time behaviour of the growth curves resembles a bumpy sine wave as one might expect upon inspection of Eqs. 31,32.

It should be kept in mind that for the parameters used in the simulation and theory results presented in Figs. 27, 28, and 29 the relativistic detuning saturation mechanism is not important since the condition $\alpha_1\alpha_2 < \left(1.6\epsilon/f(p) \right)$ (c.f. Ch. III) is clearly satisfied. In addition the time to saturation by relativistic detuning is about $500\omega_{po}^{-1}$, well beyond the $\omega_{po}t_{sat}$ of 150 relevant to the results under study here.

The theory and simulation growth curves are in excellent agreement for both the Ψ_0 and $\Psi_{\pm1}$ modes (Fig. 28a,b). In particular both the theory and simulation curves exhibit the local field maximum at $\omega_{po}t \cong 50$ for the Ψ_0 mode (beat wave). However in the simulation curves both the beat wave and first coupled mode are observed to diminish in amplitude significantly while the theory curves show little decay preceding the second maximum. In addition the Ψ_0 mode is larger and the $\Psi_{\pm1}$ mode is is smaller than for the theory curve at these later times. There are again at least two contributing factors. First, at $\omega_{po}t \cong 100$ weak plasma heating has

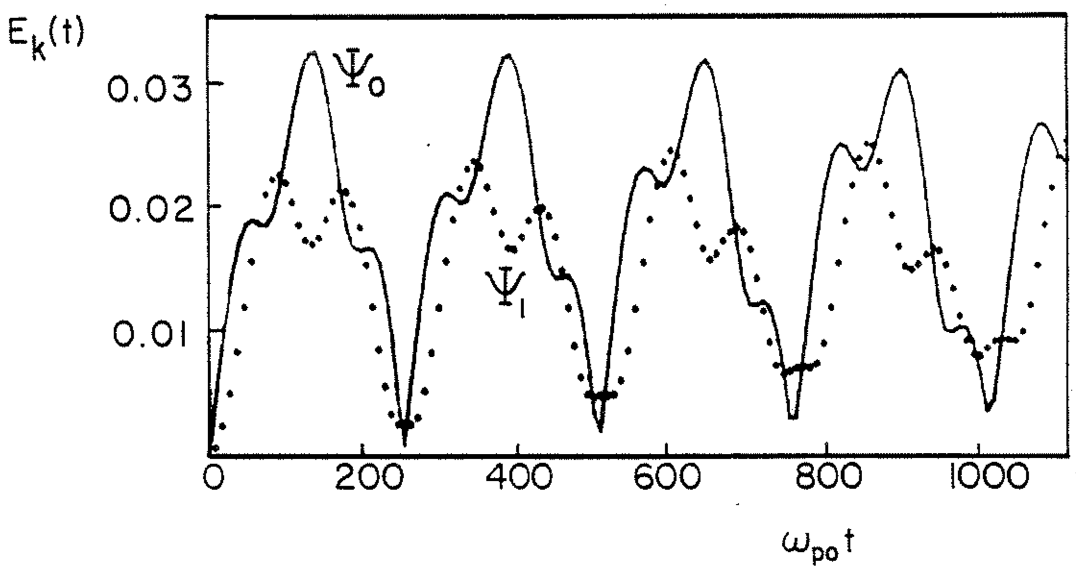

Fig. 29: Long time behaviour of the warm plasma theory solution for the beat wave (Ψ_0) and first ($\Psi_{\pm 1}$) coupled mode. The fields are normalized to $mc\omega_{po}/e$. The Ψ_0 and $\Psi_{\pm 1}$ growth curves are periodic with periodicity $\cong 250\ \omega_{po}^{-1}$. The periodic behaviour illustrates the fact that the local maxima are indicative of true saturation behaviour.

occured and to some extent enhances Landau damping of the first and second coupled modes (and higher order modes).

A second and probably more significant effect not accounted for by the theory is the excitation of the second coupled mode itself. In Fig. 30 we have reproduced the Ψ_0 and $\Psi_{\pm 1}$ growth curves on the offset timescale (offset by 40 $\omega_{p0}t$). One can see that the Ψ_0 mode behaviour departs most severely from the theoretical prediction at exactly the time when the $\Psi_{\pm 2}$ mode has reached its largest amplitude. Because the warm plasma theory of Ch. II does not take the higher order modes into consideration, this behaviour is not unexpected. The $\Psi_{\pm 2}$ mode and higher order modes all act as a sink of beat wave energy and further reduce its amplitude. The warm plasma theory of Ch II does not take the higher order modes into consideration. In their absense, it is not unreasonable to expect that the beat wave and first coupled mode sustain a higher amplitude since no higher order modes are present to absorb energy.

ESTIMATION OF BEAT WAVE SATURATION TIME

A simple law for estimating the beat wave saturation time was emperically derived by determining the beat wave saturation time from the theoretical growth curves as a function of the thermal parameter p and the ripple depth ε. The results of these measurements are shown in Fig. 31. It was found that $\omega_{p0}t_{sat} \cong$

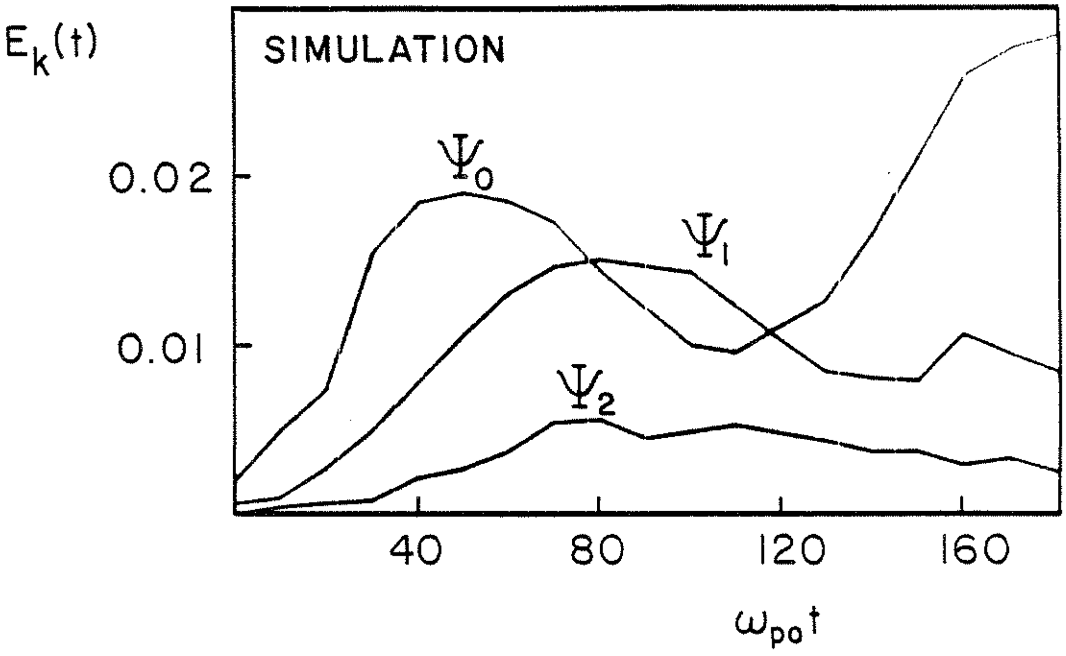

Fig. 30: Growth curves for the Ψ_0, $\Psi_{\pm 1}$, and $\Psi_{\pm 2}$ modes obtained from simulation. These curves show the exchange of energy between the various modes excited. The time scale has been offset to the left by $40\omega_{po}t$ and the fields are normalized to $mc\omega_{po}/e$.

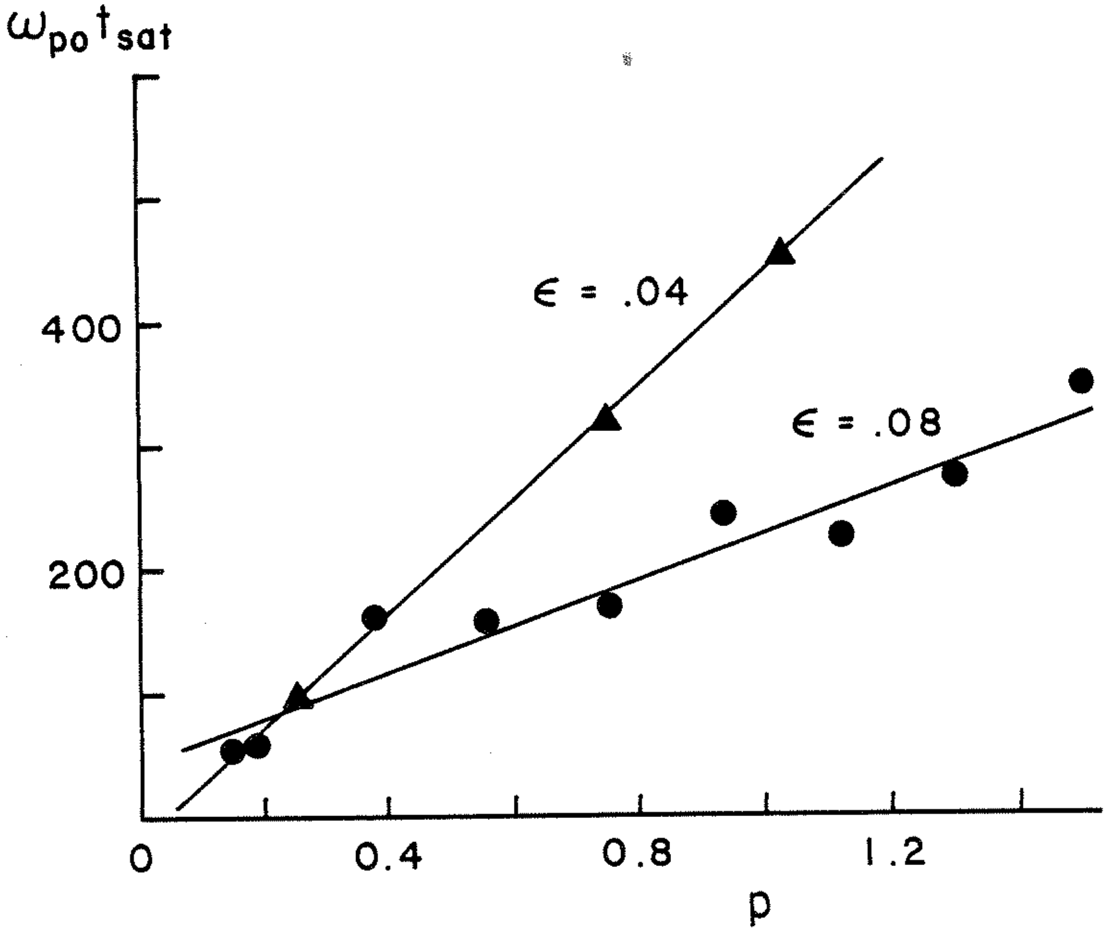

Fig. 31: Plots of $\omega_{po}t_{sat}$(beatwave) versus p for two different ripple depths ε. These results were obtained from the warm plasma mode coupling solutions Eq's. 31,32. For $p \geqslant 0.2$ the emperically derived law, $\omega_{po}t_{sat} \cong 17.5p/\varepsilon$, provides a reasonable estimate of the beat wave saturation time.

17.5 p/ε. This law provides a reasonable estimate of $\omega_{po}t_{sat}$ for $p \geqslant 0.2$ since, for sufficiently hot plasmas, the ambiguities in assigning a saturation time discussed above are not encountered (c.f. Fig. 3). The $\omega_{po}t_{sat}$ given by the law for the parameters of the simulation in Figs. 27,28 is in fair agreement with the results of that cool plasma simulation ($\omega_{po}t_{sat} \cong 100$). A simple check of this scaling law's independence of pump amplitude was made. A simulation with all parameters identical to those used in the simulation presented in Figs. 27,28 was performed with a weaker laser pump ($\alpha = .02$ compared to $\alpha = .05$). The saturation time for the beat wave was found to be about the same as in the strong pump case and, if at all, is only very weakly dependent on the laser pump amplitude.

SATURATION AMPLITUDES

The theoretically predicted beat wave (Ψ_0) and first ($\Psi_{\pm 1}$) coupled mode saturation amplitudes are given by Eq's. 35a,b. For the parameters used in the simulation of Fig. 28 (ε=0.1, p=0.466, $\alpha_1=\alpha_2=.05$, and $k_1=1.2(24)^{1/2}$) the expected saturation amplitude for the Ψ_0 $\Psi_{\pm 1}$ modes are .032 and .025 respectively. Refering to Fig. 28, the Ψ_0 and $\Psi_{\pm 1}$ saturation amplitudes observed in the simulations were .028 and .015 respectively. While the saturation amplitude of the Ψ_0 mode is in excellent agreement with the theory, the saturation amplitude of the $\Psi_{\pm 1}$ mode observed in the simulation is only about 60 % of its predicted value. This is possibly due to the fact that, at the time of saturation of the $\Psi_{\pm1}$ mode (c.f. Fig. 30), the $\Psi_{\pm2}$ mode amplitude is at its maximum and presents the maximum possible energy sink to both the Ψ_0 and $\Psi_{\pm1}$ modes. In addition, the higher order modes (not shown) further act to reduce the amplitude of the Ψ_0 and $\Psi_{\pm1}$ modes in the simulation.

The excitation to finite amplitudes of the higher order modes is an obvious point of departure of the experiment from the idealized theoretical model. Interestingly the experimentally measured amplitudes of the Ψ_0 and $\Psi_{\pm1}$ modes (c.f. Fig. 18) also fall below their theoretically perdicted values. In addition the the Thomson scatter spectra of Ch. III consistently showed that the Ψ_{+n} modes had higher amplitudes than the Ψ_{-n} modes (n>0). In Fig. 32 we have plotted the Ψ_{+1} and Ψ_{-1} growth curves obtained from simulation (the same curves which, when averaged, were presented in Figs. 27, 28, and 30). The growth curves exhibit the opposite behaviour as expected from the experimental measurements. One can imagine in the simulations, because the Ψ_{+1} mode is significantly slower ($\cong$30%) than the smaller-k Ψ_{-1} mode, that Landau damping has a stronger impact on the Ψ_{+1} mode than on the Ψ_{-1} mode and yelds a smaller Ψ_{+1} mode amplitude. By contrast in the experiment, the k's of the Ψ_{+1} and Ψ_{-1} modes are very nearly equal and differential Landau damping could not explain the difference in amplitudes even if the Ψ_{+1} mode had been observed to be smaller (which it was not).

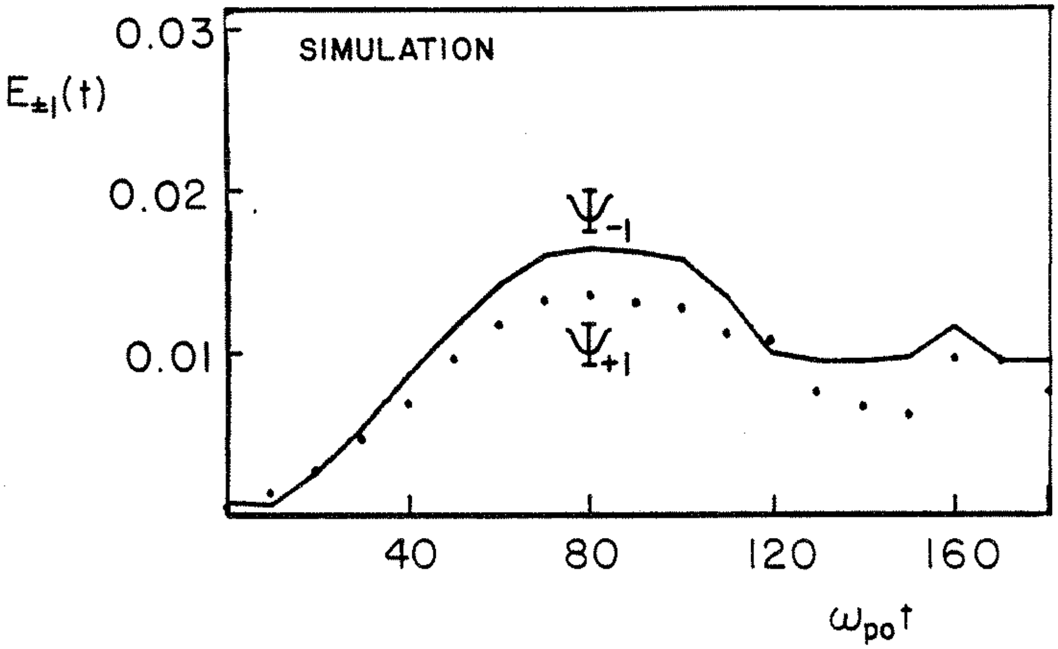

Fig. 32: Growth curves for the Ψ_{+1} and Ψ_{-1} modes obtained from simulation. The higher phase velocity Ψ_{-1} mode maintains a slightly higher amplitude than the slower Ψ_{+1} mode.

It is more likely the experiment that CPOM is a more important consideration in resolving the question of the relative amplitudes of the $\Psi_{=1}$ and Ψ_{-1} coupled modes.

CHAPTER VI: SUMMARY

A simple theoretical model for beat excitation of electron plasma waves in a rippled density plasma has been presented. The model predicts a new beat wave saturation mechanism. In cold plasmas the beat wave saturates because an infinite number of longer-k, secondary electrostatic modes are excited. These modes have frequencies equal to ω_{po} (the background plasma frequency) but their wavenumbers are equal to the beat wave wavenumber, k_p, plus multiples of the ripple wavenumber, k_i. The ripple is commonly encountered in experiments in the form of an ion acoustic wave driven by the stimulated Brillouin instability. These coupled modes divert laser pump energy from the beat wave. When the rate at which pump energy is supplied to the beat wave equals the rate at which energy is deposited in the coupled modes, the beat wave saturates. The saturation amplitude (normalized to the cold plasma wave breaking field $mc\omega_{po}/e$) in cold plasmas is given by $E_{sat}(\mathrm{cold})=\alpha_1\alpha_2/\varepsilon$ where $\alpha_j=eE/m\omega_j c$ parameterizes the laser intensity and ε is a measure of the ripple depth.

In warm plasmas the electrostatic coupled mode spectrum is limited in the number of excited modes because only those modes whose Bohm-Gross frequency shifts do not exceed the variation of $\omega_{po}(x)$ in the density ripple are excited. Because the number of coupled modes is limited, the beat wave saturates at a higher amplitude. In warm plasmas, the saturation amplitude is given by $E_{sat}(\mathrm{warm})=$

$\alpha_1\alpha_2 f(p)/\varepsilon$ where $f(p)=p+(1+p^2)(2+p)^{-1/2}$ is a thermal enhancement factor and p is a thermal parameter defined by $p=3(k_i\lambda_d)^2/\varepsilon$.

The relevance of the mode coupling saturation mechanism can be assessed by comparing the mode coupling beat wave saturation amplitude with that expected for relativistic detuning. One finds that saturation by mode coupling dominates over that due to relativistic detuning whenever $\alpha_1\alpha_2<\left(1.6f(p)/\varepsilon\right)^{-3/2}$. For example in the case of a modest ripple size of $\varepsilon=0.04$ and $\alpha_1=\alpha_2$, saturation by mode coupling dominates unless $\alpha_j>0.04$ or, in the case of a CO_2 laser, unless $I(CO_2)>4\times10^{13}$ W/cm^2. Although this requirment may be altered somewhat when laser rise times are considered, it is apparent that the mode coupling saturation mechanism can be quite important in moderate-intensity or shorter-wavelenght experiments.

The coupled mode spectrum itself is of interest from a basic plasma physics standpoint, irrespective of the beatwave. Experiments which were designed to study and characterize the ω and k spectrum of the coupled modes as well as that of the beat wave were performed. These epxeriments were performed in an 10^{17} cm^{-3} density plasma using the 10.6 and 9.6 μm lines of 2 ns pulsewidth CO_2 laser capable of delivering about 10^{13} W/cm^2 at its focus. Detailed measurements employing ruby laser Thomson scattering were made. The measured electrostatic ω and k spectrum agreed well with the theory. In addition the measured coupled mode amplitudes were consistent with the mode coupling saturation model. Although the coupled modes were conclusively observed, the experimental parameters were such that the actual beat wave saturation amplitude measured was consistent with both the mode coupling and relativistic detuning saturation models.

To further corroborate the theoretical predictions and experimental measurements, particle simulations were performed using the PIC code *WAVE*. Particular attention was directed toward the observation of the beat wave mode coupling saturation mechanism and the theoretically predicted properties of the coupled mode k-spectrum.

Early simulations verified the excitation of the beat wave and coupled modes at precicely the theoretically predicted wavenumbers. In addition by following and recording the temporal development of the beat wave and coupled modes we were able to compare theory and simulation directly for the same parameters. The growth curves for the beat wave and coupled modes are in excellent agreement at early times with regard to saturation times and saturation amplitudes. At later times the deviation in behaviour of the theory and simulation growth curves becomes evident as the contributions of the higher order coupled modes, not included in the warm plasma model, become more and more important.

In cold plasma, long pulse experiments, the mode coupling saturation mechanism can undergo self stabilization if the plasma is heated to the point where the Bohm-Gross frequency shift of the first coupled mode is sufficiently large to detune them from the fixed frequency driver. This self stabilization mechanism was observed in one simulation whose electrons were initialized at t=0 with zero thermal motion. For early times the beat wave grew much as predicted by the cold plasma theory and the k-spectrum clearly indicated the presence of the coupled modes. However at later times we observed abrupt quenching of the coupling concomitant with the onset of particle heating observed in the electron distribution function and in electron phase space.

REFERENCES

(1) T. Tajima and J. M. Dawson, Phys. Rev. Lett <u>43</u>, 267 (1969)

(2) C. Joshi, W. B. Mori, T. Katsouleas, J. M. Dawson, J. M. Kindel, and D. W. Forslund, Nature <u>311</u>, 256 (1984)

(3) Norman M. Kroll, Amiran Ron, and Norman Rostoker, Phys. Rev. Lett. <u>13</u>, 83 (1964)

(4) D. Montgomery, Physica (Utrecht) <u>31</u>, 693 (1965)

(5) R. A. Stern and N. Tzoar, Phys. Rev. Lett <u>16</u>, 785 (1966)

(6) M. N. Rosenbluth and C. S. Liu, Phys. Rev. Lett. 29, 701 (1972)

(7) W. L. Kruer, Phys. Fluids <u>15</u>, 2423 (1972)

(8) P. K. Kaw, A. T. Lin, and J. M. Dawson, Phys. Fluids <u>16</u>, 1967 (1973)

(9) C. M. Tang and P. Sprangle, App. Phys. Lett <u>45</u>, 375 (1984)

(10) John M. Dawson, Phys. Rev. 113, 383 (1959)

(11) Behrouz Amini and Francis F. Chen, Phys. Rev. Lett 53, 1441 (1984)

(12) C. Aldrich, B. Bezzerides, D. F. DuBois, H. Rose, Los Alamos Report No. LA-UR 85-2099 (unpublished)

(13) C. Clayton, C. Joshi, and F. F. Chen, *Laser Interactions and Related Plasma Phenomena*, (Plenum), Vol. 6.

(14) C. J. Walsh, D. M. Villeneuve, and H. A. Baldis, Phys. Rev. Lett. 53, 1445 (1984)

(15) D. M. Villeneuve, C. J. Walsh, and H. A. Baldis, Phys. Rev. Lett. 28, 1591 (1985)

(16) S. J. Kartunnen, Plasma Phys. 22, 251 (1980)

(17) D. E. Evans and J. Katzenstein, Rep. Prog. Phys 32, 207 (1969)

(18) Christopher E. Clayton, Chris Darrow, and Chan Joshi, Appl. Optics 24 2823 (1985)

(19) D. W. Forslund, J. M. Kindel, and E. L. Lindman, Phys. Rev. Lett. 30, 739 (1973)

(20) D. W. Forslund, J. M. Kindel, and E. L. Lindman, Phys. Flu. 18, 1002 (1975

(21) D. W. Forslund, J. M. Kindel, and E. L. Lindman, Phys. Flu. 18, 1017 (1975)

(22) L. D. Landau and E. M. Lifshitz, *Electrodynamics of Continuous Media*, Pergamon Press, New York

(23) R. E. Slusher and C. M. Surko, Phys. Fluids 23, 472 (1980)

(24) F. Martin and T. W. Johnston, Phys. Rev. Lett. 55, 1651 (1985)

(25) C. Clayton, C. Joshi, C. Darrow, and D. Umstadter, Phys. Rev. Lett. 55, 1652 (1985)

(26) R. L. Morse, C. W. Neilson, Phys. Fluids 14, 830 (1971)